

INFORMATION TO USERS

The most advanced technology has been used to photograph and reproduce this manuscript from the microfilm master. UMI films the original text directly from the copy submitted. Thus, some dissertation copies are in typewriter face, while others may be from a computer printer.

In the unlikely event that the author did not send UMI a complete manuscript and there are missing pages, these will be noted. Also, if unauthorized copyrighted material had to be removed, a note will indicate the deletion.

Oversize materials (e.g., maps, drawings, charts) are reproduced by sectioning the original, beginning at the upper left-hand corner and continuing from left to right in equal sections with small overlaps. Each oversize page is available as one exposure on a standard 35 mm slide or as a 17" x 23" black and white photographic print for an additional charge.

Photographs included in the original manuscript have been reproduced xerographically in this copy. 35 mm slides or 6" x 9" black and white photographic prints are available for any photographs or illustrations appearing in this copy for an additional charge. Contact UMI directly to order.



300 North Zeeb Road, Ann Arbor, MI 48106-1346 USA

Order Number 8622120

**The measurement of strong-interaction effects in high-Z sigma
hyponic atoms**

Phillips, William Clarke, Ph.D.

The College of William and Mary, 1988

Copyright ©1980 by Phillips, William Clarke. All rights reserved.

U·M·I

300 N. Zeeb Rd.
Ann Arbor, MI 48106

PLEASE NOTE:

In all cases this material has been filmed in the best possible way from the available copy. Problems encountered with this document have been identified here with a check mark .

1. Glossy photographs or pages _____
2. Colored illustrations, paper or print _____
3. Photographs with dark background _____
4. Illustrations are poor copy _____
5. Pages with black marks, not original copy _____
6. Print shows through as there is text on both sides of page _____
7. Indistinct, broken or small print on several pages
8. Print exceeds margin requirements _____
9. Tightly bound copy with print lost in spine _____
10. Computer printout pages with indistinct print _____
11. Page(s) _____ lacking when material received, and not available from school or author.
12. Page(s) _____ seem to be missing in numbering only as text follows.
13. Two pages numbered _____. Text follows.
14. Curling and wrinkled pages _____
15. Dissertation contains pages with print at a slant, filmed as received
16. Other _____

U·M·I

THE MEASUREMENT OF STRONG-INTERACTION EFFECTS
IN HIGH-Z SIGMA HYPERONIC ATOMS

A Dissertation

Presented to

The Faculty of the Department of Physics
The College of William and Mary in Virginia

In Partial Fulfillment

Of the Requirements for the Degree of
Doctor of Philosophy

by

William Clarke Phillips

1988

APPROVAL SHEET

This dissertation is submitted in partial fulfillment of
the requirements for the degree of

Doctor of Philosophy

William Clarke Phillips

William Clarke Phillips

Approved, May 1988

Morton Eckhaus

Morton Eckhaus

Carl E. Carlson

Carl E. Carlson

John R. Kane

John R. Kane

Robert E. Welsh

Robert E. Welsh

Rolf G. Winter

Rolf G. Winter

Richard L. Kiefer

Richard L. Kiefer
Department of Chemistry

©1989

WILLIAM CLARKE PHILLIPS

All Rights Reserved

DEDICATION

To my parents Robert E. and Edna C. Phillips
for stability, courage, and persistence

AND

To my wife Shelly Wolfe Phillips
for helping to maintain my essential insanity
through it all

TABLE OF CONTENTS

	Page
ACKNOWLEDGMENTS.....	vi
LIST OF TABLES.....	x
FIGURE CAPTIONS.....	xii
ABSTRACT	xv
INTRODUCTION	2
CHAPTER I. THEORY	6
Energy Levels of Hadronic Atoms	8
Governing Equations and Method of Solution..	8
Klein-Gordon Equation.....	9
Dirac Equation.....	12
Corrections to the Energy Levels	17
Electron Screening.....	17
Quantum Electrodynamic Corrections.....	18
Nuclear Recoil.....	21
Static Polarizability.....	23
Intrinsic Nuclear Multipole Moments.....	26
Transition Rates	29
Radiative Transition Rates.....	29
Auger Transition Rates.....	36
Initial Distribution	38
Strong Interactions	42
CHAPTER II. EXPERIMENTAL METHOD	47
Beam Line	49
Target, Counters and Geometry	53
Laminar Target	54
K-STOP Identification	56
Pion Spectrometers	61
X-Ray Spectroscopy System	64
Solid-State Detector Crystals	66
Signal Processing	73
Interconnections and Operation	82
Data Acquisition	84

CHAPTER III. DATA ANALYSIS.....	95
Data Sets.....	95
Playback.....	97
Fitting Algorithm.....	101
Data Fits.....	101
Parameter Fits.....	104
Non-Gaussian Detector Response Functions.....	106
Charge Production and Collection.....	109
Small-Angle Compton Scattering.....	112
Pulse Pileup.....	114
Amplifier and ADC Noise.....	116
Functional Form.....	117
Parameterization of the Detector Response.....	119
Compton-Shelf Parameter.....	120
Pulse Pileup Parameters.....	122
Charge Trapping Parameter.....	125
Gaussian Width Parameter.....	127
Energy Calibration.....	129
Determination of Detector Relative Efficiency.....	131
Determination of Target Transmission.....	133
Measurement of Target Transmission.....	133
Calculation of Target Transmission.....	135
Energy Calculations.....	140
Calculation of Potentials.....	140
Integration of the Wave Equation.....	144
Determination of Eigenvalues.....	145
Grid Selection.....	146
Corrections.....	147
Sequence of Calculations.....	149
Cascade Simulations.....	151
Initial Approximations.....	151
Optimization of Computational Technique.....	153
Determination of Initiation Parameters.....	154
CHAPTER IV. RESULTS AND CONCLUSIONS.....	165
Widths and Shifts.....	165
Yield Reductions.....	168
Scattering Lengths.....	169
Discussion and Theoretical Implications.....	173
APPENDIX A Calculation of Higher-Order Vacuum Polarization Potentials.....	175
BIBLIOGRAPHY.....	179
FIGURES.....	184

ACKNOWLEDGMENTS

I would like to thank the many dedicated individuals whose countless hours of labor have made this experiment possible. I would especially like to thank:

Dr. Morton Eckhause, my advisor, for his boundless energy and meticulous attention to details throughout all phases of this work. It would not have been possible without Morty.

Dr. John Kane, for his contributions to the design and construction of the laminar target and the pion spectrometer arrays, and for his calm in the face of the storm.

Dr. Robert Welsh, for his many contributions to the design and operation of the experimental apparatus, and for his many creative ideas and continued enthusiasm in the face of adversity.

Dr. Rolf Winter, for continually demonstrating the usefulness of the backs of envelopes, thereby reminding me of the essential aspects of the experiment.

Dr. Dave Hertzog, for his extraordinary contributions in bringing the many facets of this experiment together for the first time, and for his pioneering efforts at analyzing and understanding the results.

Mr. Bill Vulcan, for his magic touch (generously applied) at keeping the electronics happy and healthy in a hostile environment, and for taking the extra effort to teach me to learn electronics, rather than simply trying to teach me electronics.

Dr. Rob Whyley, for his many hours of very helpful assistance on the experimental runs, and for keeping the computer system running smoothly during the course of my analysis.

Drs. Lee Roberts and Jim Miller for their assistance with the experimental runs, and for useful contributions to the experimental design.

Dr. Fran O'Brien, for his many hours of dedicated work in all aspects of the execution of this experiment.

Dr. Roger Sutton, for his Monte-Carlo simulations which guided the experimental design, and for his assistance with the experimental runs.

Dr. Ray Kunselman, for his help during the experimental runs, his work on the cascade program, and his cheery disposition.

Dr. Paul Guss, for help with the experimental runs, and for special assistance with the X-ray detectors.

Fellow graduate students Michael Chapman, John Ginkel, Chris Kenney, Jim Kraiman and Eric Austin, for their help on the experimental runs.

Drs. Nick Colella, George Dodson, Don Joyce, Dick Powers, and Mr. Dan Tieger for their various contributions to the design, construction, and operation of the experimental apparatus.

Drs. Marvin Blecher, Edith Borie, and Mel Leon, for providing copies of their energy-calculation and cascade-simulation programs.

Dr. Phil Pyle, for his remarkable and gracious assistance in tuning the C4 beam line.

the entire staff of the Brookhaven AGS, for their continuing dedication to the smooth operation of the accelerator, and in particular, the Hydrogen Target Group for the construction and maintenance of the laminar targets, and the Electronics Group for their exceptional assistance with the assembly and maintenance of the electronics (Thanks Russ!).

Ms. Sylvia Stout, for always knowing where it is, who they are, where I need to go, and what I need to be doing.

Mr. Richard Pehl, Mr. Fred Goulding, Mr. Donald Landis, and Mr. Norm Madden of Lawrence Berkeley Laboratory, and Mr. Rex Trammell of EG&G Ortec, for designing and constructing an exceptional X-ray detector array, and for their unparalleled response to our pleas for emergency repairs.

Dr. John Bensei, Mr. Melvin Woods, and Mr. Norm Rainville of the William and Mary physics machine shop, for production of the pion spectrometer scintillation counters.

Mrs. Molly Wolfe, for providing an excellent living and working environment during the crucial, final six-month period of my analysis.
Thanks, Kig!

and finally, I would like to thank the inventors of white-out and duct tape, without which this experiment would not have been practical.

This work was supported in part by the National Science Foundation.

LIST OF TABLES

<u>Table</u>	<u>Page</u>
I	C4 Beam Line Elements and Settings for 680 MeV/c K^- 52
II	Beam-Defining Telescope Counters 60
III	Pion Spectrometer Elements 61
IV	Left Pion Spectrometer Logic Signals 62
V	X-ray Detector Crystal Specifications 72
VI	CAMAC Crate Configuration 85
VII	Calibration γ -ray Energies 87
VIII	Software Event Types 91
IX	Event Information 92
X	Data Collection Periods 96
XI	Summed Data Files 100
XII	Compton-Shelf Parameterization 122
XIII	Pulse Pileup Amplitude Parameterization 123
XIV	Pulse Pileup Length Parameterization 124
XV	Charge Trapping Parameterization 126
XVI	Gaussian Width Parameterization 128
XVII	Energy Parameterization 130
XVIII	Detector Relative Efficiency Parameterization 132
XIX	Potentials Calculated for Each Hadron-Nucleus System 141
XX	Weighted Means of Nuclear Parameters 142
XXI	Optimization Parameters for the Cascade Simulation 154
XXII	Beam Steering and Hadron Initial Distribution Parameters 160
XXIII	Measured and Calculated Kaonic Atom X-ray Relative Yields 161

<u>Table</u>	<u>Page</u>
XXIV Measured and Calculated Σ^- Atom X-ray Relative Yields . .	162
XXV Calculated Yields of Σ^- -W X-ray Components	163
XXVI Calculated Yields of Σ^- -Pb X-ray Components	164
XXVII Strong Interaction Effects Measured in Σ^- -W and Σ^- -Pb .	171
XXVIII Strong Interaction Effects Calculated for Σ^- -W and Σ^- -Pb	172

FIGURE CAPTIONS

1. Vacuum polarization potentials of order $\propto (Z\alpha)^{3,5,7}$ for $Z=82$, as calculated by Reference [8] (point nucleus) and Reference [9] (finite nucleus)
2. Selected transitions between atomic energy states labeled by the principal and orbital quantum numbers. Fine-structure splittings and $\Delta l = +1$ transitions omitted for clarity.
3. Distributions in angular momentum of hadrons immediately after atomic capture, as calculated by Reference [60]. E_F is the Fermi energy parameter.
4. Layout of AGS C4 beam line. A series of magnetic lenses is used to transport particles of a desired momentum.
5. Experimental apparatus, including beam-defining plastic scintillators, π^+ spectrometers, and X-ray detectors (A, B, C) located below target (T).
6. Sketch showing laminar target foil array and surrounding cryogenic housing (a) — side view, (b) — front view
7. Pulse height in counter S5 gated by S1-S2-C-S3-S4-S5. A 300 mV threshold was placed on S5 in the data runs to select stopping kaons by dE/dX
8. Beam telescope logic block diagram. Units contained within dashed box were located just outside the experimental area; others were located in a nearby counting trailer.
9. Logic diagram for left-arm π^+ spectrometer. Right side is identical.
10. Delayed e^+ events recorded in right π^+ spectrometer and fitted to $A \exp[-t/\tau] + B$, with the result for the μ^+ lifetime $\tau = 2.26 \pm 0.1 \mu\text{sec}$.
11. X-ray detector array showing top and side view of detector housing and relative positions of crystals.
12. Block diagram of detector preamplifier system, including detector crystal, charge-sensitive amplifier, reset control logic, and reset transistor (T).

13. Logic diagram showing those X-ray spectroscopy system units which were housed in thermally controlled environment near the experimental area.
14. Histogram of time relationship between KS signals and detector A events.
15. Logic diagram showing X-ray spectroscopy system gating event-type identification circuitry.
16. Logic diagram showing CAMAC gating and CAMAC modules. MBD was interrupted by LAM from trigger module.
17. Untagged Pb X-ray summed (A+B+C) histogram with transitions as indicated.
Horizontal scale: $E(\text{keV}) = 0.090 X (\text{Channel}-851.5)$
18. Tagged Pb X-ray summed (A+B+C) histogram with transitions as indicated.
Horizontal scale: $E(\text{keV}) = 0.090 X (\text{Channel}-851.5)$
19. Untagged W X-ray summed (A+B+C) histogram with transitions as indicated.
Horizontal scale: $E(\text{keV}) = 0.090 X (\text{Channel}-851.5)$
20. Tagged W X-ray summed (A+B+C) histogram with transitions as indicated.
Horizontal scale: $E(\text{keV}) = 0.090 X (\text{Channel}-851.5)$
21. A portion of the energy spectrum from summed tagged(a) and untagged(b) histograms showing the dramatic effect of tagging on Σ^- X-ray signal-to-noise ratio.
22. Gaussian function fitted to a high-statistics diagnostic dataset (semi-logarithmic scale). Note the low-energy tail structure of the dataset.
23. Representative probability functions from the detector response model of Section III.4.
 - a) Charge production and collection effects.
 - b) Effects of small-angle Compton scattering (exaggerated for clarity).
 - c) Pulse-Pileup effects (exaggerated for clarity).
24. Detector B relative-efficiency dataset and its parameterization, with error bars.
25. Σ^- -W and Σ^- -Pb target transmission curves with statistical error bars (Monte-Carlo calculation). Normalization is arbitrary.

26. Ratios of measured to calculated yield in K^- -Pb, showing the effect of the beam steering parameter z_s .

ABSTRACT

Strong-interaction effects have been observed in the X-ray spectra of atoms formed with Σ^- in lead and tungsten.

In the experiment, performed at the Alternating Gradient Synchrotron of Brookhaven National Laboratory, negative kaons were brought to rest in a novel laminar target consisting of thin sheets of high-Z material in a liquid hydrogen bath. The geometry of the target was designed to optimize the production of high-Z Σ^- atoms and the detection of their subsequent de-excitation X rays. A method of identifying the energetic π^+ from the production reaction $K^- + p \rightarrow \Sigma^- + \pi^+$ resulted in a factor of 15 improvement in the signal-to-noise ratio of the Σ^- atom X rays over that of previous experiments. The X-ray spectra were recorded by three high-resolution intrinsic Ge detectors and analyzed for shifts, broadenings, and yield reductions of the final X-ray transitions before absorption of the Σ^- into the nucleus. A lineshape function which reflected the non-Gaussian response of the X-ray spectroscopy system was developed for this analysis. The results are

$$\Sigma^- - W (10 \rightarrow 9) : E = 650 \pm 30 \text{ eV}, \quad \Gamma = 380 \pm 70 \text{ eV}, \quad \%Y = .98 \pm .04$$

$$\Sigma^- - Pb (10 \rightarrow 9) : E = 510 \pm 50 \text{ eV}, \quad \Gamma = 290 \pm 140 \text{ eV}, \quad \%Y = .53 \pm .04$$

where $E = E_{\text{meas}} - E_{\text{calc}}$, Γ is the Lorentzian FWHM, and $\%Y$ is the ratio (measured yield)/(yield calculated with no strong interaction).

Optical model calculations with $\bar{a} = (0.928 + i0.022)$ fm are able to reproduce all observed effects in the $\Sigma^- - W$ spectra. Such calculations with $\bar{a} = (0.247 + i0.039)$ fm reproduce the observed shift and width of the $(10 \rightarrow 9)$ transition in $\Sigma^- - Pb$, but fail to reproduce the observed yield reduction. It is doubtful if the current status of the theory of $\Sigma^- - N$ interactions can explain this discrepancy.

**THE MEASUREMENT OF STRONG INTERACTION EFFECTS
IN HIGH-Z SIGMA HYPERONIC ATOMS**

INTRODUCTION

An exotic atom is formed when a negative particle other than an electron is captured into an atomic orbit around a nucleus. Since electrons are the least massive of the known negatively charged particles, the resulting exotic atomic states have smaller radii and larger binding energies than do the usual (electronic) atomic states of the same quantum numbers. The heavy particle may be a lepton, a meson or a baryon. For this work we are interested in atoms formed with kaons (K^-) and sigma hyperons (Σ^-). In the discussion that follows it is assumed that the heavy particle is either a meson (integral spin hadron) or a baryon (fractional spin hadron), although much of the theory (excluding that part which deals with strong interaction effects) was developed for and is also applicable to muonic atoms.

A hadronic atom goes through several distinct phases in the course of its lifetime. Formation of a hadronic atom occurs after a negatively charged hadron is brought to rest in material composed of target atoms. Initially the hadron has excess kinetic energy, and it passes through and interacts with the electron clouds of the target atoms without being captured. Energy is lost in these interactions until the speed of the hadron becomes comparable to the speeds of the atomic electrons. At this point, transitions to bound states become

probable, and atomic capture occurs.

Once captured, the hadron may de-excite to a more tightly bound state either by emitting an X ray or by transferring the energy difference to an electron via an Auger transition. As the hadron de-excites through the electron cloud, there is a large overlap between the hadronic and electronic wave functions and Auger transitions dominate the energy loss. The energy transferred to the electron in this case is usually enough to eject it from the electron cloud, ionizing the target atom. If the target material is a metal, replenishment of these vacated electronic states is usually so much more rapid than the ionization processes that all of the electron shells are effectively full all of the time [1].

When the orbital radius of the hadron becomes less than that of the innermost orbital electron the overlap needed for Auger transitions declines and X-ray (or radiative) transitions dominate the energy loss. The atomic electrons have very little effect during this radiative phase because most of their charge lies well outside of the hadronic orbits. The overlap between the hadron and the nucleus is usually negligible at this point so that the only appreciable forces acting are electromagnetic in nature. The nuclear charge distributions are known well enough [2] that accurate calculations should be possible, although higher-order quantum electrodynamic effects must be taken into account for moderate- to high-Z target nuclei [3,4]. This phase of the life of a hadronic atom thus serves as a testing ground for several important QED calculations.

Experiments designed specifically to test vacuum polarization [5] and Lamb shift [6,7] effects have stimulated many different approaches to the calculation of these effects [8-11].

If QED effects are understood well enough, study of the radiative phase of exotic atoms can also yield information about the orbiting particle. The X-ray transition energies are sensitive to the mass of the particle [12-14]. If the particle has a magnetic moment the X rays exhibit fine-structure splitting characteristic of that moment [14-16].

The hadronic atom continues to de-excite by way of radiative transitions until a state is reached which has an appreciable overlap with the nuclear matter distribution. Here the strong interactions which characterize this final absorptive phase can alter the X-ray transitions in three ways [17,18]. As soon as the hadron reaches a state which has any overlap with the nucleus, absorption by the strong interaction competes with the radiative and Auger transitions for the state's depletion. The intensities of any X-ray transitions which originate in this state or one of its successors are thus reduced. If the hadron survives to reach a state with more overlap the strong interaction may actually shift the energy level by an observable amount. Also, the rapid strong absorption resulting from the increased overlap reduces the mean life of the state to a value such that a broadening of the energy level due to the uncertainty principle may be observable.

Because of the strength of the strong interaction, the effects on atomic states increase very rapidly as a function of the orbital-nucleus overlap integral. This provides a convenient separation of the strong interaction effects on a given state from the effects on its predecessor states. For any observable X-ray transition, strong interaction effects on the final state are typically several orders of magnitude larger than those on the initial state. The shifts and broadenings of the X-ray transition energies are thus dominated by the shifts and broadenings of the energies of the final states. Similarly, any strong interaction effects on the initial states' predecessors are typically several orders of magnitude smaller than those on the initial states. The reduction in intensity of a particular X-ray transition is thus dominated by strong absorption out of the initial state itself rather than out of any of the initial state's predecessors.

Chapter I

THEORY

Extraction of strong interaction effects from X-ray transitions in hadronic atoms requires a calculation of the energies and intensities of these transitions in the absence of any strong interaction. The physical system involved is quite complex. The unperturbed nuclear charge distribution is not necessarily spherically symmetric and may possess intrinsic electric and/or magnetic multipole moments. The quantum electrodynamic interaction between the nucleus and the orbiting hadron must be calculated to a sufficiently high order to include all significant effects. Possible spin and anomalous magnetic moment structures of the orbiting hadron must be taken into account, as well as any residual effects of the electron cloud which surrounds the hadron-nucleus system. The extremely strong electric fields experienced by both the nucleus and the hadron result in physical deformations of both systems. If a resonance condition occurs, this can cause transitions of the nucleus to excited states [19]. All of these effects can alter the energy levels of the hadronic bound states.

Predictions of X-ray intensities require not only an understanding of the radiative transition process but also knowledge of the initial state populations. Unfortunately, this population

distribution is not independent of the strong interaction. Strong absorption effects on states having large principal quantum number n but small values of angular momentum may be described sufficiently well by an optical potential, but the details of how such absorption effects the population distribution is not easily derived by analytical means. A computer model of the hadronic cascade is usually used to predict the initial state populations in the presence of the (simplified optical model) strong interaction so that intensity reductions in an X-ray transition may be associated with strong absorption out of the initial state rather than with any strong interaction induced variations in the initial state population. Such a computer model requires some ansatz concerning the distribution in angular momentum of the orbiting hadrons immediately after atomic capture. Auger transitions must be included if the model is to be considered a realistic representation of the cascade process.

Finally, deviations of measured intensities from predictions cannot be firmly linked to a strong-interaction absorption rate without first accounting for all other processes which may contribute to depopulation of the initial states. Such processes include Auger transitions and decay of the orbiting hadron. An exposition of the theories needed to make the energy and intensity predictions pertinent to this analysis follows.

I.1 Energy Levels of Hadronic Atoms

I.1.1 Governing Equations and Method of Solution

The dynamics of high-Z exotic atoms formed with particles having spins of zero or one half are governed by the Klein-Gordon or Dirac equations [20]. The large ratio of nuclear to hadronic masses insures that most of the relativistic effects are associated with the hadron. This means that the classical reduced mass approximation will account adequately for most of the nuclear recoil. For the Ξ^- -Pb and Ξ^- -W systems the residual relativistic corrections to the nuclear recoil are less than 20 eV in magnitude.

The method of solution is similar for both equations. The equation is solved for bound energy eigenstates, usually in a potential generated by a static, spherically symmetric nuclear charge distribution of realistic finite extent. In this case the equations are separable into radial and angular parts. Solutions take the form of radial functions multiplying angular functions which are eigenstates of the total angular momentum operator. All dynamical effects are contained in the radial equations, which may be solved numerically for most physically realistic charge distributions. In practice, many of the nuclei for which one might wish to solve these equations are indeed spherically symmetric (even-even). If not, any effects due to nuclear asymmetry are usually small and may be treated

as a first-order perturbation to the spherically symmetric solution.

It is useful to have available analytical solutions for two special cases. The energy eigenvalues for a point charge distribution are frequently good starting points for eigenvalue searches involving more realistic finite charge distributions. A first-order perturbation calculation using the basis states of a point charge solution can improve such an initial guess dramatically, and is not very costly in computation time.

The radial eigenfunctions for a spherical square-well potential may be used to initialize numerical integration algorithms at any radius where the actual potential is a sufficiently slowly varying function of radius. This condition is met at very large and very small radii by potentials generated by physically realistic charge distributions.

I.1.2 Klein-Gordon Equation

The Klein-Gordon equation for a free particle of mass m is [21]

$$I.1-1) \quad [\pi^\mu \pi_\mu - (mc)^2] \Psi = 0$$

where $\pi^\mu = i\hbar(\partial/\partial x_\mu)$ is the four-momentum operator corresponding to space-time coordinates $x^\mu = (ct, \vec{x})$. Note that

$$\pi^\mu \pi_\mu = -\hbar^2 \left(\frac{\partial}{\partial x_\mu} \right) \left(\frac{\partial}{\partial x^\mu} \right) = -(\hbar/c)^2 \frac{\partial^2}{\partial t^2} + \hbar^2 \nabla^2 = (E/c)^2 - |\vec{p}|^2$$

Coupling to an external electromagnetic field is effected by the substitution

$$I.1-2) \quad \pi^{\mu} \longrightarrow \pi^{\mu} - (e/c)A^{\mu}$$

where $A^{\mu} = (\phi, \vec{A})$

In the case of a static Coulomb potential $A^{\mu} = (\phi(\vec{x}), \vec{0})$, equation (I.1-1) becomes, in the more usual non-covariant notation

$$I.1-3) \quad \left[\left(\frac{1}{c} \frac{\partial}{\partial t} + \frac{ie\phi(\vec{x})}{\hbar c} \right)^2 - \nabla^2 + \left(\frac{mc}{\hbar} \right)^2 \right] \Psi = 0$$

Any stable bound state which is a solution to equation (I.1-3) will be an eigenstate of the Hamiltonian H:

$$I.1-4) \quad H\Psi = i\hbar \frac{\partial \Psi}{\partial t} = E\Psi$$

Solutions of the form $\Psi(\vec{x}, t) = \psi(\vec{x}) e^{-iEt/\hbar}$ satisfy this condition, and equation (I.1-3) becomes

$$I.1-5) \quad \left[\nabla^2 + \frac{(E - e\phi(\vec{x}))^2 - (mc^2)^2}{(\hbar c)^2} \right] \psi(\vec{x}) = 0$$

For a spherically symmetric potential $\phi(\vec{x}) = \phi(r)$, equation (I.1-5) is separable into radial and angular equations [22]. The angular equation is solved by the usual spherical harmonics $Y_{\ell}^m(\theta, \phi)$ and has a separation constant equal to $\ell(\ell+1)$. The resulting equation for the radial function $R(r)$

$$I.1-6) \quad \frac{d^2 (rR(r))}{dr^2} + \left[\frac{[(E - e\phi(r))^2 - (mc^2)^2]}{(\hbar c)^2} - \frac{\ell(\ell+1)}{r^2} \right] (rR(r)) = 0$$

may be solved numerically for most non-pathological potentials $\phi(r)$.

Power series techniques may be used to solve this equation in the case of a Coulomb potential generated by a (static) point charge distribution with the result [23]

$$I.1-7) \quad E(n, \ell) = mc^2 \left[1 + \left(\frac{Z\alpha}{n - (\ell + 1/2) \pm \sqrt{(\ell + 1/2)^2 - (Z\alpha)^2}} \right)^2 \right]^{-\frac{1}{2}}$$

In regions of constant potential the term $-e\phi(r)$ may be combined with the energy to give an effective energy $E' = E - e\phi$. Solutions for energy E in these regions of constant potential ϕ may be expressed as linear combinations of the free-particle (i.e., $\phi=0$) solutions for energy E' . The substitutions

$$I.1-8) \quad z = \frac{\sqrt{(E - e\phi)^2 - (mc^2)^2}}{\hbar c} r$$

and $w(z) = r(z)R(r(z))$

result in a slightly different form of equation (I.1-6) for regions of constant potential:

$$I.1-9) \quad z^2 w'' + [z^2 - \ell(\ell+1)]w = 0 .$$

This is recognized as the equation for the Ricatti-Bessel functions [24]. Linearly independent solution pairs are based on the spherical

Bessel functions of the first and second kinds

$$\begin{aligned} \text{I.1-10) } \quad x j_{\ell}(z) &= \sqrt{\pi z/2} J_{(\ell+\frac{1}{2})}(z) \\ x y_{\ell}(z) &= \sqrt{\pi z/2} Y_{(\ell+\frac{1}{2})}(z) \end{aligned}$$

and of the third kind

$$\begin{aligned} \text{I.1-11) } \quad x h_{\ell}^{(1)}(z) &= \sqrt{\pi z/2} H_{(\ell+\frac{1}{2})}^{(1)}(z) \\ x h_{\ell}^{(2)}(z) &= \sqrt{\pi z/2} H_{(\ell+\frac{1}{2})}^{(2)}(z) \end{aligned}$$

Here $j_{\ell}(z)$, $y_{\ell}(z)$, $h_{\ell}^{(1)}(z)$ and $h_{\ell}^{(2)}(z)$ are spherical Bessel functions, $J_{\ell}(z)$ and $Y_{\ell}(z)$ are the usual Bessel functions of the first and second kinds and $H_{\ell}^{(1)}(z)$ and $H_{\ell}^{(2)}(z)$ are the Hankel functions. These solutions are of particular interest for $E' > mc^2$ at $r=0$, where convergence of the normalization integral limits the solution to $x j_{\ell}(z)$ and for $E' < mc^2$ as $r \rightarrow \infty$, where $x h_{\ell}^{(1)}(z)$ is the only solution which goes to zero as required for a bound state.

I.1.3 Dirac Equation

The Dirac equation for a free particle of mass m is [21]

$$\text{I.1-12) } \quad [\gamma_{\mu} \partial^{\mu} - mc] \psi = 0$$

where the γ^{μ} are Dirac matrices. For space-time coordinates $x^{\mu} = (ct, \vec{x})$ these take the form [23]

$$\begin{aligned}
 \text{I.1-13)} \quad \gamma^0 &= \begin{vmatrix} \langle 1 \rangle & \langle 0 \rangle \\ \langle 0 \rangle & -\langle 1 \rangle \end{vmatrix} & \gamma^i = \vec{\alpha} = \begin{vmatrix} \langle 0 \rangle & \sigma^i \\ \sigma^i & \langle 0 \rangle \end{vmatrix} \\
 \text{where } \langle 1 \rangle &= \begin{vmatrix} 1 & 0 \\ 0 & 1 \end{vmatrix} & \text{and } \langle 0 \rangle = \begin{vmatrix} 0 & 0 \\ 0 & 0 \end{vmatrix}
 \end{aligned}$$

are the 2X2 identity and zero matrices and the σ^i are the usual 2X2 Pauli matrices.

Coupling to an external electromagnetic field is again made by the minimal substitution (I.1-2). Inclusion of an anomalous magnetic moment adds a magnetic dipole term [21]

$$\text{I.1-14)} \quad \left[\frac{\hbar e}{4\pi c^2} \gamma_\mu \gamma_\nu F^{\mu\nu} \right] u$$

to the right side of equation (I.1-12), where

$$\text{I.1-15)} \quad F^{\mu\nu} = \frac{\partial A^\nu}{\partial x_\mu} - \frac{\partial A^\mu}{\partial x_\nu}$$

is Maxwell's field-strength tensor.

Energy eigenstate solutions to the Dirac equation may be separated into spatial and temporal parts of the form $u(\vec{x}, t) = u(\vec{x}) \exp(-iEt/\hbar)$. If solutions are to be limited to energy eigenstates the operator $(\partial/\partial(ct))$ which appears in the Dirac equation may be replaced with its eigenvalue equivalent $(\partial/\partial(ct)) = -iE/\hbar c$ resulting in a simplification of equation (I.1-12). In the case of a spherically symmetric potential the Dirac equation may be separated

into angular and radial parts. The bound state solutions take the form [25]

$$I.1-16) \quad u(x) = \left\{ \begin{array}{l} \frac{G_{\ell,k}(r)}{r} |k, m\rangle \\ \frac{iF_{\ell,k}(r)}{r} |-k, m\rangle \end{array} \right\} \quad \begin{array}{ll} k=\ell & \text{for } j=\ell-1/2 \\ k=(\ell+1) & \text{for } j=\ell+1/2 \end{array}$$

where

$$I.1-17) \quad |k, m\rangle = \left\langle \begin{array}{l} C(\ell, s, (m-\frac{1}{2}), (+\frac{1}{2}) | \ell, s, (|k|-\frac{1}{2}), m) Y_{\ell}^{(m-\frac{1}{2})} \\ C(\ell, s, (m+\frac{1}{2}), (-\frac{1}{2}) | \ell, s, (|k|-\frac{1}{2}), m) Y_{\ell}^{(m+\frac{1}{2})} \end{array} \right\rangle$$

The $C(\ell, s, m_{\ell}, m_s | \ell, s, j, m)$ are vector addition, or Clebsch-Gordan, coefficients.

The resulting radial equations are now [20]

$$I.1-18) \quad \begin{aligned} \frac{dF(r)}{dr} &= \left[\frac{k}{r} + \tilde{K} \frac{d\phi(r)}{dr} \right] F(r) - \frac{[E+e\phi(r)-mc^2]}{hc} G(r) \\ \frac{dG(r)}{dr} &= - \left[\frac{k}{r} + \tilde{K} \frac{d\phi(r)}{dr} \right] G(r) + \frac{[E+e\phi(r)+mc^2]}{hc} F(r) \end{aligned}$$

where $\tilde{K} = g_1 e/2mc^2$ is the anomalous moment term.

This set of equations is amenable to numerical solution.

Bound state energy eigenvalues of the Dirac equation for a static point charge distribution and no anomalous moment may be found by expanding the solutions to the radial equations (I.1-18) in a power series [23]. The discrete energies which result in proper truncation of the series are found to be

$$I.1-19) \quad E(n, j) = mc^2 \left[1 + \left(\frac{2\alpha}{n - (j+1/2) + \sqrt{(j+1/2)^2 - (2\alpha)^2}} \right)^2 \right]^{-1/2}$$

In regions of constant potential the two first-order equations (I.1-18) may be combined to give a single second-order equation for the radial function $G(r)$

$$I.1-20) \quad z^2 w''(z) + [z^2 - k(k+1)]w(z) = 0$$

where once again the substitutions (I.1-8) have been made. This is recognized again as the equation for the Riccati-Bessel functions [24] which has linearly independent solution pairs

$$I.1-21) \quad \text{and} \quad \begin{aligned} & [z j_k(z) , z y_k(z)] \\ & [z h_k^{(1)}(z) , z h_k^{(2)}(z)] \end{aligned}$$

(See eqs. (I.1-10) and (I.1-11))

For $E' > mc^2$, integrability requirements at the origin exclude the $z y_k(z)$ solution for $k > 0$ and the $z j_k(z)$ solution for $k < 0$. For $E' < mc^2$ the solution must vanish at large radius, which excludes the $z h_k^{(2)}(z)$ solution.

Equation (I.1-18) may be manipulated to give

$$I.1-22) \quad F(r) = \frac{\hbar c}{(E - e\phi(r) + mc^2)} \left[\frac{dG(r)}{dr} + \frac{k}{r} G(r) \right]$$

At large and small radii where $G(r)$ is limited to the form of a single Bessel function, the term $dG(r)/dr$ may be evaluated with the help of recursion relations between the Bessel functions [22]. This

results in the solution pair for a constant potential ϕ :

$$G_{n,k}(r) = r f_n(Dr)$$

I.1-23)

$$F_{n,k}(r) = \begin{cases} \sqrt{E - e\phi - mc^2} \\ \sqrt{E - e\phi + mc^2} \end{cases} r f_{(k-)}(Dr)$$

$$\text{where } D = \frac{\sqrt{(E - e\phi)^2 - (mc^2)^2}}{\hbar c}$$

$$\text{and } \begin{cases} r \rightarrow 0 \text{ and } E - e\phi > mc^2 & \begin{cases} k > 0 \rightarrow f_k(z) = j_k(z) \\ k < 0 \rightarrow f_k(z) = y_k(z) \end{cases} \\ r \rightarrow \infty \text{ and } E - e\phi < mc^2 & \rightarrow f_k(z) = h_k^{(0)}(z) \end{cases}$$

Thus the ratio F/G may be calculated at large and small radii whether or not the overall normalization is known. This is sufficient to initialize a numerical integration procedure.

I.2 Corrections to the Energy Levels

I.2.1 Electron Screening

For a hadron of mass m and a single negative charge, states having a principal quantum number $n \leq n_{\text{max}} = \sqrt{m/m_e}$ lie within the electronic K-shell and screen one unit of nuclear charge from the orbiting electrons. Since there is little penetration of the electron densities to within the K-shell radius, the screening is almost exact and the electron density is nearly independent of the state of the orbiting hadron. The state of the hadron, however, is not independent of the electron density. Detailed calculations of the hadronic energy eigenvalues must incorporate the potential induced by the electronic charge density.

The electron density for radii within the K-shell is nearly independent of the ionization state of the outer electronic shells. Any inner shells which are ionized by an Auger transition are quickly refilled from the outer shells. Thus throughout the volume of space within the electronic K-shell the charge density of the electrons orbiting a hadronic atom of nuclear charge Z is, to within about three percent, equal to that of the $(Z-1)$ electrons orbiting a normal atom of nuclear charge $(Z-1)$ [1]. Any major differences between these two charge distributions occur well outside of the hadronic orbit and will affect the hadron energy only through the constant part of the

electrostatic potential. Such uncertainties in the potential are the same for all states of the hadron and are not reflected in the energies of the transition X rays. The potentials generated by electronic charge distributions of normal atoms have been calculated and tabulated in forms that are useful to exotic atom calculations [26].

1.2.2 Quantum Electrodynamic Corrections

The two basic types of quantum electrodynamic corrections applicable to calculations of the energy levels of exotic atoms are radiative effects and vacuum polarization. Radiative effects, sometimes known as self-energy corrections, result from interactions between the orbiting particle and the quantized radiation field. The main contribution to this interaction, the emission and re-absorption of a single virtual photon by the orbiting particle, gives rise to the well-known Lamb shift in the 2s state of hydrogen [27]. Although radiative processes may severely affect low-lying muonic states (greater than 3 keV for the 1s state of muonic W or Pb [28]), they play little part in the energy levels of hadronic atoms. The strong interaction usually results in absorption of hadrons in states which are still high-lying enough to be nearly devoid of radiative effects. Based on the methods of Rinker and Steffen [29], estimates of the first-order Lamb shift on the (9,8), (10,9) and (11,10) states of Ξ^- -Pb give respectively 1.6, 1.0 and 0.6 eV. Since much of this shift comes from a $(\vec{\sigma} \cdot \vec{L})$ term, the effect is generally much less for spinless particles. Estimates of the Lamb shift on the (7,6) and

(8,7) states of kaonic Pb are less than 1 eV. Radiative effects are generally ignored in this analysis.

Vacuum polarization, the emission and re-absorption of virtual electron-positron pairs by photons, is rarely if ever negligible in exotic atoms. Expressions for the polarization charge density generated by a point charge Coulomb potential have been derived [3] which show that the leading term in an expansion in powers of α gives the Uehling-Serber potential [30,31]. For exotic atoms of moderate to high Z this potential is too large to be treated by first-order perturbation theory. Although second-order theory is usually sufficient, a more practical approach frequently used is to include this potential in the eigenvalue problem, which is then solved numerically. Higher-order terms may be included either in the eigenvalue problem or evaluated later by first-order perturbation theory. Included in these higher-order terms are the $\alpha^2(Z\alpha)$ term first derived by Kallen and Sabroy [32] and the $\alpha(Z\alpha)^{3,5,7}$ terms derived by Wichman and Kroll [3]. Blomqvist [8] has organized the results of these authors into forms useful, if difficult, for computation and has provided expansions in powers of r valid near the origin. Unfortunately, the analytical expressions of Blomqvist are difficult to evaluate numerically and the expansions in powers of r break down beyond about 75 fm.

Based on Blomqvist's analytical expressions, Fullerton and Rinker [33] have derived parameterizations of the $\alpha(Z\alpha)$ and $\alpha^2(Z\alpha)$ terms, their integrals, and the second and fourth radial derivatives of the

$\propto(Z\alpha)$ term. These parameterizations are optimized in the Chebychev sense, so that the maximum error is minimized for the given number of parameters. The $\propto(Z\alpha)$ parameterizations are valid for all radii. The $\propto^2(Z\alpha)$ parameterizations are valid only for radii less than the electron's Compton wavelength λ_e , about 386 fm. An approximation is given for larger radii, but the potential is so small that it may usually be set equal to zero beyond λ_e with no effect on calculated results.

The $\propto(Z\alpha)^3$ vacuum polarization potential about a point charge has been evaluated by Vogel [26] using the expressions of Blomqvist [8]. Results are tabulated in a Z-independent manner over the range $0.1 \lambda_e < r < \lambda_e$. The results vary slowly with r , and so are easily interpolated. For $r < 0.1 \lambda_e$, the Blomqvist expansion in powers of r is preferable. The $\propto(Z\alpha)^{5,7}$ terms are generally assumed to have the same functional dependence as the $\propto(Z\alpha)^3$ term. Blomqvist has evaluated the leading terms in $1/r$ of these potentials, thus determining their relative magnitudes.

Finite nuclear size effects may be included in these vacuum polarization terms which are linear in the inducing charge Z simply by performing a linear convolution of the point-charge potential over the inducing charge distribution. For spherically symmetric charge distributions, this convolution may be greatly simplified at small radii by using the parameterizations of the potential integrals provided by Fullerton and Rinker [33]. At large radii, the $\propto(Z\alpha)$ potential for a finite nucleus may be expanded in terms of the first

few radial moments of the charge distribution and evaluated with the help of the parameterizations for the derivatives of the $\alpha(Z\alpha)$ potential.

Finite nuclear size effects are much more difficult to incorporate into the $\alpha(Z\alpha)^{3,5,7}$ potentials. A simple linear convolution is incorrect since the potentials are very non-linear in the inducing charge $Z\alpha$. Rinker, Willets and Steffen [9,29,34] have carried out direct numerical evaluations of the induced vacuum polarization charge densities about various nuclei of finite extent, using the so-called Schwinger prescription:

$$1.2-1) \quad \rho_e(\vec{r}) = (-e/2) \left[\sum_{\text{occ}} |\Psi_{\ell,k}^{\downarrow}(r)|^2 - \sum_{\text{unocc}} |\Psi_{\ell,k}^{\uparrow}(r)|^2 \right]$$

As can be seen in Figure 1, the exact results for ^{209}Pb deviate significantly from the point-charge and linear-convolution results for radii as large as 50 fm. The results of Rinker, Willets and Steffen [9,29] are tabulated only in the form of shifts to muonic atom energy levels. Although this is not directly useable, it does serve as a guide to a parameterization of this potential for general use. (See Appendix A.)

1.2.3 Nuclear Recoil

Classically, all effects of nuclear recoil on the energy eigenvalues are included by substituting the reduced mass for the hadron mass in the governing equations. Using a relativistic generalization of the reduced mass [35,36], one obtains an additional

shift $-B_0 / 2M_N$ which is of purely kinematic origin [20]. Here B_0 is the hadronic binding energy and M_N is the mass of the nucleus.

Nuclei of finite size have an additional effect first described by Breit [37], who pointed out that non-pointlike charge distributions moving at relativistic speeds suffer a rescaling of space as well as of time, and that the nucleus and the orbiting hadron, moving at different speeds, will have different rescaling factors. In an effort to avoid the treacherous Bethe-Salpeter equation, this problem has been approached by way of the scattering approximation [38-40] and a restricted version of the Breit equation [41] with essentially the same result; namely,

$$I.2-2) \quad \Delta E = (1/2M_N c^2) \langle h(r) + 2B_0 P_1(r) \rangle$$

$$\text{where } P_1(r) = -r\phi'(r) - \phi(r) \quad \text{for all } r \\ = 0 \quad \text{outside of the nuclear charge distribution}$$

$$\text{and } h(r) = -\phi''(r) - \frac{2}{r^2} \phi'(r) \int_0^r dx \, x^2 \phi(x) \quad \text{for all } r \\ = -\frac{Z\alpha \hbar c \langle r_N^2 \rangle}{3r^2} \phi'(r) \quad \text{outside of the nuclear charge distribution}$$

Note that $\langle r_N^2 \rangle$, the second radial moment of the nuclear charge distribution, vanishes for a point nucleus, so that $\Delta E(\text{point}) = 0$.

In addition, Salpeter [42], working through the Bethe-Salpeter equation, has derived an additional energy shift due to hole theory. Although these calculations have been carried out only for a limited set of cases [43], the effect is believed to be of the order of Zm/M_N times the first-order Lamb shift [20]. For kaonic and Σ^- atoms, the

total recoil correction is less than 10 eV for all but the most low-lying states.

1.2.4 Static Polarizability

Of all effects in hadronic atoms, polarization of the nucleus and of the orbiting hadron can be among the most difficult to calculate. In the rather extreme case of low-lying muonic or pionic states about high-Z nuclei, the orbital transition energies have magnitudes comparable to the excitation energies of the nucleus and, for pions, of the orbiting hadron. A considerable portion of the orbital wave function penetrates into the nucleus, so that a clear separation of the system into orbital, nuclear and hadronic components is not possible.

Ericson and Hufner [44] have shown that several simplifications can be made for most atoms formed with strongly-interacting particles other than pions. Apart from pions, which react mainly with nucleon pairs, most hadrons react with single nucleons at the nuclear surface and so are strongly absorbed before any significant penetration occurs. As a result, an expansion in terms of multipole moments of the time-dependent electric forces exerted on the hadron and on the nucleus by each other will be dominated by E1 (electric dipole) effects. The characteristic orbital frequencies of the hadron about the nucleus are small compared to those of the nucleons within the nucleus. The resulting static approximation allows closure over the atomic states, so that the second-order E1 energy shift due to

polarization of the nucleus

$$1.2-3) \quad \Delta E_{E1}^{NP} = -e^4 \sum_{A,Y} \frac{|\langle \phi_0^N | \vec{D} | \phi_p^N \rangle \cdot \langle \phi_0^H | \frac{\vec{p}}{Y} | \phi_Y^H \rangle|^2}{(\omega_p^N - \omega_0^N) + (\omega_Y^H - \omega_0^H)}$$

becomes

$$1.2-4) \quad \Delta E_{E1}^{NP} = -(\epsilon^2/2) a_{E1}^N \langle \vec{r}^{-4} \rangle_{n,l_0}$$

where

$$1.2-5) \quad a_{E1}^N = 2 \sum_p \frac{\epsilon^2 |\langle \phi_0^N | D_x | \phi_p^N \rangle|^2}{(\omega_p^N - \omega_0^N)}$$

is the nuclear polarizability. Here ϕ^N and ϕ^H are nuclear and hadronic wave functions, \vec{D} is the nuclear electric dipole operator and the expectation value $\langle \vec{r}^{-4} \rangle_{n,l_0}$ is taken over the hadronic eigenstate.

Ericson and Hufner [44] relate the nuclear polarization parameter a_{E1}^N to the energy-weighted (E1) photonuclear absorption cross section σ_{-2}^{E1} :

$$1.2-6) \quad a_{E1}^N = \frac{1}{2\pi^2} \sigma_{-2}^{E1} = \frac{1}{2\pi^2} \int \frac{\sigma_{E1}^-(\omega)}{\omega^2} d\omega$$

This relation is expected to be good to a few percent, approximately the same accuracy as the static approximation.

For nuclei heavier than argon, the total energy-weighted photonuclear cross section σ_{-2} may be approximated to better than 20 percent accuracy by

$$1.2-7) \quad \sigma_{-2}^- = 3.2 \times 10^{-6} A^{5/3} \text{ barn/MeV}$$

Assuming that $\sigma_{-2}^- \approx \sigma_{-2}^{E1}$, this gives $a_{E1}^N \approx 3.2 \times 10^{-3} A^{5/3} \text{ fm}^3$.

Equation (I.2-4) may be expanded to include polarization of the hadron by treating the hadron and the nucleus in a symmetric fashion:

$$I.2-8) \quad \Delta E_{E1} = -(\sigma^2/2) (\alpha_{E1}^H + Z^2 \alpha_{E1}^N) \langle r^{-4} \rangle_{n,l}$$

Very little is known [44] about the hadron polarizability parameter α_{E1}^H . Experimental results for the proton yield $\alpha_{E1}^P = (9 \pm 2) \times 10^{-4} \text{ fm}^3$ [45] and $\alpha_{E1}^P \leq 14 \times 10^{-4} \text{ fm}^3$ [46]. Calculations for the pion yield values ranging from $4 \times 10^{-3} \text{ fm}^3$ [47] to 10^{-1} fm^3 [48].

Relativistic effects are also considered by Ericson and Hufner, who find for the nucleus that

$$I.2-9) \quad (\alpha_{E1}^N)_{rel} = (\alpha_{E1}^N)_{n.r.} (1 + \bar{\epsilon}/M) + (Ze^2/3M) \langle r^2 \rangle$$

where $\bar{\epsilon} \approx -8 \text{ MeV}$ is the average nucleon binding energy and M is the nucleon mass. For $Z \approx A/2$ and $r \approx 1.2 A^{1/3} \text{ fm}$, equation (I.2-9) becomes

$$I.2-10) \quad (\alpha_{E1}^N)_{rel} \approx 3.4 \times 10^{-3} A^{2/3} \text{ fm}^3$$

Relativistic effects on the hadron are expected to be small compared to the overall uncertainties in the hadron polarizability. Since the polarization effect on hadronic atoms is generally small, equations (I.2-8) and (I.2-10) usually provide a sufficiently good approximation. In the absence of specific experimental evidence to the contrary, a hadron polarizability of $9 \times 10^{-4} \text{ fm}^3$ is assumed for this analysis.

A final effect considered by Ericson and Hufner is polarization of the electron cloud by the orbiting hadron. Here again a static approximation is possible, since the characteristic orbital frequencies of the electrons are typically larger than those of the hadron by at least an order of magnitude. The result is that the electron-screening correction (see section 1.2.1) is reduced approximately two percent by polarization effects [44].

1.2.5 Intrinsic Nuclear Multipole Moments

So far in this exposition, the theory has been developed only for nuclei possessing spherical symmetry, which is true for all but two of the isotopes used in this experiment. The nuclei $^{193}_{74}\text{W}$ and $^{207}_{82}\text{Pb}$ have nuclear spins of $1/2$ and nuclear magnetic dipole moments, respectively, of 0.1172 and 0.5895 in units of the nuclear magneton, μ_N . The first-order energy shift of a spin $1/2$ hadron due to a nuclear magnetic dipole moment $\mu = g\mu_N$ is found by evaluating the Dirac matrix element of the vector potential:

$$1.2-11) \quad \Delta E_{n,k} = \langle n,k | e\vec{\alpha} \cdot \vec{A} | n,k \rangle$$

where the $|n,k\rangle$ are eigenstates of the orbiting hadron and $\vec{\alpha}$ is defined in equation (1.1-13). Borie and Rinker [20] have evaluated this matrix element in the dipole approximation with the result

$$\begin{aligned}
 \text{I.2-12) } \Delta E_{n,k} &= \frac{4\pi k g \hbar^2}{(k-k_f) 2M_p} [\Delta(\Delta+1) - I(I+1) - J(J+1)] \\
 &\quad \times \int_0^\infty dr \frac{F_{n,k}(r) G_{n,k}(r)}{r^2} \int_0^r dx_N x_N^2 \rho(r_N)
 \end{aligned}$$

where M_p is the proton mass, \hat{I} is the nuclear spin and $\hat{A} = \hat{I} + \hat{J}$. $F_{n,k}(r)$ and $G_{n,k}(r)$ are the radial Dirac functions defined in equation (I.1-16).

The first-order energy shift of a spinless hadron is found in a similar manner. Letting E become $(E+\Delta E)$ and \vec{p} become $(\vec{p} - (e/c)\vec{A})$, the Klein-Gordon equation becomes:

$$\text{I.2-13) } \left[\frac{(E+\Delta E)^2}{c^2} - \left(\vec{p} - (e/c)\vec{A} \right)^2 - (mc)^2 \right] \Psi_{n,l} = 0$$

Subtracting equation (I.2-1) and dropping the $(\Delta E)^2$ and $|\vec{A}|^2$ terms, one obtains:

$$\text{I.2-14) } \Delta E = -(ec/E) \langle \Psi_{n,l}^r | \vec{p} \cdot \vec{A} | \Psi_{n,l}^r \rangle$$

In the dipole approximation about a spherically symmetric nucleus,

$$\text{I.2-15) } e\vec{A}(\vec{r}) = \frac{e\hbar^2}{2M_p} \int d^3 r_N \rho(r_N) \frac{\hat{I}_x(\vec{r} - \vec{r}_N)}{|\vec{r} - \vec{r}_N|^3} = \frac{2\pi g \hbar^2 (\hat{I}_x \vec{r})}{M_p r^3} \int_0^r dx_N x_N^2 \rho(r_N)$$

so that

$$\begin{aligned}
 \text{I.2-16) } \Delta E &= - \frac{2\pi g \alpha c \hbar^3}{EM_r} \langle \Psi_{n,\ell}^r | \frac{(\vec{I} \cdot \vec{L})}{r^3} \int_0^r dx_N x_N^2 \rho(x_N) | \Psi_{n,\ell} \rangle \\
 &= - \frac{2\pi g \alpha c \hbar^3}{EM_r} [\Delta(\Delta+1) - I(I+1) - \ell(\ell+1)] \int_0^\infty dx \frac{|R_{n,\ell}(r)|^2}{r^3} \int_0^r dx_N x_N^2 \rho(x_N)
 \end{aligned}$$

where the $R_{n,\ell}(r)$ are the solutions to the radial Klein-Gordon equation (I.1-6).

I.3 Transition Rates

I.3.1 Radiative Transition Rates

The radiative transition rate $R(b|a)$ is the probability per unit time (assumed independent of time) that an exotic atom in state $|a\rangle$ will de-excite to state $|b\rangle$ emitting a single photon of energy $E = E_a - E_b$ in the process. This rate may be calculated directly by the methods of quantum field theory [49] or indirectly by relating it to the Poynting vector of classical radiation theory [50]. The semi-classical calculation, although mathematically the simpler of the two, relies on a correspondence principle argument to relate the classical multipole moments to the matrix elements of the quantum mechanical multipole operator; i.e.,

$$I.3-1) \quad \text{Classical moment} \iff 2 \operatorname{Re}\{\langle b | \text{Quantum operator} | a \rangle \exp(iEt/\hbar)\}$$

For either method, calculation of the radiation (retarded) potentials at large radii may be simplified by expanding them in terms of the multipole moments of the charge distribution of the radiating system [51]. This leads to the familiar classification of radiation fields as E1 (electric dipole), E2 (electric quadrupole), M1 (magnetic dipole) and so forth. In this analysis it is generally not necessary to consider anything beyond the E1 rate, although for sake of completeness some formulas that follow are given also for E2 and M1 fields.

The transition rates for the first few multipoles are given by
 (52)

$$\begin{aligned}
 R_{E1}(nkm|n'k'm') &= \frac{4\alpha E^3}{3c^2 \hbar^3} |\langle nkm | \vec{r} | n'k'm' \rangle|^2 \\
 \text{I.3-2) } R_{E2}(nkm|n'k'm') &= \frac{\alpha E^5}{10c^4 \hbar^5} |\langle nkm | \vec{r} \vec{r} | n'k'm' \rangle|^2 \\
 R_{M1}(nkm|n'k'm') &= \frac{\alpha g_0^2 E^3}{3m^2 c^4 \hbar^3} |\langle nkm | \vec{L} + 2(1+g_1/g_0) \vec{S} | n'k'm' \rangle|^2
 \end{aligned}$$

where $\vec{r} \vec{r}$ is a second rank tensor.

If the orbiting particle is a fermion (spin 1/2) the angular quantum numbers k and k' are those of the Dirac theory (See equation I.1-16). For bosons (spin=0) k becomes the more usual orbital angular momentum quantum number l , and the operator \vec{S} in the R_{M1} matrix element of equation (I.3-2) is omitted. For either bosons or fermions m is the z-projection of the total (orbital+spin) angular momentum.

The transition rates (I.3-2) are calculated in the one-body reduced mass system of the Klein-Gordon or Dirac equation. Nuclear recoil can contribute significantly to the effective multipole moment of the hadron-nucleus system. A hadron-nucleus separation of \vec{r} gives an electric dipole moment $\vec{P} = -e \vec{r}$ in the reduced mass system, whereas the dipole moment in the lab frame has contributions from both the orbiting hadron and the nuclear recoil:

$$\text{I.3-3) } \vec{P} = (-e) \left(\frac{M_N}{m+M_N} \right) \vec{r} + (Ze) \left(\frac{-m}{m+M_N} \right) \vec{r} = (-e \vec{r}) \left(\frac{Zm+M_N}{m+M_N} \right)$$

It is thus seen that the transition rates (I.3-2) must contain the appropriate powers of the Fried-Martin factor [53]

$$I.3-4) \quad E = (Zm+M_M)/(m+M_M)$$

before they may be compared to experiment. $R_{E1}(b|a)$ is multiplied by E^2 and $R_{E2}(b|a)$ by E^4 . $R_{M1}(b|a)$ is unchanged.

If an atomic system reaches a state characterized by quantum numbers $(n'j'm')$ in some isotropic manner it is equally likely to be in any one of the $2j+1$ substates of azimuthal quantum number m' . There is likewise no preference in selecting the final substates (njm) other than that contained in the matrix elements.

The total transition rate

$$I.3-5) \quad R_{E1}(nj|n'j'm') = \sum_m R_{E1}(njm|n'j'm')$$

may be shown to be independent of m' [52]. It is this sum of transition rates which corresponds to the observed line intensities and state depopulation rates.

The operators which occur in the matrix elements of equation (I.3-2) may all be cast in the form $\mathcal{O} = R(r) \mathcal{O}(\theta, \phi)$, where $R(r)$ depends only on radial co-ordinates and $\mathcal{O}(\theta, \phi)$ depends only on angular co-ordinates, by the definitions

$$I.3-6) \quad \begin{aligned} x &= r \sin(\theta) \cos(\phi) = r \sin(\theta) [\exp(i\phi) + \exp(-i\phi)]/2 \\ y &= r \sin(\theta) \sin(\phi) = r \sin(\theta) [\exp(i\phi) - \exp(-i\phi)]/2i \\ z &= r \cos(\theta) \end{aligned}$$

$$xz = r^2 \sin^2(\theta) \cos^2(\phi)$$

$$1.3-7) \quad xy = r^2 \sin^2(\theta) \sin(\phi) \cos(\phi)$$

etc.

(Note: The M_l operators are already functions only of angular variables.)

If the eigenfunctions representing the initial and final states are also separable into radial and angular parts then these matrix elements may be evaluated in two parts, with any sensitivity to the form of the central potential appearing in the radial evaluation. Such a matrix element takes the form

$$1.3-8) \quad \langle n \ell m | R(\hat{H}) | n' \ell' m' \rangle = \langle Y_{\ell}^m | \hat{H} | Y_{\ell'}^{m'} \rangle \cdot \int_0^{\infty} (R_{n,\ell}(r))^* R_{n',\ell'}(r) dr$$

for the Klein-Gordon equation. The corresponding result for the Dirac equation is

$$1.3-9) \quad \langle n k m | R(\hat{H}) | n' k' m' \rangle = \langle \hat{H}_G \rangle \cdot \int_0^{\infty} (G_{n,k}(r))^* R_{n',k'}(r) dr \\ + \langle \hat{H}_F \rangle \cdot \int_0^{\infty} (F_{n,k}(r))^* R_{n',k'}(r) dr$$

where

$$1.3-10) \quad \langle \mathbb{H}_G \rangle = \text{Sign}(kk') \sqrt{\frac{(k-m+\frac{1}{2})(k'-m'+\frac{1}{2})}{(2k+1)(2k'+1)}} \langle Y_l^{m-\frac{1}{2}} | \mathbb{H} | Y_{l'}^{m'-\frac{1}{2}} \rangle \\ + \sqrt{\frac{(k+m+\frac{1}{2})(k'+m'+\frac{1}{2})}{(2k+1)(2k'+1)}} \langle Y_l^{m+\frac{1}{2}} | \mathbb{H} | Y_{l'}^{m'+\frac{1}{2}} \rangle$$

and

$$\langle \mathbb{H}_F \rangle = \text{Sign}(kk') \sqrt{\frac{(k+m-\frac{1}{2})(k'+m'-\frac{1}{2})}{(2k-1)(2k'-1)}} \langle Y_{l-\text{Sign}(k)}^{m-\frac{1}{2}} | \mathbb{H} | Y_{l'-\text{Sign}(k')}^{m'-\frac{1}{2}} \rangle \\ + \sqrt{\frac{(k-m-\frac{1}{2})(k'-m'-\frac{1}{2})}{(2k-1)(2k'-1)}} \langle Y_{l-\text{Sign}(k)}^{m+\frac{1}{2}} | \mathbb{H} | Y_{l'-\text{Sign}(k')}^{m'+\frac{1}{2}} \rangle$$

are the angular matrix elements. Here $\text{Sign}(x) = x/|x|$ for nonzero x . Note from the definitions of $R_{n,\rho}$ and $(E_{n,k}, G_{n,k})$ that the volume factor r^2 is already included in the radial integrals. In this way the radial system is made to appear truly one-dimensional, rather than as the radial part of a three-dimensional system.

The spherical harmonic angular elements $\langle Y_l^m | \mathbb{H} | Y_{l'}^{m'} \rangle$ appearing in equations (I.3-8) and (I.3-10) may be evaluated from the definition and orthogonality of the spherical harmonics [24]

$$1.3-11) \quad Y_l^m(\theta, \phi) = \frac{1}{\sqrt{2\pi}} e^{im\phi} P_l^m(\cos(\theta))$$

(The $P_l^m(z)$ are associated Legendre polynomials)

$$1.3-12) \quad \int_0^{2\pi} d\phi \int_0^\pi d\theta \sin(\theta) \left(Y_l^m(\theta, \phi) \right)^* Y_{l'}^{m'}(\theta, \phi) = \delta(m, m') \delta(l, l')$$

with the help of the identities [22]

$$\begin{aligned}
 \text{I.3-13)} \quad \sin(\theta) P_{\ell}^m(\cos(\theta)) \\
 &= \sqrt{\frac{(\ell+m+1)(\ell+m+2)}{(2\ell+1)(2\ell+3)}} P_{\ell+1}^{(m+1)}(\cos(\theta)) - \sqrt{\frac{(\ell-m)(\ell-m-1)}{(2\ell+1)(2\ell-1)}} P_{\ell-1}^{(m+1)}(\cos(\theta)) \\
 &= -\sqrt{\frac{(\ell-m+1)(\ell-m+2)}{(2\ell+1)(2\ell+3)}} P_{\ell+1}^{(m-1)}(\cos(\theta)) + \sqrt{\frac{(\ell+m)(\ell+m-1)}{(2\ell+1)(2\ell-1)}} P_{\ell-1}^{(m-1)}(\cos(\theta))
 \end{aligned}$$

and

$$\begin{aligned}
 \text{I.3-14)} \quad \cos(\theta) P_{\ell}^m(\cos(\theta)) \\
 &= \sqrt{\frac{(\ell+m+1)(\ell-m+1)}{(2\ell+1)(2\ell+3)}} P_{\ell+1}^m(\cos(\theta)) - \sqrt{\frac{(\ell+m)(\ell-m)}{(2\ell+1)(2\ell-1)}} P_{\ell-1}^m(\cos(\theta))
 \end{aligned}$$

Results pertinent to the evaluation of the E1 matrix elements are

$$\begin{aligned}
 \text{I.3-15-a)} \quad \langle \ell m | \sin(\theta) e^{i\phi} | \ell' m' \rangle \\
 &= S(m, m'+1) S(\ell, \ell'+1) \sqrt{\frac{(\ell+m)(\ell+m-1)}{(2\ell+1)(2\ell-1)}} - S(\ell, \ell'-1) \sqrt{\frac{(\ell-m+1)(\ell-m+2)}{(2\ell+1)(2\ell+3)}}
 \end{aligned}$$

$$\begin{aligned}
 \text{I.3-15-b)} \quad \langle \ell m | \sin(\theta) e^{-i\phi} | \ell' m' \rangle \\
 &= S(m, m'-1) - S(\ell, \ell'+1) \sqrt{\frac{(\ell-m)(\ell-m-1)}{(2\ell+1)(2\ell-1)}} + S(\ell, \ell'-1) \sqrt{\frac{(\ell+m+1)(\ell+m+2)}{(2\ell+1)(2\ell+3)}}
 \end{aligned}$$

$$\begin{aligned}
 \text{I.3-15-c)} \quad \langle \ell m | \cos(\theta) | \ell' m' \rangle \\
 &= S(m, m') S(\ell, \ell'+1) \sqrt{\frac{(\ell+m)(\ell-m)}{(2\ell+1)(2\ell-1)}} + S(\ell, \ell'-1) \sqrt{\frac{(\ell+m+1)(\ell-m+1)}{(2\ell+1)(2\ell+3)}}
 \end{aligned}$$

Note that these matrix elements are non-zero only for transitions with $\Delta\ell = +/-1$ and $\Delta m = 0$ or $+/-1$.

Equations (I.3-9), (I.3-10) and (I.3-15) all taken together yield the matrix elements $\langle x \rangle$, $\langle y \rangle$ and $\langle z \rangle$. The element $|\langle \vec{r} \rangle|^2$ which appears in equation (I.3-2) is then given by

$$I.3-16) \quad |\langle \vec{r} \rangle|^2 = |\langle x \rangle|^2 + |\langle y \rangle|^2 + |\langle z \rangle|^2$$

If a numerical procedure is used to solve the eigenvalue problem (I.1-4) then the radial integrals of equations (I.3-8) and (I.3-9) may be evaluated at the same time. In many cases this is not necessary. The radial matrix elements of the solutions to the Schrodinger equation for a non-relativistic spinless electron about a point proton have been evaluated analytically by Gordon [54] for the $\Delta l = 1$ transitions:

$$I.3-17-a) \quad \int_0^{\infty} \left(R_{n',l'+1}(r) \right)^* r \left(R_{n,l}(r) \right) dr = G(n,n',l)$$

$$\text{where } \frac{\alpha(-1)^{(n'-l)}}{(n'-l)!} \frac{[(n+l)! (n'+l-1)!]^{(l+1)} (4nn')^{(l+1)} (n-n')!}{4(2l-1)! [(n-l-1)! (n'-l)!] (n+n')^{(n+n')} (n-n')^{(2l-2)}}$$

$$G(n,n',l) = \frac{\alpha(-1)^{(n'-l)} [(n+l)! (n'+l-1)!]^{(l+1)} (4nn')^{(l+1)} (n-n')!}{4(2l-1)! [(n-l-1)! (n'-l)!] (n+n')^{(n+n')}} \quad \text{I}$$

$$\left\{ F \left[(l+1-n), (l-n'), 2l, \frac{-4nn'}{(n-n')^2} \right] - \left(\frac{n-n'}{n+n'} \right)^2 F \left[(l-1-n), (l-n'), 2l, \frac{-4nn'}{(n-n')^2} \right] \right\}$$

and $\alpha = (\hbar^2 / Zm_0^2)$. The F's are hypergeometric functions. This author has found a good approximation for the $\Delta l = +1$ transition matrix elements to be given by

$$1.3-17-b) \int_0^{\infty} \left(R_{n',l'}(r) \right)^2 r \left(R_{n,l}(r) \right) dr = \left(\ell+1/\ell \right)^{\frac{1}{2}} G(n',n,l+1)$$

These expressions may be scaled by m_e/ZM (m_e =electron mass, Z =nuclear charge number, M =hadron mass) to give an approximation that is frequently good enough for exotic atom calculations. Although derived for spinless 'electrons', equation (1.3-17) is also a good approximation for spin-1/2 electrons. In this case, $\ell=k-1/2$ retains its usual meaning as an orbital, rather than a total, angular momentum.

This approximation is more accurate for states of relatively large angular momentum. Such states have less penetration into the region near the nucleus where relativistic, finite nuclear size and vacuum polarization effects are more pronounced. For a given degree of accuracy desired in the rate calculation, it is found empirically that all transitions between states having ℓ greater than some minimum value may be evaluated using equation (1.3-17). The minimum value of ℓ depends on the accuracy desired and on the particular exotic atomic system, but is very insensitive to the principal quantum number n .

1.3.2 Auger Transition Rates

Auger transitions occur when the time-dependent potential generated by a relatively compact hadron-nucleus system induces a photoelectric absorption event in the surrounding electron cloud. Although the inducing radiation is incident on the electron cloud from

the inside instead of from the outside, the processes involved are very similar. Ferrell [55] has taken advantage of this similarity to relate the Auger rate $\Gamma_{\text{AUG}}(\omega)$ to the radiative transition rate $\Gamma_{\text{RAD}}(\omega)$ and the photo-absorption cross section $\sigma_{\text{pe}}^{(Z-1)}(\omega)$:

$$\text{I.3-18)} \quad \frac{\Gamma_{\text{AUG}}(\omega)}{\Gamma_{\text{RAD}}(\omega)} = \frac{\sigma_{\text{pe}}^{(Z-1)}(\omega)}{(Z-1)^2 \sigma_{\text{T}}}$$

where

$$\sigma_{\text{T}} = (8\pi e^4) / (3m^2 c^4) \text{ is the Thomson cross section.}$$

The radiative rate provides an estimate of the strength of the inducing potential. The photoelectric cross section gives an estimate of the rate at which an incident radiation field will induce electron excitations in a neutral $(Z-1)$ atom. A simple derivation of Ferrell's formula is included as an appendix by Leon and Soki [56].

The derivation of (I.3-18) assumes that electron depletion effects are not important. It is also limited to the dipole approximation, which is valid if the hadron-nucleus system is much smaller than the electronic K-shell radius. Exotic atoms in the radiative phase usually satisfy both of these requirements.

Several measurements and calculations of photoelectric cross sections have been reported. Storm and Israel [57], selecting calculations which best match experimental results, have tabulated these cross sections for $Z=1$ to 100 over the energy range (1 keV \rightarrow 100 MeV). Their results are expected to be accurate to within approximately three percent.

1.4 Initial Distribution

Very little is known experimentally about the distribution in angular momentum of an exotic atom in a specific state of principal quantum number n . In certain cases, intensities of X-ray transitions from states of equal n but having ℓ values which differ by one may be isolated (See Figure 2, e.g.; transitions A_0 and \mathcal{N}_1). In practice, these transitions are measurable only for states of maximum ℓ which lie well within the radiative zone (i.e., well within the electronic K-shell radius). Throughout this radiative zone both radiative and Auger transitions favor maximal changes in n but limit $\Delta\ell$ to ± 1 . The initial distribution in ℓ is thus shifted drastically toward larger values of ℓ by the time the hadron reaches the inner part of the radiative zone, and few details of the initial distribution survive in an identifiable form.

Barring any further information, the simplest assumption for an initial distribution in ℓ stems from the statistical distribution in which each state (n,j,m) is accorded equal weight independent of j and m . Since there are $2j+1$ such states for each level (n,j) , this gives a distribution $f(n,j) \propto (2j+1)$ which is frequently approximated by $f(n,\ell) \propto \ell$. Calculations based on the Fermi-Teller [58] model of atomic capture confirm a distribution approximately proportional to ℓ immediately after capture when the hadron is still high in the electron cloud [56]. Also according to the Fermi-Teller model, the

distribution in l does not change significantly as the hadron de-excites through the electron cloud.

Computer simulations of the quantum-mechanical cascade of a hadronic atom generally start with an assumed initial distribution in l or j at the radius of the electronic K-shell and then propagate this distribution to the lower-lying states via the Auger and radiative processes which dominate in the radiative zone. Since the transition from the conditions of large hadron-electron overlap where the Fermi-Teller model is applicable to the conditions of minimal hadron-electron overlap which characterize the radiative zone is actually rather gradual, the Auger and radiative processes (which shift the hadronic distribution towards larger values of l) have had at least some effect by the time the hadron reaches a radius small enough that the hadron-electron overlap may be ignored. The initial distribution assumed for such a computer simulation of the quantum-mechanical part of the cascade thus cannot be strictly proportional to l as predicted by the Fermi-Teller model, but must already show some shift towards larger values of l .

It has been found empirically from such computer simulations [59, also Section III.9 of this work] that the effects of Auger and radiative processes on a hadronic distribution in l may be well-approximated by a factor e^{al} , where a is generally positive and depends on the principal quantum number n as well as on the particular hadron-nucleus system under consideration. The initial hadron distribution at the radius of the electronic K-shell is thus

frequently assumed to have a form $\rho e^{a\ell}$ or $(2\ell+1)e^{a\ell}$ or $(2j+1)e^{a\ell}$, and the parameter a is then adjusted so that the predicted X-ray yields match the experimentally measured yields as closely as is possible.

A different approach is taken by Leon and Miller [60], who have developed a quantum-mechanical extension of the semi-classical Fermi-Teller model. In its simplest form, their fuzzy Fermi-Teller model yields results in most ways very similar to those of the Fermi-Teller model. It permits, however, the inclusion of an effective Fermi energy which modifies the hadron-electron interaction at hadron energies just below zero. The net result is a shift of the distribution toward lower ℓ which can, for rather extreme values of the Fermi energy, produce intensity fluctuations of the magnitude observed by Wiegand and Godfrey [59]. The form of the distribution in ℓ at the electronic K-shell given by this fuzzy Fermi-Teller model is still roughly linear in ℓ , but now with reduced slope and a non-zero (positive) value at $\ell=0$ (See Figure 3). There are many small fluctuations away from this essentially linear form, but they are expected to be averaged out in the radiative phase of the cascade and should have no significant effect on the observed X-ray intensities. It is unclear whether these fluctuations in the ℓ -distribution are physical in nature or are a manifestation of the calculation process employed by Leon and Miller.

The initial distributions used in this analysis combine these linear modifications to the statistical distribution with the more usual factor $e^{-a\ell}$, with the results

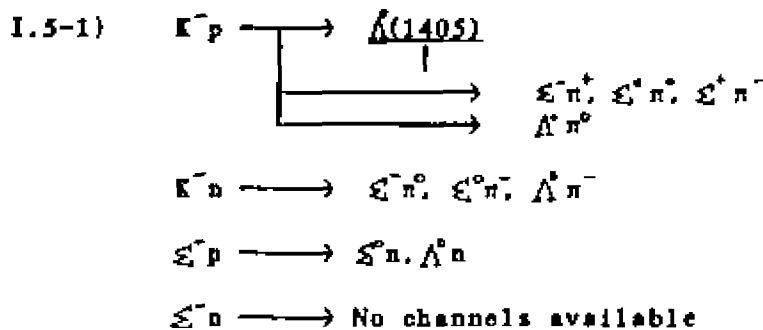
$$\begin{aligned}
 1.4-1) \quad f(n, \ell) &\propto [b(2\ell+1-n)+n] \exp(-a\ell) && \text{for spin}=0 \\
 f(n, j) &\propto [b(2j-n)+n+1] \exp(-a\ell) && \text{for spin}=1/2
 \end{aligned}$$

Here b and a are free parameters which may be adjusted to provide the best agreement between calculation and experiment. Typical values of b are slightly less than one, while a is generally in the range $0 < a < 0.2$.

1.5 Strong Interactions

The strong interaction differs in several important ways from any other interaction considered previously in this exposition. Since it is very short-ranged in nature (~ 1 fm), its effects are limited entirely to the neighborhood of the nucleus. For K^- and Σ^- , the strong interaction is thought to act independently between the hadron and each nucleon. This is not the general case, as pions interact mainly with nucleon pairs.

In addition to exerting forces, the strong interaction can mediate transformations of a hadron-nucleon system into some other system of particles as long as the appropriate conservation laws (isotopic spin, charge, parity, angular momentum, energy, baryon number, strangeness) are obeyed. The interaction channels which fulfill these conditions are:



It is generally accepted that strong-interaction effects in K^- and Ξ^- atoms may be adequately described by the inclusion of a complex local pseudopotential in the Klein-Gordon or Dirac equation for the orbiting hadron [61,62]. The real part of this pseudopotential describes the strong interaction forces exerted between the hadron and some time-averaged model of the nucleon distribution (static approximation). The imaginary part describes the absorption of the hadron by this time-averaged nuclear model through the strong interaction channels (I.5-1) listed above. The inclusion of a complex pseudopotential results in two immediate changes to the system of eigensolutions. Firstly, normalization is no longer conserved and, secondly, the energy eigenvalue takes on an imaginary component. Connecting these two facts by way of the Hamiltonian equation $E\Psi = i\hbar(\partial/\partial t)\Psi$, it is found that the normalization integral of an eigenstate having complex energy $E = E - i\Gamma/2$ decreases exponentially in time with characteristic time $\tau = \hbar/\Gamma$.

The most common form used for the strong-interaction pseudopotential is proportional to the nuclear matter distribution:

$$I.5-2) \quad V(\vec{r}) = -(4\pi\hbar^2/2\mu) (1+m/M_N) (\bar{a}_p \rho_p(\vec{r}) + \bar{a}_n \rho_n(\vec{r}))$$

where M_N is the nucleon mass, μ is the reduced mass of the hadron-nucleus system, \bar{a}_p and \bar{a}_n are strength parameters and $\rho_p(\vec{r})$ and $\rho_n(\vec{r})$ are proton and neutron matter distributions normalized, respectively, to Z and N . Since the poorly-known neutron distribution is usually assumed to be the same as the proton distribution, equation (I.5-2) is usually simplified to

$$I.5-3) \quad V(\vec{r}) = -(4\pi\hbar^2/2\mu) (1+m/M_N) \bar{a} \rho_N(\vec{r})$$

$$\text{where } \bar{a} = (Z/A)\bar{a}_p + (N/A)\bar{a}_n$$

$$\text{and } \rho_N(\vec{r}) = \rho_p(\vec{r}) + \rho_n(\vec{r})$$

Such a potential results from the first-order optical potential in Born approximation [63], and is usually justified by the short range of the strong interaction relative to the dimensions of the nucleus.

Deloff and Law [64] have folded an explicit finite-range K^- -nucleon potential into the ${}^4\text{He}$ matter distribution and fit the resulting differential cross section to experimental data. Their result for the range of the K^- -nucleon interaction is indistinguishable from the proton charge radius, supporting the use of the charge distribution rather than the matter distribution for the functional form of the K^- -nucleus potential.

In the most general case, the strength parameters \bar{a}_p and \bar{a}_n in equations (I.5-2) and (I.5-3) are free parameters to be fit to the data. They may be interpreted as effective K^- -p and K^- -n scattering lengths within the nuclear medium. In the commonly-used impulse approximation, they are replaced by the free scattering lengths extrapolated to threshold, a_p and a_n . Calculations based on the impulse approximation [65,66] are unable to reproduce adequately the experimentally-observed shifts in kaonic sulfur [67].

The strong energy dependence of the scattering lengths below threshold [68,69] due to the $\Lambda^{\circ}(1405)$ resonance has prompted Bardeen and Torigoe [70,71] to develop an energy-averaging technique which greatly improves the agreement between theory and experiment. Alternately, a development by Deloff [72] within the framework of Watson's multiple scattering theory [73] results in a simple relationship between the free and effective scattering lengths

$$1.5-4) \quad \bar{a}_{\beta n} = \frac{a_{\beta n}}{1 + (a_{\beta n}/bq)}$$

where bq is a range parameter approximately equal to 1.0 fm for most kaonic cases. This general relation avoids the impulse approximation by imposing the less radical coherent, or rigid, nucleus approximation for which nuclear excitations and polarization due to the K^- -nucleon interaction are ignored. Since the kaon reacts mainly with the periphery of the nuclear distribution, this approximation is expected to be quite good [71]. The specific cases calculated by Bardeen and Torigoe are reproduced to within roughly 20 percent by equation (1.5-4).

Most of the optical-model theory developed for kaonic atoms is expected to carry over to Σ^- atoms. There is some evidence [62, Table 5], largely inconclusive, that the range parameter bq for the Σ^- -nucleon interaction may be as small as 0.57 fm. A boson exchange model of the Σ^- -nucleon interaction [74] predicts saturation of the imaginary part of the potential at $\rho_N = 0.7 \rho_N(0)$. This is expected to be unimportant for low- to moderate- Z Σ^- atoms since the

Ξ^- -nucleus overlap function peaks far outside of the nucleus for all but the heaviest Ξ^- atoms. The same model predicts no significant nonlinear effects for the real part of the Ξ^- -nucleon potential.

The pseudopotential of equation (1.5-3) may be incorporated into the Klein-Gordon or Dirac equation as either a scalar added to the mass term or as the time component of a relativistic four-vector added to the Coulomb interaction term. Calculations by this author and others [71] show no significant difference between the two cases for kaonic and Ξ^- atoms. Since the potential is proportional to the charge distribution, it is assumed to be the time component of a four-vector for this analysis.

Chapter 11

EXPERIMENTAL METHOD

The data used in this analysis were collected during the course of Experiment 723 which was performed during parts of 1982, 1983 and 1984 at the Alternating Gradient Synchrotron facility of Brookhaven National Laboratory. The main purpose of Experiment 723 was to determine the magnetic moment of the Σ^- hyperon from measurements of the fine structure of the X rays emitted by high-Z Σ^- atoms. The experimental setup was thus designed to produce and identify Σ^- atoms and then measure the resulting de-excitation X rays.

Since Σ^- particles are too short-lived to survive transport over more than a few centimeters, they must be produced with a low kinetic energy at or near where the atoms are to be formed. This is usually accomplished by allowing K^- particles to interact with the nuclei of the target atoms. An intermediate product of this reaction is the production of many kaonic atoms and their de-excitation X rays.

The magnetic moment analysis requires knowledge of the relative populations of the individual levels involved in the fine-structure multiplets which are used for the determinations. It was thus necessary to measure as many as possible of the transitions leading into the multiplets. A relative efficiency-vs-energy calibration of the X-ray detection system was obtained so that the relative

intensities of these transitions could be determined.

Since the fine-structure splitting is greater for transitions involving lower principal quantum number n , the energy region over which X rays were measured included the final few transitions before the orbiting Σ^- was absorbed into the nucleus by the strong interaction. These final transitions are where strong interaction effects are most apparent in the atomic cascade. The same energy region also covers the final few transitions in the kaonic atomic cascade.

Thus the basic requirements of the magnetic moment experiment provided at the same time an excellent opportunity to study strong interaction effects on the de-excitation X rays of kaonic and Σ^- atoms.

II.1 Beam line

In slow extracted mode the BNL AGS required approximately 2 seconds to fill its ring with $\sim 10^{13}$ protons and accelerate them to a momentum of 28 GeV/c. Once the protons were brought up to speed and acceleration was discontinued, the slow extraction process diverted the protons down the beam lines to the production targets in a roughly uniform flow lasting from 600 to 1000 msec.

Figure 4 shows a diagram of production target C and the C4 beam line. At the C-Target Station, the beam of 28 GeV/c protons was focused so that a portion of them struck a two inch thick production target of either Cu or Pt. The remainder of the proton beam continued to other target stations. The interaction of the incident protons with the nuclei of the production target produced a wide spray of particles which for the most part continued in the same general direction as the proton beam. Included in this spray were hadrons such as the Λ , Ξ , K , p , n and π as well as leptons such as muons and electrons.

Bending dipole D1 was situated as closely as was possible to the remainder of the proton beam in order to steer the most intense part of the particle spray down the C4 beam line. Quadrupole magnets Q1 and Q2 controlled vertical and horizontal focusing, and were adjusted to collimate the beam of particles entering D2. Dipole bender D2 steered the beam into the separator. It could be turned off to allow

the beam to continue into a beam dump. This reduced radiation levels at the C4 experimental station to levels safe for access while the rest of C-line was delivering beam to the other experimental stations.

When D2 was turned on it steered the beam into the separator, deflecting more those particles with a lesser momentum so that there was a horizontal dispersion of momentum. In the separator, a vertical electric field was combined with a horizontal magnetic field so that any particles having velocity different from E/B were deflected vertically, resulting in a vertical dispersion of velocity.

Quadrupoles Q3 and Q4 focused the beam onto the mass and momentum slits. At the mass slit, thick horizontal jaws placed suitably in the vertically dispersed beam permitted transmission of any particles having velocity within about 0.1% of the central velocity. The electric and magnetic field strengths in the separator determined the central velocity. The width of the mass slit opening determined the allowed spread of velocities. In a similar manner, adjustments of D2 and of the vertical momentum jaws determined the central momentum and the spread of momenta which were passed through the beamline.

Quadrupoles Q5 and Q6 and dipole D3 served to transport the beam and re-focus it at the experimental station. D3 and Q6 had two mounting positions designed to provide beam to either the C-2 or the C-4 station. Only one of these stations at a time could receive beam. Figure 4 shows the configuration for delivering beam to the C-4 station.

For Experiment 723, the beam line was tuned to transport negatively charged particles with momenta of 680 MeV/c \pm 2%. The separator B-field was adjusted to pass particles having velocities characteristic of 680 MeV/c kaons. The mass slit width was adjusted to exclude as much as possible velocities characteristic of 680 MeV/c pions. A typical tune of the beam line showing the beamline elements, physical values and control system setpoints is given in Table I. For 4×10^{12} protons striking the C production target during a single 800 msec beam spill, about 6×10^4 K^- were delivered to a point approximately 1 meter downstream of Q6. The predominant contaminants were π^- , which outnumbered the K^- by about 10:1. In light of the fact that pions were produced much more copiously than were kaons and that only one kaon out of 19 survived decay while traversing the 15 meters from the production target to the final focus, this is considered good separation.

Q5 and Q6 were adjusted to focus the beam into a spot approximately 1.5 cm horizontal by 1.0 cm vertical (size extracted from a Monte-Carlo calculation) at a point 1.3 meters downstream from the exit window of Q6. In the process of passing through 14 cm of Cu moderator prior to focus, this spot size was smeared to approximately 5.5 cm horizontal by 4.5 cm vertical as measured at the hodoscope H (see Section II.2.2).

Table 1

C4 Beam Line Elements and Settings for 680 MeV/c K^-

<u>ID</u>	<u>Element</u>	<u>Set Point</u>	<u>Current/Opening</u>
D1	Dipole	2000	1999.0 A
Q1	Quadrupole	1826	1826.0 A
Q2	Quadrupole	470	351.8 A
D2	Dipole	1950	1217.0 A
B1	Separator Dipole	1680	638.7 A
Q3	Quadrupole	2568	1598.0 A
Q4	Quadrupole	1568	975.0 A
K1	Upstream Jaw	2440	OPEN
K2	Mass Slit Opening	2245	1.5 mm
K3	Mass Slit Rotation	2746	64° from beam
K4	Mass Slit Height	2050	-1.0 mm
K5	Downstream Jaw	2128	OPEN
Q5	Quadrupole	1888	889.2 A
D3	Dipole	1476	1477.0 A
Q6	Quadrupole	1448	1885.0 A

II.2 Target, Counters and Geometry

A view from above of the experimental arrangement for Experiment 723 is shown in Figure 5. For purposes of discussion the arrangement is divided into four functional groups: laminar target, KSTOP identification, pion spectrometer and X-ray spectroscopy system.

The laminar target, composed of thin metal plates suspended in liquid hydrogen, was designed to optimize both the production of Σ^- atoms subsequent to the stopping of a K^- within the target volume and the detection of the subsequent X rays by the spectroscopy system.

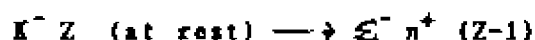
The KSTOP identification system identified those beam particles which had characteristics of K^- stopping within the target volume. It also provided a time-mark signal for entrance of beam particles into the front face of the laminar target.

The pion spectrometer was designed to detect and identify the π^+ resulting from Σ^- production within the target volume, with a bias towards those for which the Σ^- formed an exotic atom in the high-Z material of the laminar target.

The X-ray spectroscopy system measured the energy of X rays emerging from the bottom of the laminar target. It also provided a time-mark signal for the X-ray event.

II.2.1 Laminar Target

In previous Σ^- atom experiments the Σ^- have been produced by the reaction



within the target material. For high-Z atoms, calculations predict that this reaction has only a 5% branching ratio [75]. The comparable reaction in liquid hydrogen,



has a branching ratio of 44%. Experiment 723 therefore employed a novel approach to the target design. Thin sheets of the high-Z material (Pb, W, or U) were suspended vertically in liquid hydrogen and turned edgewise to the beam. The beam line was fine tuned to maximize K^- stops in the liquid hydrogen, thus maximizing Σ^- production.

Since the initial state for Σ^- production in hydrogen is a two body state at rest, the Σ^- and π^+ so produced were monoenergetic and had equal but opposite momenta of 173 MeV/c. The Σ^- were produced with a kinetic energy of 12.4 MeV and had a range in liquid hydrogen (assuming no decay) of 0.95 cm. Many of these Σ^- which were produced in the liquid hydrogen traveled to and stopped in a sheet of target material. The π^+ were produced with a kinetic energy of 82.6 MeV and usually exited the target volume.

A Monte-Carlo simulation was used to optimize the parameters in the target design. The sheet size, thickness and spacing were chosen to maximize the product of the probabilities that an incident K^- would stop in liquid hydrogen, that a Σ^- produced in liquid hydrogen would reach a sheet of target material to form an atom, and that the resulting X rays which travelled in the direction of the X-ray spectroscopy system would emerge from the target unabsorbed. Figure 6 shows side and end views of the resulting target. The sheets were spaced 0.46 cm apart and were 15 cm long. Their height ranged from 6.5 cm to 10.5 cm and their thickness was 0.035 cm for Pb, 0.020 cm for W and 0.018 cm for U.

The target assembly was encased in a cylindrical container of stainless steel 0.08 cm thick which was filled with liquid hydrogen. This in turn was suspended in a rectangular vacuum jacket constructed of 0.55 cm thick aluminum. A 0.22 cm thick window was milled into the front face of this vacuum jacket to allow the beam to enter with the least possible hindrance. A 0.33 cm thick window was milled into the bottom face of the vacuum jacket in order to reduce the material between the laminar target and the X-ray spectroscopy system. Mechanical design, construction and maintenance of the laminar targets used by Exp 723 was provided by the Hydrogen Target Group at BNL.

For the resulting design, a Monte-Carlo simulation predicted that 40+/-9% of the Σ^- produced in liquid hydrogen would travel in the proper direction and would survive decay or absorption for the time required to reach a target sheet and form an atom.

II.2.2 KSTOP Identification

Data simulations during the planning stages of the experiment demonstrated that maximizing the signal-to-noise ratio of the Σ^- atom X rays was of paramount importance to the determination of the magnetic moment. Since Σ^- atoms were formed only subsequent to the interaction of a K^- in the laminar target, great care was taken to design an experimental arrangement that was capable of differentiating between stopping kaons and the more numerous beam pions, which generally were far too energetic to be brought to a stop within the target volume. These beam pions produced many beam-coincident γ and X rays which could contribute to the radiation background in the energy region of the Σ^- atom X rays. Table II gives a listing of the beam-defining counters and their dimensions.

Counter Z, located just downstream of the mass slit, provided a time mark as far upstream as was possible. Unfortunately, design constraints for a counter which would function in this high radiation environment limited this counter to no more than 75% efficiency, making it useful only as a diagnostic tool.

Particles exiting Q6 were detected by a coincidence between counters S1 and S2. Next, counter \check{C} , a velocity-selective Cherenkov counter of the Fitch type [76], differentiated between the Cherenkov light of 680 MeV/c pions and kaons by detecting the difference in the angle of dispersion of the light. Light from the transit of a kaon

was totally internally reflected to a bank of six phototubes (RCA 8850). Light from a pion transit had a larger angle of dispersion due to the greater pion velocity, and so missed the critical angle for reflection. At a beam momentum of 680 MeV/c, best performance of this counter was obtained when a coincidence between any four or more of the six phototubes was required before a signal was generated. In this mode of operation, tests indicated a kaon detection efficiency of 94% and a pion rejection ratio of greater than 50:1.

Following the Cherenkov counter \check{C} , counter S3 detected particles entering the moderator. The moderator was a 14 cm thickness of Cu covering a 10 cm X 10 cm area. This was surrounded on the left, right, top, and bottom by a tunnel veto scintillator V_1 designed to detect any beam particles or their reaction products which exited the moderator in a direction divergent from the beam path. Monte Carlo simulations predicted that about 50+/-2% of the K^- entering the moderator would decay or interact within its volume.

Following the moderator, hodoscope H was used to measure the position and size of the beam spot. This hodoscope consisted of three vertical and four horizontal strips of 0.32 cm thick plastic scintillator overlapped to provide a spatial resolution of 5 bins horizontally and 7 bins vertically over the 10 cm X 10 cm area of the moderator's downstream face. A bit register was used to record the firing pattern of these counters, and this pattern was recorded as part of the event information.

The hodoscope was followed immediately by two thick plastic scintillators labeled in Figure 5 as S4 and S5. Counter S4 was viewed by two opposing phototubes connected to a mean-time circuit in order to provide the best possible determination of the transit time of a beam particle. Whenever timing signals were formed including a coincidence with S4, the leading edge of the S4 signal triggered the output so that the S4 signal set the time mark for the entire experimental arrangement. Combined with the early time-mark information from the Z-counter this gave time-of-flight information which generally provided the least ambiguous differentiation between 680 MeV/c pions and kaons. When the signal from the Z-counter was available its time relation to the S4 signal was digitized and recorded as part of the event information.

The kaons which passed through S4 and S5 had been slowed by the moderator to an average momentum of 280 MeV/c (Monte-Carlo calculation) with a rather broad spread from 180 to 360 MeV/c. At this momentum, the kaons deposited much more energy per unit length than did the pions, which were only slowed to a momentum of 490 MeV/c and were thus still minimum-ionizing. The phototube pulse heights from counters S4 and S5 were digitized and included as part of the event information. As can be seen in Figure 7, a clear separation was found between the signals from pions and those from kaons. A hardware discriminator threshold on S5 was set to 300 mv as indicated in Figure 7. Comparisons of the amplitudes of the S4 and S5 signals with the time-of-flight information when it was available showed that this threshold represented a 90% kaon detection efficiency and a pion

rejection ratio of 5.5:1.

As a further test that the kaon exiting the degrader actually stopped in the target, veto counter V_2 located approximately one meter downstream of the target was used to exclude particles which continued more or less straight through the target without stopping. Monte-Carlo calculations show that approximately 100% of the beam pions and less than 1% of the stopping kaons triggered this counter. The final K-stop signature was

$$S1 \cdot S2 \cdot \bar{C} \cdot S3 \cdot \bar{V}_1 \cdot S4 \cdot S5(\text{high}) \cdot \bar{V}_2$$

Figure 8 shows a diagram of the fast logic used to generate this stop signature, which was approximately 85% efficient and had a pion rejection ratio of at least 250:1.

TABLE II
Beam-Defining Telescope Counters

<u>Scintillation Counter</u>	<u>Dimensions (cm)</u>
S1	10.2 x 12.7 x 0.635
S2	10.2 x 12.7 x 0.635
S3	10.2 x 10.2 x 0.635
H (Hodoscope)	10.0 x 10.0 (5 bins horiz x 7 bins vert)
S4	10.2 x 10.2 x 0.635
S5	10.2 x 10.2 x 1.270
V ₁ (4 sides)	10.2 x 15.2 x 0.635
V ₂	30.5 x 30.5 x 0.635
<u>Cerenkov Counter</u>	<u>Dimensions (cm)</u>
\checkmark C (Lucite)	8.9 diameter x 1.27 thick

II.2.3 Pion Spectrometers

As shown in Figure 5, a set of scintillation counters and aluminum moderators was positioned on either side of the laminar target in an effort to detect the π^+ following Σ^- production in hydrogen. These arrays are labeled as the left and right pion spectrometers. The following discussion applies only to the left pion spectrometer. The right spectrometer is identical. A listing of the relevant elements and their dimensions is given in Table III. The associated electronics is shown in Figure 9, with a listing of the major logic signals and their composition in Table IV.

TABLE III

Pion Spectrometer Elements

<u>Element</u>	<u>Dimensions (cm)</u>
Counter L1	25.4 x 25.4 x 0.3175
Aluminum Degradar	45.7 x 45.7 x 4.13
Counter L2	45.7 x 45.7 x 0.635
Counter L3A	45.7 x 45.7 x 2.540
Counter L3B	45.7 x 45.7 x 2.540
Counter L3C	45.7 x 45.7 x 2.540
Counter L4	45.7 x 45.7 x 0.635

TABLE IV
Left Pion Spectrometer Logic Signals

<u>Signal Name</u>	<u>Logical Composition</u>
<u>Pion Signals</u>	
$L\pi_A$	$KS \cdot (L1) \cdot (L2) \cdot (L3A) \cdot (\overline{L3B})$ (Opens 10 μ sec $L\pi_A$ gate)
$L\pi_B$	$KS \cdot (L1) \cdot (L2) \cdot (L3A) \cdot (L3B) \cdot (\overline{L3C})$ (Opens 10 μ sec $L\pi_B$ gate)
$L\pi_C$	$KS (L1) (L2) (L3A) (L3B) (L3C) (\overline{L4})$ (Opens 10 μ sec $L\pi_C$ gate)
$L\pi$	$(L\pi_A) \text{ or } (L\pi_B) \text{ or } (L\pi_C)$
<u>Lo^+ Signals</u>	
$Lo^+ A_1$	$(L\pi_A \text{ gate}) \cdot (L2) \cdot (L3A) \cdot (\overline{L3B})$
$Lo^+ A_2$	$(L\pi_A \text{ gate}) \cdot (L3A) \cdot (L3B) \cdot (\overline{L2})$
$Lo^+ A_3$	$(L\pi_A \text{ gate}) \cdot (L3B) \cdot (L3C) \cdot (\overline{L3A})$
$Lo^+ A_4$	$(L\pi_A \text{ gate}) \cdot (L3A_{H3})$
$Lo^+ A$	$(Lo^+ A_1) \text{ or } (Lo^+ A_2) \text{ or } (Lo^+ A_3) \text{ or } (Lo^+ A_4)$
<u>Lo^+ Signals</u>	
$Lo^+ B_1$	$(L\pi_B \text{ gate}) \cdot (L3A) \cdot (L3B) \cdot (\overline{L3C})$
$Lo^+ B_2$	$(L\pi_B \text{ gate}) \cdot (L3B) \cdot (L3C) \cdot (\overline{L3A})$
$Lo^+ B_3$	$(L\pi_B \text{ gate}) \cdot (L2) \cdot (L3A) \cdot (\overline{L3B})$
$Lo^+ B_4$	$(L\pi_B \text{ gate}) \cdot (L3C) \cdot (\overline{L4}) \cdot (\overline{L3B})$
$Lo^+ B_5$	$(L\pi_B \text{ gate}) \cdot (L3B_{H3})$
$Lo^+ B$	$(Lo^+ B_1) \text{ or } (Lo^+ B_2) \text{ or } (Lo^+ B_3) \text{ or } (Lo^+ B_4) \text{ or } (Lo^+ B_5)$

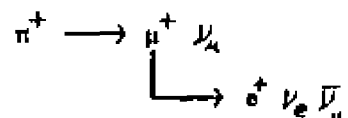
<u>Lo⁺ Signals</u>	
Lo ⁺ C ₁	(Lπ _c gate) · (L3B) · (L3C) · (<u>L4</u>)
Lo ⁺ C ₂	(Lπ _c gate) · (L3C) · (L4) · (<u>L3B</u>)
Lo ⁺ C ₃	(Lπ _c gate) · (L3A) · (L3B) · (<u>L3C</u>)
Lo ⁺ C ₄	(Lπ _c gate) · (L3C _{high})
Lo _c ⁺	(Lo ⁺ C ₁) or (Lo ⁺ C ₂) or (Lo ⁺ C ₃) or (Lo ⁺ C ₄)
<u>Any Lo⁺</u>	(Lo _A ⁺) or (Lo _B ⁺) or (Lo _C ⁺)

Right Pion Spectrometer signals are equivalent

When counter L3A was positioned 36 cm from the beam center line the left pion spectrometer package subtended a solid angle of approximately 9% as viewed from the center of the laminar target. In operation, π-stop signals Lπ_A, Lπ_B and Lπ_C indicated that particles originating in the laminar target in coincidence with a KSTOP signature passed through the aluminum moderator to stop in counter L3A, L3B, or L3C. During setup of the experimental apparatus, the thickness of the aluminum moderator was chosen to maximize the rate per KSTOP of delayed Lo⁺ signals following a π-stop in counter L3B. With 4.13 cm thickness of aluminum moderator in position, pions which exited the sides of the laminar target with kinetic energy ranges of (55-63), (63-70) and (70-77) MeV stopped in counters L3A, L3B and L3C. The π⁺ from Ξ^- production exit the laminar target with kinetic energies ranging from 65 to 79 MeV, depending on the production location within the target volume.

A survey of reactions resulting from stopping K^- showed that the particles most likely to be confused by the pion spectrometers with a π^+ accompanying Σ^- production were the π^- from the complementary production reaction $K^- p \rightarrow \Sigma^+ \pi^-$ and the π^+ and π^- from the Σ decays $\Sigma^\pm \rightarrow n + \pi^\pm$. Monte-Carlo calculations showed that the π^+ from the decay $\Sigma^+ \rightarrow n + \pi^+$ exited the side of the laminar target with kinetic energies ranging from 77 to 90 MeV. The pion spectrometers were thus fairly effective at distinguishing between these π^+ and the π^+ accompanying Σ^- production.

Signals characteristic of a delayed positron from the $\pi^+ \rightarrow \mu^+ \rightarrow e^+$ decay chain were used to distinguish between π^+ and π^- which stopped in the pion spectrometers. If the stopped particle was a π^- , it almost immediately formed a pionic atom and was absorbed into the nucleus. If the stopped particle was a π^+ , it remained in the interatomic spaces while it proceeded through the decay chain



The μ^+ in this reaction is produced with a kinetic energy of only 4.1 MeV and thus has a range of only 0.15 cm in the scintillator material. The light pulses produced by the μ^+ generally were not well-separated in time from those produced by the stopping π^+ , which has a mean life of only 26.030 ± 0.023 nsec [77].

The μ^+ has a mean life of 2.19714 ± 0.00007 μsec [78]. The delayed e^+ from the decay of a μ^+ is produced with kinetic energies ranging from 0 to 52 MeV, distributed in a Michel spectrum [79]. The Lo^+ logic signals listed in Table IV were designed to detect these delayed positrons. These signals were enabled for ten μsec following a π -stop signal. Any secondary KSTOP signature which occurred during this ten μsec gate generated a 50 nsec blanking circuit which inhibited the e^+ signals. This circuit served to protect against beam-coincident reaction fragments scattering into the rather large main counters L3A, L3B and L3C of the pion spectrometer, thereby producing false e^+ signals.

Any time a gated e^+ signal was generated, a bit register was set to indicate the spectrometer firing pattern. The time relationship of the e^+ signal relative to the π -stop signal which opened the gate was digitized. The time and bit-register information were recorded as part of the event information. Figure 10 shows a sample histogram extracted from the time relationship data. A least-squares fit of these data to a functional form consisting of a decreasing exponential and a flat background yields a lifetime of (2.26 ± 0.10) μsec , confirming that the e^+ logic signals are indeed mostly the result of μ^+ decays.

II.3 X Ray Spectroscopy System

II.3.1 Solid-State Detector Crystals

The fine-structure splitting of the final few X-ray transitions in $L^{\text{II}}\text{-Pb}$ and $L^{\text{II}}\text{-W}$ atoms ranges from 300 to 1000 eV. Bent-crystal spectrometers are capable of resolving doublet separations of less than one eV, but their very low inherent detection efficiency makes their use for the measurement of L^{II} -atom X rays impractical. Solid-state X-ray detectors can have absolute efficiencies of up to 20% and are capable of resolving doublets having separations of the same order as the $L^{\text{II}}\text{-Pb}$ and $L^{\text{II}}\text{-W}$ fine-structure splitting.

Silicon and germanium are two types of semiconductor materials which may be used for the construction of a solid-state X-ray detector. Both materials are usually doped, or drifted, with a uniform distribution of trace impurities which acts to improve the semiconductor performance. Germanium of sufficiently high purity (less than $1:10^{12}$ impurities) may show good semiconductor behavior with no need for the addition of impurities. High-purity germanium will generally have either slightly p-type or slightly n-type semiconductor properties. For Experiment 723, high-purity n-type germanium was chosen as the semiconductor material, both for its high photo-absorption efficiency relative to silicon in the 100 to 700 keV energy region and for its potential of improved resistance to, and

recovery from, radiation damage.

The static electrical configuration of a solid-state X-ray detector is that of a reverse-biased diode [80]. A semiconductor junction is formed in the detector material, and a biasing voltage is applied with the polarity which turns the junction off. This results in a dead region at the semiconductor junction where any free charge carriers are swept to one or the other side by strong electric fields. This dead region is the active volume for X-ray detection.

A constant fraction of the energy of a photon absorbed in the semiconductor material (as determined by the Fano factor of the material [81]) goes into the production of electron-hole pairs. Those pairs which are produced within the active volume are separated by the strong electric fields therein with a minimal amount of charge recombination, and the two types of charge carriers are transported rapidly to opposite sides of the junction. A charge-sensitive amplifier senses the momentary flow of current, integrating over some time interval which, ideally, is longer than the longest transit time experienced by any single charge carrier.

Imperfections in the crystal structure of the semiconductor material, such as the displacement of atoms out of their lattice sites, can cause a temporary trapping of otherwise mobile charge carriers. Such imperfections can be caused by a direct collision of an energetic massive particle with a nucleus of one of the atoms in the crystal. A large number of energetic neutrons and pions was produced by interactions within the moderator and the laminar target.

Thus, the solid-state detectors used in this experiment were subject to radiation damage of the crystal structure.

Extraction of fine-structure information from the Σ^- -Pb and Σ^- -W X-ray spectra collected with solid-state X-ray detectors involves a detailed analysis of a complex lineshape since the fine-structure components are not fully resolved. Such an analysis requires moderately high statistics in order to distinguish between small differences in the complex lineshape. The detector response to a monoenergetic X-ray transition should, as much as is possible, remain invariant over the duration of the data collection so that the data may be combined to achieve the necessary statistics. The expected ratio of energetic massive particles to Σ^- atom X-rays produced by Experiment 723 was large enough to cause serious degradation of the lineshape over the course of the experiment for any normal solid-state X-ray detector.

A novel reversed-electrode coaxial configuration which has been shown to be up to 28 times [82] as resistant to radiation-damage induced lineshape degradation as normal configurations was adopted for the X-ray detectors. In this configuration, an electrical contact is placed in a hole drilled along the axis of a cylindrically-shaped piece of high-purity n-type germanium such that the entire surface which was exposed by the drilling is maintained at constant potential. This contact is connected to the input of a charge-sensitive amplifier and its potential is maintained near electrical ground. The temperature of the crystal is maintained at 77K (as is necessary for

good operation of any germanium detector) and negative high voltage is applied to the outer surface, which has been implanted with acceptor-type impurities to form a thin layer of p-type material. This is known as a reverse-electrode configuration since most solid-state detectors have the charge-sensitive amplifier connected to the p-type bulk semiconductor and positive high voltage applied to the n-type implanted layer. The term coaxial refers to the cylindrical geometry.

The superior radiation-damage resistance of the reverse-electrode coaxial configuration can be attributed to the fact that electrons are less susceptible to charge trapping at lattice defects than are the effectively more massive electron holes, and to the fact that most of the active charge-collection volume is located nearer the outer (negative) terminal, where the electron holes are collected, rather than to the positive terminal, where the more mobile electrons are collected. Although the crystal structure itself is no less susceptible to radiation damage, charge collection, and thus the detector lineshape response, is much less sensitive to the presence of the trapping sites caused by radiation damage. This reverse-electrode configuration can be achieved only with an n-type semiconductor material such as high-purity n-type germanium. An added advantage of using a high-purity (i.e., undrifted) semiconductor material is that the radiation damage of the crystal structure may be largely repaired by annealing the crystal above 100 C, where increased mobility of the atoms allows the crystal lattice somewhat to reform itself. Drifted semiconductor materials cannot be successfully annealed, as the impurities tend to migrate to the surfaces.

There is an inverse relationship between resolution and efficiency in the design of solid-state X-ray detectors. Even at liquid nitrogen temperatures, the thermal vibrations of the crystal lattice can cause the occasional production of an electron-hole pair. These freed charge carriers are swept out of the active charge-collection volume by the biasing voltage, resulting in a flow of leakage current. Larger active volumes result in more of this leakage current, which can become a large contribution to the noise level in the charge-sensitive amplifier. The magnitude of the charge signal resulting from a photon-conversion event is relatively independent of the crystal size as long as the crystal volume is much larger than the cloud of electron-hole pairs produced in the neighborhood of the event. Resolution, a function of the signal-to-noise ratio in the charge-sensitive amplifier, is thus better for smaller active volumes.

In contrast, the absolute efficiency for detection of photons increases with active volume. Increasing the active thickness in the direction of photon propagation increases the probability that an incident photon will fully deposit its energy within the charge collection volume. Increasing the active area normal to the direction of photon propagation increases the solid angle subtended by the active volume as viewed from the source, thus increasing the chance that a photon leaving the point source in a random direction will intersect the active volume at some point.

The resolution-vs-efficiency tradeoff was weighed very carefully in the design of the X-ray detectors for Experiment 723. Fits of simulated datasets were used to compare the relative merits of improved resolution and of increased statistics in the determination of the magnetic moment. After lengthy consultations with the designers of the detector system (Lawrence Berkeley Laboratories and EG&G Ortec), a design was chosen which consisted of three coaxial high-purity (intrinsic) germanium detectors, denoted hereafter as detectors A, B and C, mounted in a reverse-electrode configuration on a common cryostatic cold finger assembly as shown in Figure 11. The physical characteristics of the three germanium crystals are listed in Table V. The different radii reflect the extremes of the anticipated region of optimization. The cylindrical axes of the crystals were oriented vertically and the mounting assembly was designed to leave the upper crystal faces exposed for best detection of photons impinging on the crystals from above. An aluminum vacuum jacket enclosed the entire three-crystal assembly. Windows 0.015 inches thick were milled into the top face of the vacuum jacket to minimize the amount of material traversed by an entering photon.

The datasets collected in 1982 showed that detector C's larger crystal size did not actually provide better statistics, as the higher rates in the larger active volume resulted in a larger percentage of dead time in the signal-processing electronics. The total amount of data collected from each of the three detectors was approximately equal, regardless of crystal size. Following the 1982 run, detector C's crystal was machined to the same dimensions as those of detectors

A and B. Subsequent to the 1982 and 1983 runs all three crystals were annealed in an effort to repair the lattice displacements due to radiation damage. Recovery of the original lineshapes was almost complete.

TABLE V
X-ray Detector Crystal Specifications

<u>Serial Number</u>	<u>Detector</u>	<u>Diameter</u>	<u>Length</u>	<u>Operating Bias</u>
701a	A	47 mm	26 mm	-2600 Volts
701b	B	47 mm	26 mm	-3600 Volts
708c	C			
	(1982)	57 mm	26 mm	-4000 Volts
	(1983-1985)	47 mm	26 mm	-4000 Volts

II.3.2 Signal Processing

Signal processing for the solid-state X-ray detectors employed in Experiment 723 was divided into three functional parts, as is usually the case for solid-state detector systems: charge-sensitive preamplifier, shaping amplifier and analog-to-digital conversion (ADC).

Charge-Sensitive Preamplifier

A block diagram of one of the charge-sensitive preamplifiers used in Experiment 723 is shown in Figure 12. An output voltage proportional to the charge present at point P is generated by a high-gain inverting amplifier connected in a capacitive-feedback configuration. In normal operation, reset transistor T is turned off. The leakage current of the detector crystal and the charges deposited by radiation events within the crystal result in a draining of (positive) charge from point P to the negative high-voltage supply. The resulting drop in voltage at point P drives the amplifier output voltage high, thus injecting charge into point P through feedback capacitor C.

For the idealized case of an amplifier A having frequency-independent gain $-a$,

$$\text{II.3-1) } V_{\text{OUT}} = -aq / (C_D + aC) \quad \text{and} \quad V_P = q / (C_D + aC)$$

where C_D is the effective capacitance of point P relative to ground. In the ideal case of $a \rightarrow \infty$, $V_{\text{OUT}} = -q / C$ and $V_P = 0$, making point P a virtual ground. In practice, C_D may be much larger than C and a may be only of the order of 10^3 so that the approximation $a \rightarrow \infty$ is not applicable.

The charge-to-voltage conversion factor $-a/(C_D + aC)$ should be maximized to provide best transmission of the signals from radiation events through any noise inherent in the preamplifier, the shaping amplifier or the ADC. An overriding consideration in many detector designs is thus to minimize C_D and C. Toward this end, and also to provide true charge sensitivity, a very high impedance field-effect transistor (FET) is generally used as the input device for the preamplifier.

For the configuration shown in Figure 12, the preamplifier output is a constantly-increasing voltage ramp (due to the detector leakage current) upon which is superimposed a series of positive step changes (less than 200 nsec rise time for Experiment 723) which are induced by radiation events. The amplitude of each step is proportional to the energy deposited by the inducing radiation event. The output of amplifier A has some finite dynamic range within which the output voltage is approximately proportional to the input voltage. Some provision must be made to deposit charge at point P in order to maintain output voltages within this dynamic range. Resistive

feedback was used in early solid-state detectors to establish some stable DC operating point, but such systems have difficulties maintaining this operating point at high rates. For most modern solid-state detectors, a pulsed-optical feedback system is used in which a light-emitting diode (LED) shines on the gate junction of the input FET to stimulate current flow (photodiode effect) whenever the preamplifier output reaches some pre-determined upper discriminator level. The gate current thus generated results in a rapid re-charging of point P, with a corresponding rapid fall in the preamplifier output voltage. Once a pre-determined lower discriminator level is reached, the LED is turned off and normal operation resumes. A logic signal indicating that a reset is in progress is usually used to disable the downstream signal processing electronics during resets.

Such a pulsed-optical reset system adds no extra capacitance or noise to the charge-sensitive stage and generally has good high-rate performance. It also may have several drawbacks. In certain cases, the FET may show some ringing after the LED is switched off. If the system is allowed to recover fully before signal processing is again enabled then dead times of 100 μ sec or more per reset may be introduced. Also, switching of the large currents (10's of mA) needed to drive the LEDs makes crosstalk a problem if several pulsed-optical reset detectors are to be mounted closely together in a single package as in Experiment 723.

With the proper choice of a reset transistor (i.e., minimum collector capacitance, among other properties) the transistor reset system shown in Figure 12 can be a reasonable choice for large coaxial detectors in which the input capacitance is already rather large. Deposition of the reset charge by a separate transistor eliminates long-term after-effects to the FET. Reset dead-times may thus be shortened for superior high-rate performance. In addition, a transistor reset system switches only a few μA of current. When several detector assemblies are mounted closely together in a common cryostat, this decreases the chance that a reset in one detector will generate a spurious signal in one of the other detectors.

The charge-sensitive preamplifiers used in Experiment 723 were constructed by Lawrence Berkeley Laboratory (model number 21X5911 P-1) and incorporated a transistor reset system as described in Reference [83]. The upper-level discriminator was set far enough below the upper limit of the preamplifier's dynamic range that events as large as 1.5 MeV in energy could be processed properly when superimposed on an output voltage ramp which was already near the upper discriminator level. The delay in triggering the reset (effected by the delay one-shot in Figure 12) once the upper level discriminator had been activated insured that the event which triggered the reset could still be processed, thus preventing a bias against events having larger energies.

Shaping Amplifier

Solid-state X-ray detectors have two principal sources of frequency-dependent noise [81]. Delta noise is concentrated at high frequencies. Its effects may be decreased by averaging (integrating) the input signal over some time interval. Increasing this time interval decreases the effects of this delta noise. Step noise is concentrated at low frequencies. As the integration time is increased, the contribution of step noise increases. There thus exists for all solid-state detectors some optimum amplifier shaping time for which the signal-to-noise ratio is maximized. This time is usually much longer than the time required for charge collection within the detector crystal.

Many different designs are possible for the shaping amplifier. The shaping amplifiers used in Experiment 723 (LNL Model 11X8481 P-5) employ a Gaussian shaper consisting of a single RC differentiator followed by multiple RC integrators. The same RC time constant is used for both the differentiator and for all of the integrators. The response to a step input of such a shaper having N stages of integration is a pulse of the form

$$\text{II.3-2) } V(t) = (t/RC)^N \exp [N(1-t/RC)]$$

This pulse shape has the advantage of being rather broadly peaked while still returning to the signal baseline rather rapidly after the peak. The broad maximum helps reduce sensitivity to fluctuations in collection times. The fast return to baseline allows sequential pulses to be processed with a minimum of interference. For the

shaping times employed in Experiment 723, the output of the Gaussian shaper peaked nine μsec after the input step (rise time) and returned to baseline within 14 μsec after the peak (fall time).

An additional function of the shaping amplifier was to monitor the time separation of the input pulse train to prevent the processing of events which occurred closely enough in time to interfere with each other. The shaping amplifiers used in Experiment 723 incorporated pulse-pileup rejection circuitry which included a fast timing channel and logic elements which inhibited the slow-shaping channel for any pulses which were preceded by 14 μsec or less (one fall time) by another pulse or which was succeeded by another pulse before the Gaussian pulse-shape had reached its maximum.

A peak-detect circuit monitored the Gaussian-shaped pulse, activating a stretcher amplifier when a peak was detected and no pulse pileup or reset inhibitions were in effect. A Valid Out signal, activated at the same time as the stretcher amplifier, gated the stored voltage to the final output for two μsec , providing the usual flat-topped pulse to the ADC.

Some refining points of the shaping amplifier included a baseline restorer which insured that the stretcher amplifier output returned properly to ground in the quiescent state and an offset bias which could be applied to the output gate. The overall gain of the shaping amplifier was distributed into several moderate gain stages for improved overload recovery. Gain switching was effected at several points throughout the series of gain stages for optimum signal-to-

noise performance.

Analog-to-Digital Conversion

Analog-to-digital conversion of the X-ray detector signals in Experiment 723 was via LeCroy CAMAC ADCs (Model 3511). These 13-bit ADCs converted input voltage pulses ranging from 0 to 8 volts in amplitude to digital binary numbers ranging from 0 to 8000 by a method of successive approximations wherein the output of a 13-bit digital-to-analog converter (DAC) is compared to the input voltage and the binary input to the DAC is adjusted one bit at a time (starting with the most significant bit) to provide the best possible agreement between the voltage input to the ADC and the voltage output of the DAC. Such a method requires only one sampling per bit decision and is capable of very rapid conversion. The LeCroy 3511 ADC performs a full 8000-channel conversion in only 5 μ sec. By comparison, as much as 80 μ sec is required for ADCs of the Wilkinson run-down design when incorporating a 100 MHz run-down clock. For the event rates anticipated in Experiment 723, the rapid conversion times permitted by the successive-approximation method were essential.

Typically for ADCs of either the successive-approximation or of the Wilkinson rundown designs, the input voltage is held in a stretcher amplifier while conversion takes place. Such voltage storage devices are never perfect. This, coupled with the fact that the conversion time of an ADC of the Wilkinson run-down design is roughly proportional to the signal amplitude, can result in serious integral non-linearities for ADCs of this design. The conversion time

of a successive-approximation ADC such as the LeCroy 3511 is independent of the signal amplitude, resulting in superior integral linearity characteristics. Differential non-linearities (bin-to-bin fluctuations in the binwidth) are more of a problem for successive-approximation ADCs. The LeCroy 3511 uses a bin-averaging technique to greatly improve the differential linearity response. A digital-to-analog converter (DAC) converts the content of an offset register to a voltage which is added linearly to the ADC input before digitization. The conversion gain of the DAC is adjusted so that one least-significant-bit change of the content of the offset register results in a 0.5 mV change in the DAC output voltage. This corresponds to one-half of a bin of the ADC output. After digitization, the content of the offset register is divided by two and subtracted from the result of the successive-approximation digitization procedure by the internal logic of the ADC. It is then incremented by one and, if greater than 383, reset. This results in an averaging of the ADC response over 191 successive bins, a procedure which smooths out most differential non-linearities present in the successive-approximation ADC.

Several modifications were made to the Model 3511 ADCs used in Experiment 723. The voltage reference for the virtual ground established by the bi-polar power supplies of the linear input stage was derived from the shield of the coaxial cable carrying signals from the shaping amplifier rather than from the CAMAC ground in the logic section of the ADC. This technique eliminated ground-loop pickup of the 60 Hz magnetic fields produced by nearby power supply

transformers. Bypass capacitors shunted any high-frequency transients on this virtual ground to the CAMAC ground in the logic section of the ADC. A careful survey of the logic functions performed within the 3511 ADC revealed several cases in which logic levels changed unnecessarily during the conversion procedure. Such level transitions were found to cause some severe differential non-linearity which could not be satisfactorily removed by the offset register system. Some portions of the logic circuitry which were unused in the application of Experiment 723 were disabled and some logic circuitry which was essential for Experiment 723 were modified so that there was no unnecessary switching of logic levels during the conversion procedure. Finally, an emitter-follower current amplifier was added to the output stage of the DAC used for the offset register conversion, reducing the sensitivity to switching transients during conversion and further improving the differential linearity. The resulting differential non-linearities for the ADCs used in Experiment 723 were less than 0.5 % when the offset register system was enabled.

II.3.3 Interconnections and Operation

An interconnection diagram for the various components of one of the X-ray detector systems used in Experiment 723 is shown in Figure 13. The gated output of the shaping amplifier had a rather slow exponential rise time. The Valid Out signal from the shaping amplifier was used to switch the input track-and-hold stage of the ADC from track to hold one μ sec after the start of the two- μ sec long output pulse. This insured that the voltage to be converted was always sampled from the same point on the gated output pulse shape.

The terminating resistor at the input of the shaping amplifier was changed so that the combined loads of the timing filter amplifier (TFA - Ortec Model 454) and of the shaping amplifier resulted in proper termination of the signal cable from the preamplifier. The output of the TFA was monitored by a constant-fraction discriminator (CFD - Ortec Model 473a) which provided a time mark with approximately ± 10 nsec stability relative to the inducing radiation event (See Figure 14). Coincidences within 40 nsec of this time-mark signal with the KSTOP signature from the beam-defining counter telescope (EVENT GATE) were used to enable the gate generator which controlled the ADC conversion strobe. An additional condition on these enabling signals was a $\overline{\text{BUSY}}$ signal from the data acquisition system, indicating that the system was ready to accept an event.

The detector assembly, including detector crystals, charge-sensitive preamplifiers, cryostatic cold finger and liquid nitrogen dewar, was located in an enclosed, insulated and thermally controlled housing beneath the laminar target. The remainder of the electronics shown in Figure 13 was housed in a separate temperature-controlled environment approximately eight meters to one side of the beam line. The digital outputs of the ADCs were transmitted to the experimental trailer on a standard 100 ft long CAMAC branch highway.

Despite the elaborate temperature controls employed in Experiment 723, the data collected in the 1982 run showed a disappointing dependence on the ambient temperature in the experimental area. The problem was found to be in the signal cables connecting the preamplifiers to the shaping amplifiers. These cables were of a type exhibiting unusually high DC resistance for the eight-meter length employed. This resistance, forming a voltage divider with the terminating resistor at the input of the shaping amplifier, was prone to vary with fluctuations in the ambient temperature. In subsequent runs (1983 and 1984), these eight-meter signal cables were replaced with cables made of the less resistive RG58U and were routed through a 1.25 inch inner diameter pipe wrapped with fiberglass insulation. Air from the temperature controlled environment housing the shaping amplifiers and ADCs was forced along the length of the pipe and vented just short of the temperature-controlled housing for the detector assembly. The data collected in these subsequent runs were found to be much less sensitive to fluctuations in the ambient temperature.

II.4 Data Acquisition

Measurement devices conforming to the CAMAC engineering standard [84] were used for data acquisition in Experiment 723. The various devices were mounted in three standard CAMAC crates providing power and connections to a local data-bus. Each of these local data buses was interfaced to a standard CAMAC branch highway by means of a type A-1 crate controller. A listing of the device configuration for each crate is given in Table VI.

Operations on the CAMAC branch highway were overseen by a Multi-programmable Branch Driver (MBD) [85]. This MBD was connected with direct memory access to the Unibus of a Digital Equipment Corporation PDP-11/34 computer which served to initialize, download and control the MBD, oversee the writing of data tapes, and perform online data analysis for diagnostic purposes.

TABLE VI
CAMAC Crate Configuration

<u>Crate</u>	<u>Modules</u>	<u>Function</u>
1	WM Trigger Module Pattern Bit Register Pattern Bit Register TDC (100 nsec) Charge Sensitive ADC Pattern Bit Register Pattern Bit Register TDC (10 μ sec) Charge Sensitive ADC	DA Synchronization Event Decoding Hodoscope Pattern KS \rightarrow γ time/K TOF dE/dX (S4,S5) L α^+ decay pattern R α^+ decay pattern KS \rightarrow e $^+$ time e $^+$ energy
2	Scalars (48 in 10 units)	Scale inputs/LAM on overflow
3	Spectroscopy ADCs (3)	Energy in detectors A, B or C

The fundamental data unit in this experiment, whether from a hardware or from a software perspective, was referred to as an event. A hardware event occurred whenever the data acquisition system was ready to accept an event and a radiation pulse occurred in one of the three X-ray detectors, in coincidence with one of three conditions (See Figure 15):

1. K-stop - An 80-nsec gate opened by the KSTOP signal. Propagation delays were adjusted so that the peak of the KSTOP-to- γ timing distribution occurred 30 nsec into the gate (See Figure 14).
2. Beam- π - A 1.0-to-1.5 μ sec gate (varied with the calibration sources) opened by a signal characteristic of beam pions passing through the entire beam counter telescope without stopping.

3. Beamoff - A continuous coincidence with a signal from the AGS control room which indicated that no beam was being delivered.

Hardware events were classified as $KS\gamma$, Beam-On or Beam-Off depending on the coincidence condition. All data events were classified as $KS\gamma$ events. The Beam-On and Beam-Off events were used for calibration purposes only.

Moderate-intensity ($\sim 1 \mu\text{C}$) sources of γ rays of well-known energies [86,87] were positioned on the bottom face of the aluminum vacuum jacket which housed the laminar target. The sources employed here and the energies of their dominant photon emissions are given in Table VII. The sources were selected to provide calibration lines close to the Σ^- atom transitions used in the magnetic moment analysis without interfering with any of the Σ^- atom or kaonic atom X rays.

Table VII
Calibration γ -ray Source Energies

<u>Source</u>	<u>γ-ray Energy (keV)</u>	<u>Used with Target(s)</u>
^{57}Co *	122.063 ± 0.003	Pb, W, U
	136.476 ± 0.003	
^{133}Ba *	276.397 ± 0.012	Pb
	302.839 ± 0.008	
	356.005 ± 0.017	
	383.851 ± 0.020	
^{192}Ir **	205.79549 ± 0.00007	W
	295.95825 ± 0.00001	
	308.45689 ± 0.00001	
	316.50789 ± 0.00001	
	468.07147 ± 0.00027	
^{198}Au **	411.80441 ± 0.00001	U
^{51}Cr **	320.076 ± 0.006	U
^{137}Cs **	661.661 ± 0.003	Pb, W, U
* Reference [87]		
** Weighted mean of values from Reference [86]		

The probability that a photon from one of these calibration sources would make an accidental coincidence with the KSTOP signal was rather small owing to the short duration (80 nsec) of the KS- γ coincidence gate. There was thus little leak-through of the calibration lines into the data spectra. Detector events which made a coincidence with the BEAM- π gate included some background events which

were induced by the triggering beam pion and some random coincidences of calibration photons with the rather wide (1.5 μ sec) gate. These Beam-On calibration data were used to monitor the energy calibration and detector lineshape under beam conditions. Detector events which made a coincidence with the BEAM-OFF gate were almost exclusively calibration photons. These events were used to monitor the temperature stability of the X-ray spectroscopy system in a software-implemented two-point stabilization scheme which was incorporated into the data tape playback (See section III.2).

Diagrams of the event-selection logic and the event gating are shown in Figures 15 and 16. The Trigger Module shown in Figure 16 was a specially fabricated CAMAC unit responsible for the synchronization of hardware and software elements of the data acquisition system. When the system was ready to accept an event the logic level $\overline{\text{BUSY}}$ was asserted. The next valid event pulse triggered the module which then immediately de-asserted $\overline{\text{BUSY}}$, disabling the further acceptance of events. After a delay of approximately 15 μ sec (designed to allow proper signal shaping and ADC conversion in the X-ray spectroscopy system), the Trigger Module issued a Look At Me (LAM) to the MBD which then responded by processing the event.

After the MBD had finished processing the event and the spectroscopy ADCs had been cleared by CAMAC control, the data acquisition software resident in the MBD issued a CAMAC F16 command to the Trigger Module which responded by generating a NIM-standard pulse from the CLEAR output. This pulse was distributed to the EXTERNAL

CLEAR inputs of all of the other CAMAC units mounted in Crate #1. Finally, the event-processing routine reset the Trigger Module (re-asserting the $\overline{\text{BUSY}}$ output level) and returned to a quiescent state until re-activated by another LAM.

In the 1983 and 1984 runs a LAM inhibit input was added to the Trigger Module. The BUSY outputs of the spectroscopy ADCs were combined to hold the LAM inhibited unless one or more of the ADCs was converting a pulse within its valid input range. At the end of the 15 μsec LAM delay period the Trigger Module sampled the logic level at the inhibit input and issued either a LAM to the MBD or a CLEAR to the fast-clear fanout unit. If no LAM was issued, the trailing edge of the CLEAR pulse was used to re-assert the $\overline{\text{BUSY}}$ output of the Trigger Module, re-enabling event acceptance. This modification was found to improve overall system throughput since many of the beam-induced radiation events generated very large pulses from the passage of charged particles through the crystal volume. Such events could trigger the data acquisition system even though their energy was far above the upper limit for conversion by the ADCs. Each of these false triggers introduced at least 35 μsec dead time while the acquisition software decided that the event was not valid and executed its reset procedure.

Once the LAM-driven MBD-resident event processing software was activated, its first action was to read the event pattern unit shown in Figure 16. One of several options was selected for the event-handling procedure, depending on the bit pattern found in this unit.

K Σ events and Beam-On events were handled in approximately the same manner; namely, a number of CAMAC units were read and a software event, consisting of a header and a number of data words, was constructed and appended to a buffer resident in the memory of the PDP-11. The event header contained, in addition to information on the total number of data words comprising the event, an event number which differentiated among types of events as shown in Table VIII. The CAMAC units read and included in each class of event are shown in Table IX. The Multiple event type shown in these tables occurred when, within a given K-STOP coincidence gate (KS fanout, Figure 15), events were detected in more than one of the detector crystals or both pion spectrometers registered a stopping pion. In this case, all of the CAMAC units were read and their outputs recorded. A considerable portion (up to 25%) of the data acquisition system's capabilities went into processing these Multiple events, which were subsequently found to contain almost no useful data. The data acquisition software was thus modified following the 1982 run so that the occurrence of a Multiple event triggered a fast reset of all CAMAC units, with no information being read or recorded.

Table VIII
Software Event Types

<u>Event Number</u>	<u>Event Type</u>	<u>Trigger</u>
70	ON.A	BEAM-ON
80	ON.B	BEAM-ON
90	ON.C	BEAM-ON
100	RAW.A	KS · γ_A
110	RAW.B	KS · γ_B
120	RAW.C	KS · γ_C
130	CLEAN.A	KS · $\gamma_A \cdot L\pi_A$
131	CLEAN.A	KS · $\gamma_A \cdot L\pi_B$
132	CLEAN.A	KS · $\gamma_A \cdot L\pi_C$
133	CLEAN.A	KS · $\gamma_A \cdot R\pi_A$
134	CLEAN.A	KS · $\gamma_A \cdot R\pi_B$
135	CLEAN.A	KS · $\gamma_A \cdot R\pi_C$
	(and similarly)	
140-145	CLEAN.B	KS · $\gamma_B \cdot (L\pi_A \rightarrow R\pi_C)$
150-155	CLEAN.C	KS · $\gamma_C \cdot (L\pi_A \rightarrow R\pi_C)$
160-165	TAG.A	KS · $\gamma_A \cdot (L\pi_A \rightarrow R\pi_C) \cdot e^+$
170-175	TAG.B	KS · $\gamma_B \cdot (L\pi_A \rightarrow R\pi_C) \cdot e^+$
180-185	TAG.C	KS · $\gamma_C \cdot (L\pi_A \rightarrow R\pi_C) \cdot e^+$
190	Multiple	KS · (> one γ) or KS · γ · (> one n)

Table IX
Event Information

<u>Event Type</u>	<u>Recorded Information</u>
TAGGED	1) Event Header 2) Detector Energy 3) Hodoscope Pattern 4) KS- γ timing 5) dE/dX S4 (A+B) 6) dE/dX S5 7) Kaon TOF 8) σ^+ Decay Pattern 9) KS \rightarrow σ^+ timing 10) σ^+ Energy
CLEAN	1-7 above
RAW	1-7 above
MULTIPLE	Header + all CAMAC words
Beam-On	1-2 above

If a Beam-Off event was indicated by the event pattern unit, then only the appropriate spectroscopy ADC (as indicated by the A,B,C bits of the event pattern unit) was read. The resulting number was used to increment one of six Beam-Off histograms resident in the memory of the MDD. Each of these histograms, two for each detector, was 60 bins wide and was respectively centered on the 122 keV line of ^{57}Co and on the 662 keV line of ^{137}Cs . The gain and offset of the X-ray spectroscopy system were adjusted so that these lines fell approximately at channels 500 and 6500 of the spectroscopy ADC's 8000-

channel conversion range. For the 1983 and 1984 runs the upper histogram for each detector was binned by two by the MBD software so that an effective interval of 120 channels of the ADC output range was monitored.

Periodically (usually once every ten minutes), the PDP-11 set a Flush Pending flag in the MBD memory. The next time that a Beam-Off event was processed and sufficient buffer space remained in the memory of the PDP-11, a Beam-Off software event (event number 50) was appended to the data stream. This event consisted of a header and the contents of the six windowed Beam-Off histograms. The first channel of each histogram was overwritten with the ADC output value which had caused that first channel to be incremented. This offset value could be changed by commands from the data acquisition control software. Upon successful transfer of the Beam-Off histograms to the buffer in the PDP-11, the MBD cleared the histogram area in its internal memory and reset the Flush Pending flag.

The data buffer in PDP memory was 4096 (16-bit) words long. Once this buffer was filled, the MBD issued an AST-level interrupt (Asynchronous Service Trap) to the PDP-11 and went into a dormant state. The interrupt activated an AST service routine installed in the PDP-11 which transferred the data buffer to tape and re-activated the MBD, initializing its buffer pointer to indicate a fresh buffer. The AST service routine also passed the first 1024 words of the data buffer to the analysis software for online diagnostic analysis.

Two similarly-configured PDP-11/34 computers were installed for Experiment 723. Each consisted of a CPU, a hardware floating-point processor, 128K words of RAM, several 2.2 Megabyte-capacity RK05 hard disk drives, one or more tape drives, a console printer, a Tektronix 4010 graphics terminal, and several additional CRT-display terminals. One of the PDP-11's was used for data acquisition and the other was used for immediate offline analysis of data tapes. Additional devices connected to the data-acquisition computer included the MBD and a hardcopy device for the graphics terminal.

The standard program used for data manipulation on either computer was a customized installation of the MULTI [88] data analysis system running in an RSX-11M [89] multi-user operating system environment. On the data-acquisition computer, MULTI was responsible for initializing the AST-level routine used for tape handling, for overseeing the operation of the MBD, for construction of real-time histograms, and for the interpretation of keyboard commands to the data acquisition system. On the offline computer, MULTI read back data tapes and constructed histograms according to a user-defined analysis protocol.

The data-acquisition MULTI system was also responsible for issuing requests for the MBD to flush the Beam-Off histograms to the data buffer. Once these histograms were received, MULTI called a user-written program BMOFIT which performed least-squares fits to each of the six Beam-Off histograms and printed the fit results to a dedicated printer port and to a spool file.

Chapter III

DATA ANALYSIS

III.1 Data Sets

Data for Experiment 723 were collected over the course of several running periods from 1982 to 1984. In addition, a background study was conducted in the spring of 1985. A summary of these runs is given in Table X. In so far as was possible, the experimental arrangement was the same for all data runs except for changes in the hardware event trigger as discussed in Section II.4. The background study used a simplified experimental arrangement which excluded the pion spectrometers and the temperature controls.

The kaon beam delivered by the AGS during the 1983 running period was found to have a strong time microstructure, resulting in a severe degradation in performance of both the pion spectrometers and the X-ray spectroscopy system. All data collected in 1983 were subsequently found to be of very poor quality and were discarded.

TABLE X
Data Collection Periods

<u>Run</u>	<u>Date</u>	<u>Tapes</u>	<u>Target</u>	<u>Comments</u>
1	3/16/82 to 4/6/82	1 to 91	Pb	Initial Setup
2A 2B	4/15/82 to 4/30/82	92 to 182 183 to 234	Pb	Good Pb Data
3	5/10/82 to 5/17/82	235 to 313	W	'Old' W Data
4	4/11/83 to 4/19/83	1001 to 1022	W	Poor Beam Quality
5	4/21/83 to 5/3/83	1025 to 1047	U	Poor Beam Quality
6	5/20/84 to 5/30/84	2001 to 2022	W	'New' W Data
7	5/31/84 to 6/17/84	2023 to 2048	U	Poor Calibration
B	5/4/85	No tapes 13 Disk files	W	Stopping Pions (background study)

III.2 Playback

Data tapes were played back on the two PDP 11-34 computer systems using the MULTI data acquisition software package in playback mode. The TAGGED events (those KS- γ events followed by a delayed e^+ signal - see Section II.2.3) and Beam-Off events were sorted from the data tapes and recorded separately on pared-down tapes to facilitate the TAGGED playback. Photon energies recorded in TAGGED events were histogrammed into spectra TAG.A, TAG.B and TAG.C, depending upon which detector observed the X ray. The full energy range of 77 to 750 keV was covered in the TAGGED spectra.

The X-ray energies of those KS- γ events not followed by a delayed e^+ signal were histogrammed in spectra denoted RAW.A, RAW.B and RAW.C, each of which covered the full energy range of 77 to 750 keV.

The photon energies recorded subsequent to a Beam-On event (see section II.4) were used to form histograms which covered only narrow energy regions bracketing the calibration lines. The names of these histograms depended on the particular line or set of lines covered. (Example: ONCO.A covered the 122 keV line of ^{57}Co recorded by detector A.) As a group, these histograms are referred to as the CALON spectra.

All three types of spectra (CALON, RAW and TAGGED) were subjected to a software two-point stabilization procedure on playback. Whenever a Beam-Off software event (consisting of the six Beam-Off histograms - see Section II.4) was encountered in the playback event stream, the processing of events by MULTI was temporarily suspended while a set of

user programs (FITTER and BMOSHF) performed the following sequence of steps:

- 1) Fit each of the six Beam-Off histograms by least-squares to a Gaussian-plus-linear functional form.
- 2) Use the resulting centroids and the known energies of the calibration lines to find the offset and gain, averaged over the data recorded since the last Beam-Off event, of each of the three X-ray detector systems.
- 3) Open a sumfile. For each histogram stored in this file
 - 3a) read in the histogram from the sumfile.
 - 3b) find a matching histogram name in MULTI's playback area.
 - 3c) using the gain and offset of the playback histogram (as determined in step 1) and that of the sumfile histogram (as determined by the histogram header), gainshift the playback histogram to match the sumfile histogram and add the two.
 - 3d) re-write the incremented sumfile histogram to the sumfile.
 - 3e) clear the playback histogram in MULTI's playback area.
- 4) When finished with all histograms, close the sumfile and re-activate MULTI for further playback.

The offset and gain of the histograms in the sumfile were chosen so as to locate the centroid of the 122 keV line of ^{57}Co in channel 500 and that of the 662 keV line of ^{137}Cs in channel 6500.

During playback of the 1982 data, sumfiles were generated for each set of approximately ten data tapes. As a test of the software stabilization procedure, the centroids of the Beam-Off calibration γ -ray lines (122 keV line of ^{57}Co and 662 keV line of ^{137}Cs) were fitted in the CALON spectra of each ten-tape group. Several of these tape sets were found to have CALON centroids inconsistent with the majority of the data. These same subsets of the CALON data exhibited a signal-to-noise ratio at least an order of magnitude greater than that of the majority of the data. This suggests that there may have

been a problem with the Beam-n gate (shown in Figure 15) which could have allowed photons having no particular time correlation with the arrival of beam particles to trigger Beam-On calibration events. The data sets exhibiting abnormally large signal-to-noise ratios in the CALON spectra were thus considered to be unreliable and were excluded from the analysis. The remaining datasets were summed to form master sum files as shown in Table XI.

Of the data collected in 1984, those on tapes 2001 through 2007 were found to have problems stemming from a maladjustment of the preamplifiers of the X-ray spectroscopy system and so were discarded. Tapes 2008 through 2022 were played back with gainshifting and summed into master files RAWO.SUM and TAGWO.SUM as shown in Table XI.

The uranium data (tapes 2023 through 2048) were discarded because of a combination of the poor quality of the calibration data and the difficulties of calculating effects on the energy eigenstates due to dynamic quadrupole mixing.

TABLE XI
Summed Data Files

<u>Filename</u>	<u>Contents</u>	<u>Tapes</u>
RPB2A0.SUM TPB2A0.SUM	RAW and CALON spectra TAGGED spectra	92-182 excluding Det C from 102-112
RPB2B0.SUM TPB2B0.SUM	RAW and CALON spectra TAGGED spectra	183-203 and 224-234
RWO.SUM TWO.SUM	RAW and CALON spectra TAGGED spectra	235-313
RAWO TAGO	RAW and CALON spectra TAGGED spectra	2008-2022

Figures 17,18,19 and 20 show the principal data spectra collected during the course of Experiment 723. The improvement to the signal-to-noise ratios of the Σ^- X-ray lines can be seen in Figure 21, which shows the (12 \rightarrow 11) transition of Σ^- -Pb and the (9 \rightarrow 8) transition of Σ^- -Pb as recorded in both the RAW and the TAGGED spectra.

III.3 Fitting Algorithm

III.3.1 Data Fits

Fits of the data to various functional forms were made by the method of maximum likelihood [90], usually referred to as the method of least-squares for historical reasons. Histograms which contained no channels having fewer than 30 counts were fitted under the assumption that the number of counts in a given channel was described by a Gaussian parent distribution. If a dataset y_j is assumed to derive from a functional form $y_j = f(x_j; a_i)$, then it is easily shown, for Gaussian statistics, that the most likely values of the parameters a_i are those for which the χ^2

$$\text{III.3-1) } \chi^2 = \sum_{j=1}^n \frac{[y_j - f(x_j; a_i)]^2}{\sigma_{y_j}^2}$$

is minimized. If the y_j in equation III.3-1 are the numbers of directly observed events in a counting experiment, then the assumption of Gaussian statistics provides the connection $\sigma_{y_j}^2 = y_j$, and the χ^2 becomes

$$\text{III.3-2) } \chi^2 = \sum_{j=1}^n \frac{[y_j - f(x_j; a_i)]^2}{y_j}$$

Frequently, as in the case of Experiment 723, the y_j represent the output of some pre-processing algorithm (gainshifting, smoothing, etc.) which takes the form

$$\text{III.3.3) } y_j = \sum_k b_{jk} d_k$$

where the d_k represent the observed number of events of class k and the b_{jk} are some constant coefficients characteristic of the algorithm. In this case, $\sigma_{d_k}^2 = d_k$ and

$$\text{III.3-4) } \sigma_{y_j}^2 = \sum_k b_{jk}^2 \sigma_{d_k}^2 = \sum_k b_{jk}^2 d_k$$

The gainshifting algorithm employed during playback of the data of Experiment 723 provided for each channel of the output histograms the sums III.3-3 and III.3-4.

An iterative approximation method was used to determine the values of the parameters a_i for which the χ^2 was minimized. The function $f(x_j; a_i)$ in equation III.3-1 was replaced by its linear expansion about some initial point a_i^0 in the parameter space. Demanding that the derivatives $\partial \chi^2 / \partial a_i$ all vanish results then in a system of linear equations for the parameters a_i . This system of equations may be solved by standard matrix methods to obtain an approximation for the values of the parameters a_i for which the χ^2 is minimized. Repeated applications of this procedure usually converge rapidly.

The assumption of Gaussian statistics is the high-statistics ($n > 30$) limit of the Poisson distribution, which is more generally regarded as the proper description of a counting experiment. Following a method devised by Awaka [91], it is found that the maximum-likelihood values for the parameters which describe a

gainshifted dataset having some or all of its channel values less than 30 are the values for which the parameter

$$\text{III.3-5) } G = \sum_{j=1}^n [y_j \ln(f(x_j; a_i)) - f(x_j; a_i)] / \eta_j$$

is maximized. Here η_j is the averaged value of b_{jk} for the j 'th channel of the gainshifted dataset.

$$\text{III.3-6) } \eta_j = \frac{\sum_k b_{jk} d_k}{\sum_k b_{jk} d_k}$$

The changes in dispersion effected by the gainshifting algorithm used in the playback of the data from Experiment 723 were less than 0.2% in magnitude. In this case, η_j is a slowly varying function of j , and so can easily be approximated by taking the ratio σ_j^2/y_j and smoothing it over a few (usually five) channels to minimize the effects of statistical fluctuations.

The parameter G may be maximized by a method similar to that used to minimize the χ^2 . Substituting a linear expansion of the function $f(x_j; a_i)$ into equation III.3-5 and demanding that the partial derivatives vanish results in a system of linear equations for the parameters a_i which may be solved by standard matrix methods. Repeated applications of this procedure converge rapidly to the values of the parameters for which G , and thus the likelihood, is maximized. Any datasets which contained one or more channels having fewer than 30 counts were fitted by this method. In addition, several high-statistics datasets were fitted using both this method and the more usual method of χ^2 minimization. No significant difference was found

between the results, although considerably more computation time was required for the Poisson-statistics fits.

III.3.2 Parameter Fits

It was frequently necessary in this analysis to fit a set of statistically-determined estimates of one variable to some generalized function of another variable. The generalized function chosen for this analysis was a sum of Legendre polynomials. Since Legendre polynomials are defined only over the region $[-1 \rightarrow +1]$, the values of the independent variable were limited to a finite region which was mapped onto the region $[-1 \rightarrow +1]$ via a linear transformation.

Unlike the fits of Section III.3.1, the datasets to be fitted to polynomials frequently had uncertainties in the values of both the dependent and the independent variables. The uncertainty in the independent variable at each point was multiplied by the slope of the fitted function (or the current best estimate thereof) at that point in order to convert to an equivalent uncertainty in the dependent variable. This equivalent uncertainty was squared and added to the square of the uncertainty in the dependent variable. The result was used as the weighting factor $\sigma_{y_j}^2$ in equation III.3-1, and the resulting χ^2 was then minimized as in Section III.3.1. It was assumed that the values y_j in equation III.3-1 obeyed Gaussian statistics for all parameter fits.

When the polynomial function which had been fitted to a particular dataset was evaluated for some arbitrary value a of the independent variable a_i , the uncertainty assigned to the value of the function was calculated by the relationship

$$\text{III.3-7) } \sigma_{y_i}^2 = \sum_{\substack{\text{all} \\ \text{elements}}} (P) (\epsilon) (P) ; \text{ where } (P) = \begin{Bmatrix} P_0 & 0 & 0 & \dots \\ 0 & P_1 & 0 & \dots \\ 0 & 0 & P_2 & \dots \\ \cdot & \cdot & \cdot & \dots \end{Bmatrix}$$

is a diagonal matrix constructed from the values of the Legendre polynomials at $a_i = a$ and (ϵ) is the error matrix [90].

III.4 Non-Gaussian Detector Response Functions

As discussed in section II.3, optimization of the energy resolution of the X-ray spectroscopy system was of paramount importance to this experiment. During initial testing and setup of the detector array, great care was taken to insure that the best possible energy resolution was obtained subject to the design constraints of the experimental arrangement. Such an optimization regimen required that resolutions obtained with different detector configurations be compared for small differences.

In order to measure small effects on the resolution, monoenergetic γ rays (usually from the 303 keV line of ^{133}Ba) were observed and the digitized photon energies were histogrammed. The resulting intensity-vs-energy spectra were then fitted by the method of least-squares to a functional form consisting of a Gaussian peak on a linear background. The full-width at half-maximum (FWHM) of the Gaussian was taken as a definition of the energy resolution. The statistical uncertainty in this parameter decreased approximately as the inverse square root of the number of monoenergetic photons observed. A typical dataset gathered for purposes of resolution testing contained on the order of 10^5 events in the peak, allowing the FWHM (typically 930 to 1050 eV) to be measured to within approximately one eV.

There was at first some difficulty with a lack of reproducibility of the FWHM from dataset to dataset where the data were collected under identical conditions. Further investigation led to the

discovery of several characteristics of these relatively high-statistics ($i.e.$, large number of observed photons) datasets which affected the resolution-measurement procedure. The fitted value of the FWHM was found to be rather sensitive (10 to 25 eV) to the energy region included in the fit. For this reason, resolution-determination fits which were to be compared were made over the same energy region of approximately 7 keV range centered about the centroid of the peak. The fitted value of the FWHM was also somewhat sensitive to the number of counts in the peak, so that only datasets containing a comparable number of statistics could be compared. The normalized χ^2 parameters of the least-squares fits to these datasets were usually rather poor (2 to 12 χ^2/ν), indicating that the response of the X-ray spectroscopy system to a monoenergetic γ -ray line was non-Gaussian in form.

Overlaid plots of the data and the Gaussian function which was fitted to the data (See Figure 22) indicated that the low-energy wing of the detector response function should decrease less rapidly than does a Gaussian function. Previous authors have attempted to accommodate such a non-Gaussian response function by matching an exponential tail to the Gaussian [92] or by adding a second Gaussian, having a width parameter several times that of the main peak, to the background term [93]. Neither of these methods was found to account satisfactorily for the non-Gaussian detector response in the high-statistics datasets collected during detector optimization. The double-Gaussian form did result in an improvement in the normalized χ^2 parameter simply by virtue of admitting a non-symmetric component to the functional form. However, the low-energy tails of the peaks in

these datasets seemed to be more nearly exponential in nature than could be obtained with a double-Gaussian form, which suffered the additional disadvantage of requiring three more parameters than did a simple Gaussian form. The matched-exponential form gave improvements to the normalized χ^2 parameter beyond those due to the use of a double-Gaussian form. While only one more parameter was required for this form than for the simple Gaussian form, the fitted value of the additional parameter was found to be strongly dependent on the number of photons observed, on the energy region included in the fit, and on statistical fluctuations from dataset to dataset.

Additional clues to the form of the non-Gaussian detector response function were found subsequent to the 1982 run when a failure of the liquid nitrogen dewar caused the temperature of the radiation-damaged detector crystals to rise somewhat above 77K. Such a partial warming allows the crystal lattice in the neighborhood of atomic displacement sites to deform, thus greatly increasing the effectiveness of these damage sites in temporarily trapping charge carriers. The effect on the detector response was a severe loss of resolution, with obvious tails several keV in extent appearing on the low-energy side of the γ -ray peaks. Fits to datasets which were collected under these conditions and which were restricted to essentially the upper half of the peaks were consistent with a Gaussian of FWHM of about one keV. Fits to the same datasets, but restricted to essentially the lower third of the peaks, showed a form which was very nearly exponential in nature. Datasets were collected for each detector in this radiation-damaged state over a wide range of

operating biases. The lengths of the exponential tails were found to decrease with increasing bias voltages.

From these observations, a model of the detector response was formulated. At different stages of the response process, the probability distributions involved will have as independent variables the initial photon energy, the photon energy deposited within the detector crystal, the charge generated by this energy deposition, the charge actually collected by the signal-processing system, the voltage output by the signal processing system, and finally the channel number output of the ADC. The relationship among these variables is very nearly linear. Assuming exact linearity over local regions (for the derivation of the response model only!), one may relate any of the variables to the ADC channel number by a linear transformation which amounts essentially to a choice of scale. For calculational and notational convenience, all variables are expressed in the same units, assumed to be ADC channels, in the discussion that follows.

III.4.1 Charge Production and Collection

The probability distribution $C(Q;E_p)$ for the amount of charge Q produced by the deposition of an energy E_p within the detector crystal was assumed to have a Gaussian form as governed by the charge-production statistics [81].

$$\text{III.4-1) } C(Q;E_p, \sigma) = \frac{1}{\sigma\sqrt{2\pi}} \exp \left[-\frac{(Q-E_p)^2}{2\sigma^2} \right]$$

This distribution was then convoluted with a charge-collection

probability distribution $V(Q_c; Q)$ which represented the probability (averaged over the active volume of the detector) that a charge Q produced within the active volume would result in a charge Q_c collected at the input of the charge-sensitive preamplifier within the shaping time of the pulse-processing system. Since no more charge can be collected than was produced, $V(Q_c; Q)$ is identically zero for Q_c greater than Q .

In a damage-free detector crystal, where charge trapping is at a minimum, there is only a very small probability that large amounts of charge will be delayed or lost, so that $V(Q_c; Q)$ decreases rapidly as Q_c decreases below Q . In the rather unrealistic limit of no trapping, $V(Q_c; Q)$ becomes a Dirac-delta function in the variable $\Delta Q = Q_c - Q$ and the convolution with the Gaussian charge-production distribution yields the Gaussian form which is usually assumed as the detector response function.

In a heavily radiation-damaged detector crystal, where considerable portions of the produced charge may not be collected, $V(Q_c; Q)$ may be much wider than the charge-production distribution $C(Q; E_D, \sigma)$. The convolution then takes on the dominant features of $V(Q_c; Q)$, so that the result is rather insensitive to the structure of $C(Q; E_D, \sigma)$.

The fits to the datasets collected following the partial warmup of the detector crystals led to the trial form

$$\text{III.4-2) } V(Q_c; Q, \lambda) = |1/\lambda| \exp((Q_c - Q)/\lambda) \Theta(\lambda(Q - Q_c))$$

where the step function $\Theta(\lambda(Q - Q_c))$ is used to limit $V(Q_c; Q, \lambda)$ to the domains $(Q_c < Q)$ for $\lambda > 0$ and $(Q_c > Q)$ for $\lambda < 0$. The resulting convolution of $V(Q_c; Q, \lambda)$ and $C(Q; E_p, \sigma)$ yields the detector response function

$$\text{III.4-3) } R_1(Q_c; E_p, \sigma, \lambda) = D(Q_c; E_p, \sigma, \lambda)$$

$$\text{where } D(Q_c; E_p, \sigma, \lambda) = \text{Sign}(y) \exp \left[y + \frac{y}{2x} \right] \text{erfg} \left[\text{Sign}(y) \left(\frac{y}{x} + z \right) \right]$$

$$\text{erfg}(z) = \frac{1}{\sqrt{2\pi}} \int_x^{\infty} \exp \left[\frac{-x^2}{2} \right] dx \quad ; \quad \text{Sign}(x) = x/|x|$$

$$\text{and } y = (Q_c - E_p)/\lambda \quad ; \quad z = (Q_c - E_p)/\sigma$$

This unit-area detector response distribution has, for $\lambda > 0$, a tail of characteristic exponential length λ on the low-energy side of the peak. As λ decreases towards zero the distribution approaches a Gaussian form. This definition may easily be extended to negative values of λ , resulting in a tail structure on the high-energy side of the peak. Plots of representative functions V , C and R_1 are shown in Figure 23-a.

Least-squares fits of the functional form R_1 to high-statistics datasets collected during detector optimization showed a dramatic improvement in the values of the normalized χ^2 over those obtained from fits using any of the previously discussed functional forms. The fitted value of the characteristic length λ was found to be quite insensitive to the energy region and to statistical fluctuations among

different datasets collected under similar conditions. With this functional form, reasonable fits could be obtained to almost all of the datasets collected subsequent to the partial warmup. These radiation-damaged datasets were also fitted to a linear combination of $D(Q_c; E_p, \sigma, \lambda)$ and a Gaussian $G(Q_c; E_p, \sigma)$, with the results that the Gaussian term was nearly always found to be superfluous.

The numerical evaluation of $D(Q_c; E_p, \sigma, \lambda)$ and its derivatives, as required for the application of a least-squares fit algorithm, is somewhat complicated by the $\text{erfg}(z)$ terms involved. An algorithm was developed which calculated $\text{erfg}(z)$ to an accuracy of 12 or more digits over most of its significant range. Depending on the value of the argument z , this algorithm employed either a power series expansion, an expansion in continued fractions, or interpolation between tabulated values via a direct numerical integration of the appropriate Gaussian function. The technique was chosen which would provide the desired accuracy with the least amount of calculation. The resulting algorithm was sufficiently efficient to make least-squares fits to functional forms based on $D(Q_c; E_p, \sigma, \lambda)$ a realistic option in the analysis.

III.4.2 Small-Angle Compton Scattering

With functional forms based on $D(Q_c; E_p, \sigma, \lambda)$ to fit the datasets collected for resolution testing and the CALON data from the 1982 run, several further deviations of the data from the expected form were observed. The background underneath some of the lower-energy peaks such as the 122 keV line of ^{57}Co was found to have a higher value on

the low-energy side of the peak than on the high-energy side. There was rarely any significant difference between the slopes of the backgrounds on the two sides. Datasets collected specifically to study this effect showed that this step-function effect in the background could be increased dramatically by the addition of a thin sheet of aluminum between the photon source and the X-ray detector. This effect was assumed to be due to small-angle Compton scattering of the photons in the material between the source and the detector, resulting in the loss of only small amounts of the photon energy. The Klein-Nishina formula [94] for the angular dependence of the Compton scattering cross section was used to generate a probability distribution for the final energy E_D of Compton-scattered photons originating from a monoenergetic source of energy E_γ . This distribution was found to be nearly independent of energy for small energy losses, and could be closely approximated for energies within a few percent of the initial photon energy E_γ by a step function $P(E_D - E_\gamma) = P \theta(E_\gamma - E_D)$. The energy distribution of photons arriving at the detector crystal from a monoenergetic source thus has the form

$$\text{III.4-4) } I(E_D; E_\gamma, \eta) = \delta(E_D - E_\gamma) + \eta \theta(E_\gamma - E_D)$$

where η may be interpreted as the observed intensity per unit energy per unscattered photon of Compton-scattered photons.

The Gaussian form of the charge production distribution $C(Q; E_D, \sigma)$ is based on the assumption that photons producing the charge all have the same energy. The charge-production distribution resulting from the conversion of photons obeying an intensity

distribution $I(E_p; E_\gamma, \eta)$ is a convolution of this intensity distribution with the monoenergetic production distribution $C(Q; E_p, \sigma)$ so that the detector response function becomes

$$\text{III.4-5) } R_2(Q_c; E_p, \sigma, \lambda, \eta) = V(Q_c; Q, \lambda) * C(Q; E_p, \sigma) * I(E_p; E_\gamma, \eta)$$

Plots of representative functions I and R_2 are shown in Figure 23-b.

III.4.3 Pulse Pileup

Another deviation of the data from the expected form was a small amplitude tail of one or two keV width which appeared on the high-energy side of the peaks in the CALON datasets and, to a lesser extent, in those resolution-test datasets which were collected at high rates. These high-side tails were not observed in datasets collected under low rate conditions, and were assumed to be caused by pulse pileup.

Pulse pileup occurs when the peak of a pulse exiting the shaping amplifier (see Section II.3.2) is insufficiently separated in time from preceding or succeeding peaks to prevent interference. Each LBL amplifier system contained a fast discriminator (200 nsec time resolution) which had its threshold set just above the noise level. A logic circuit in the amplifier monitored the output of this discriminator and rejected pulses which showed an insufficient time separation.

There is an inverse relationship between the time and energy resolutions of any amplifier which processes the output of a solid-state detector crystal. Thus, any discriminator which has a time resolution considerably shorter than that of the shaping amplifier will consequently have an energy resolution which is considerably poorer than that of the shaping amplifier. The discriminator threshold must be set at least one width of its energy resolution above the noise level in order to avoid false triggers, and pulses which fall below this threshold (or which are separated from the pulse of interest by less than the time resolution of the discriminator) are not detected.

The probability that a pulse which falls below this fast discriminator threshold will occur within the time range that a pulse of interest is susceptible to interference increases with increasing rate of low-energy photons. Thus, peaks in high-rate datasets, and especially those collected under beam conditions during which bremsstrahlung and Compton scattering produce many soft X rays, can be expected to have high-side tails. The energies of these tails range above the centroid by up to one or two times the energy resolution of the fast discriminator and their amplitudes increase with rate. The forms and amplitudes of these tails should be independent of the energy of the X ray of interest.

Pulse pileup may be incorporated into the model of detector response by the introduction of a pileup probability distribution $P(A;Q_C)$ which represents the probability that a pulse having amplitude

Q_c in the absence of interfering pulses will be altered in the presence of pulse pileup such that its effective amplitude is A . The LBL amplifiers used for Experiment 723 employed unipolar (Gaussian) pulse shapers so that all such contributions from pulse pileup had the effect of increasing the apparent peak energy. $P(A;Q_c)$ is thus zero for $A < Q_c$ and decreases rapidly to zero for $A > Q_c$. Since most pulses are not subject to pileup, most of the integrated area of $P(A;Q_c)$ will be concentrated in a Dirac-delta function term $\delta(A-Q_c)$. For this analysis, a form

$$\text{III.4-6) } P(A;Q_c, q, \gamma) = \delta(A-Q_c) + q[\exp((A-Q_c)/\gamma) \Theta(\gamma(Q_c-A))]/|\gamma|$$

is assumed, where q is the portion of events subject to pileup and γ is the characteristic length of the exponentially-shaped pileup tail. This form is computationally convenient and was found to be sufficient to describe the observed highside tails. The detector response function $R_2(Q_c; E_\gamma, \sigma, \lambda, \pi)$ previously derived may be convoluted with $P(A;Q_c, q, \gamma)$ to give the expected response function with pileup included.

$$\text{III.4-7) } R_3(A; E_\gamma, \sigma, \lambda, \pi, q, \gamma) = P(A;Q_c, q, \gamma) * R_2(Q_c; E_\gamma, \sigma, \lambda, \pi)$$

Plots of representative functions P and R_3 are shown in Figure 23-c.

III.4.4 Amplifier and ADC Noise

A detailed study both of an experimental and a Monte-Carlo simulation nature showed that the ADC response over localized regions of input voltage had the effect of smearing the voltage by a Gaussian

of FWHM of about 0.5 channels. The order of the convolutions in equation III.4-7 may be commuted. Rather than convoluting R_3 by the ADC response function, the ADC response function may be first convoluted with the Gaussian charge-production distribution $C(Q;E_D, \sigma)$. This results in a slight increase of the effective value of σ . In an identical manner, the noise in the amplifier system was assumed to have a Gaussian form (confirmed by pulser tests), and so may be included in the effective value of σ . Since only the effective value of σ is actually observable in the X-ray data, the amplifier noise and ADC response functions are not included explicitly in this model of the detector response.

III.4.5 Functional Form

A considerable mathematical simplification results if the order of the convolutions in equation III.4-7 are commuted so that $R_3 = P * V * C * I$ becomes $R_3 = C * (P * V * I)$. This simplification is due to the fact that a convolution of two truncated exponentials is a linear combination of those same truncated exponentials. Since the step function Θ is the long-tail limit of a truncated exponential, the final detector response function $R_3(A; E_\gamma, \sigma, \lambda, \tau, q, \gamma)$ may thus be expressed as a linear combination of terms based on the exponential-Gaussian convolution $D(A; E_\gamma, \sigma, \beta)$ in which the allowed values of β are λ , γ , and some rather arbitrary but very large positive number ω , taken for this analysis to be equal to 2×10^5 . The resulting form of the detector response function is:

$$\text{III.4-8) } R_g = a_\lambda D(A; E_g, \sigma, \lambda) + a_\gamma D(A; E_g, \sigma, \gamma) + a_\omega D(A; E_g, \sigma, \omega)$$

$$\text{where } a_\lambda = 1 + \left[\frac{\eta \lambda}{\lambda - \omega} \right] + \left[\frac{q \lambda}{\lambda - \gamma} \right] + \left[\frac{\eta \lambda}{\lambda - \omega} \right] \left[\frac{q \lambda}{\lambda - \gamma} \right]$$

$$a_\gamma = \frac{q \gamma}{(\lambda - \gamma)} \left[\frac{\eta \gamma}{(\omega - \gamma)} - 1 \right]$$

$$a_\omega = \frac{\eta \omega^2}{(\lambda - \omega)} \left[\frac{q \omega}{(\gamma - \omega)} - 1 \right]$$

and

- A = final output variable
- E_g = centroid parameter
- σ = Gaussian width parameter (effective)
- λ = charge trapping parameter (tail length)
- q = pileup tail amplitude
- γ = pileup tail length
- η = Compton shelf amplitude
- ω = 2×10^5 = Compton shelf 'length'

This functional form is normalized to a total area $A = (1 + \eta \omega)(1 + q)$, with a portion $(1 + q)$ due to the main peak with pileup and a portion $\eta \omega(1 + q)$ due to the Compton shelf with pileup. The experimental data were fitted to functional forms $f = (\text{Amplitude}) R_g$. An area of $(\text{Amplitude})(1 + q)$ was attributed to the peak for the purposes of extracting yields from the data.

III.5 Parameterization of the Detector Response Function

The response of the X-ray detector system to monoenergetic photons was not assumed to be a constant from run to run, although it was assumed that there were no significant differences between the responses as recorded in the CALON, RAW, and TAGGED spectra of a given run. The sequence of steps used to extract a parameterization of the detector response as a function of energy was motivated by the observation that the different non-Gaussian parameters affected the functional form in different regions. The Compton-shelf parameter affected almost exclusively the background on the low-energy side of the peak. The charge-trapping parameter λ affected primarily the central part of the data peak and, to a lesser extent, its low-energy wing. The pulse pileup parameters q and γ affected primarily the high-energy wing and, to a much lesser extent, the central part of the data peak. Thus, parameterizations as a function of the centroid channel number N_c were first found for η , then for q and γ , then for λ , and then for the Gaussian width σ . Finally, the centroid channel number N_c was parameterized as a function of energy.

The normalized χ^2 of the polynomial fits used to extract these parameterizations frequently exhibited either abnormally large or abnormally small values. This was found to be due in part to the uneven spacing in energy of the calibration X rays. A commonly observed case was that of a dataset containing a subset of three or more points which were closely spaced in energy, one of which differed significantly in ordinate value from the others. The Legendre polynomials could not accommodate such rapid variations as a function

of the independent variable, and the χ^2 suffered badly as a result. In every case of this type, a polynomial fitted to the dataset with the single troublesome point excluded did not differ significantly from the polynomial fitted to the entire data set. As a precaution, the error bars of all parameterization fits were scaled by $\sqrt{\chi^2/\nu}$ whenever χ^2/ν was greater than one.

Another commonly observed case was that of a dataset containing a subset of three or more points, closely spaced in energy, having ordinate values which differed by considerably less than their statistical uncertainties. This resulted in abnormally small values of χ^2 . In these cases, the uncertainties were representative more of the insensitivity to the parameter values of the data fits from which they were derived rather than of any actual variations from point to point of the parameter values.

III.5.1 Compton-Shelf Parameter

In order to extract a parameterization for η from a given CALON spectrum, the method of least-squares was used to fit all the calibration peaks in that spectrum with the non-Gaussian functional form complete with Compton scattering and pulse pileup. When all the fitted parameters were allowed to vary simultaneously, several of the calibration peaks seemed to cause unstable behavior in the fitting algorithm even when the parameter stepsize was severely restricted in an effort to prevent oscillations. These particular peaks were excluded from the analysis in this first step. For the data of runs 2A and 2B, the values of the Compton-shelf parameter η obtained from

the remaining peaks formed a smooth curve and could be fitted to Legendre polynomials of up to second order in $\log(N_0)$, where N_0 is the centroid parameter of the fits. The results of these fits are shown in Table XII. For the data of runs 3 and 6, the values of the Compton-shelf parameter τ_c did not form a smooth curve when plotted as a function of N_0 . This parameter was thus included as a free variable in all subsequent fits to the CALON data of runs 3 and 6. It was not necessary to include a Compton-shelf term in any of the fits to the RAW and TAGGED data owing to their lower statistics and to the poorer signal-to-noise ratio of these datasets as compared to the CALON datasets.

TABLE XII
Compton-shelf Parameterization

$$\eta = [a_0 P_0(X) + a_1 P_1(X) + a_2 P_2(X)]/\omega$$

where $X = \frac{2[\log(N_c) - \log(3500)]}{[\log(6600) - \log(400)]}$ and $N_c = \text{Channel number}$
 $\omega = 2 \times 10^5$

Data Set	Norm χ^2	a_0	a_1	a_2
<u>RFB2A0, SUM</u>				
Detector A	0.5143	115.7 ± 5.0	-104.8 ± 4.9	23.5 ± 7.1
Detector B	0.0095	99.8 ± 4.8	-120.3 ± 4.6	56.9 ± 6.5
Detector C	0.0463	61.5 ± 3.9	-69.1 ± 4.0	22.3 ± 5.4
<u>RFB2B0, SUM</u>				
Detector A	0.4686	123.1 ± 6.1	-113.2 ± 6.8	-----
Detector B	0.0024	137.5 ± 8.0	-101.5 ± 8.6	-----
Detector C	0.2619	51.3 ± 6.5	-61.9 ± 7.7	37.2 ± 10.2

III.5.2 Pulse Pileup Parameters

Next, all of the calibration data peaks were fitted with values for the Compton-shelf parameter η fixed to the values determined from the parameterization shown in Table XII. All calibration peaks which still exhibited unstable behavior were again excluded, and the remaining fits were then used to obtain a parameterization of the pulse pileup parameters q and γ . These parameters were fitted to Legendre polynomials of up to second order in N_c . The results of

these fits are shown in Tables XIII and XIV.

TABLE XIII
Pulse Pileup Amplitude Parameterization

$$q = [a_0 P_0(X) + a_1 P_1(X) + a_2 P_2(X)]/100$$

where

$$X = \frac{2(N_0 - 3500)}{[6600 - 400]} \quad \text{and} \quad N_0 = \text{Channel number}$$

<u>Data set</u>	<u>Norm χ^2</u>	<u>a0</u>	<u>a1</u>	<u>a2</u>
<u>RPD2A0.SUM</u>				
Detector A	0.8471	4.33 ± 0.08	0.10 ± 0.11	-----
Detector B	0.2972	4.28 ± 0.13	0.15 ± 0.15	-----
Detector C	4.8329	5.09 ± 0.12	-0.42 ± 0.11	-0.68 ± 0.15
<u>RPD2B0.SUM</u>				
Detector A	1.5509	4.73 ± 0.24	0.50 ± 0.29	-----
Detector B	0.1478	4.85 ± 0.24	0.32 ± 0.29	-0.85 ± 0.30
Detector C	0.3482	4.65 ± 0.16	-0.31 ± 0.18	-0.54 ± 0.20
<u>RWD.SUM</u>				
Detector A	0.4549	3.86 ± 0.13	0.19 ± 0.14	-----
Detector B	0.6572	3.98 ± 0.11	0.24 ± 0.11	-----
Detector C	3.8264	4.24 ± 0.11	-0.52 ± 0.11	-----
<u>RAWWO.SUM</u>				
Detector A	0.7380	8.51 ± 1.22	-2.94 ± 1.31	-----
Detector B	0.9880	8.57 ± 0.92	-1.04 ± 1.14	-----
Detector C	0.9987	6.48 ± 1.09	-1.35 ± 1.31	-----

TABLE XIV
Pulse Pileup Length Parameterization

$$Y = a_0 P_0(X) + a_1 P_1(X) + a_2 P_2(X)$$

where

$$X = \frac{2[N_0 - 3500]}{[6600 - 400]} \quad \text{and} \quad N_0 = \text{Channel number}$$

Data set	Norm χ^2	a_0	a_1	a_2
<u>RFB2A0.SUM</u>				
Detector A	0.5537	-16.08 ± 0.52	0.11 ± 0.68	-----
Detector B	1.0502	-11.83 ± 0.50	1.67 ± 0.59	-1.53 ± 0.66
Detector C	4.4192	-11.72 ± 0.31	-3.20 ± 0.39	-----
<u>RFB2B0.SUM</u>				
Detector A	0.8756	-12.96 ± 0.75	3.53 ± 0.98	-----
Detector B	0.9750	-11.31 ± 0.69	-0.72 ± 0.90	-----
Detector C	0.1916	-13.60 ± 0.66	-1.67 ± 0.72	1.60 ± 0.81
<u>RW0.SUM</u>				
Detector A	0.0662	-7.45 ± 2.34	-0.96 ± 0.87	-6.01 ± 2.60
Detector B	0.9470	-8.39 ± 1.49	-2.75 ± 1.18	-7.72 ± 1.68
Detector C	0.2958	-9.62 ± 1.06	-3.92 ± 1.08	-3.52 ± 1.18
<u>RAWW0.SUM</u>				
Detector A	6.0813	-7.17 ± 0.84	-3.42 ± 1.17	-----
Detector B	0.5240	-7.45 ± 0.62	-1.99 ± 0.79	-----
Detector C	0.0009	-6.98 ± 0.80	-1.26 ± 1.00	-----

III.5.3 Charge Trapping Parameter

In the next step, all the calibration peaks were again fitted, this time with both the Compton-shelf and the pulse pileup parameters fixed to values taken from their respective parameterizations. At this point, stable fits were obtained to all the calibration peaks. These fits were used to parameterize the charge-trapping parameter λ .

Several of the calibration peaks collected by detector A exhibited negative values for λ . A set of simulations was carried out in which functional forms having small values of λ of either sign ($|\lambda| < \sigma/4$) were used to generate pseudo-randomized datasets which were then fitted by least-squares to the same form. The maps of $\chi^2 - \chi^2_{\text{min}} - \lambda$ generated by these fits were found to have two minima, one for each sign of the fitted value of λ . It was found that statistical fluctuations could sometimes cause the proper minimum in the χ^2 map to be smoothed out to the extent that the spurious minimum would be selected by the fitting algorithm. In these cases, it was not possible to recover the input value of λ . If the proper minimum was selected by the fitting algorithm, the simulations showed that the fitted value of λ was no more sensitive to statistical fluctuations than was indicated by the appropriate element of the error matrix of the fit. There are strong theoretical grounds for expecting λ to be everywhere positive (see section III.4.1). This was, in fact, the case for all but a few calibration peaks. These exceptional data sets were all collected by detector A, which consistently showed the smallest values of $|\lambda|$. All fits, therefore, which resulted in negative values of λ were excluded as input to the parameterization

of λ .

The values of λ were fitted to Legendre polynomials of up to second order in N_o . The results of these fits are shown in Table XV.

TABLE IV
Charge Trapping Parameterization

$$\lambda = a_0 P_0(X) + a_1 P_1(X) + a_2 P_2(X)$$

where

$$X = \frac{2[N_o - 3500]}{[6600 - 400]} \quad \text{and} \quad N_o = \text{Channel number}$$

Data set	Norm χ^2	a_0	a_1	a_2
<u>RFB2A0.SUM</u>				
Detector A	0.3746	1.346 ± 0.053	0.736 ± 0.076	-----
Detector B	2.6799	2.605 ± 0.021	1.486 ± 0.023	-0.152 ± 0.027
Detector C	2.0270	1.835 ± 0.025	1.075 ± 0.026	0.064 ± 0.032
<u>RFB2B0.SUM</u>				
Detector A	0.1688	1.422 ± 0.084	1.145 ± 0.108	-----
Detector B	1.4228	2.547 ± 0.030	1.425 ± 0.037	-0.111 ± 0.040
Detector C	0.5947	1.960 ± 0.039	1.176 ± 0.036	0.190 ± 0.048
<u>RW0.SUM</u>				
Detector A	0.8313	1.817 ± 0.205	1.073 ± 0.215	-----
Detector B	0.6317	2.449 ± 0.021	1.351 ± 0.022	-----
Detector C	0.9356	2.493 ± 0.024	1.635 ± 0.025	-----
<u>RAW0.SUM</u>				
Detector A	0.2118	1.676 ± 0.097	0.193 ± 0.149	-----
Detector B	3.1984	2.409 ± 0.052	1.007 ± 0.068	-----
Detector C	1.3233	1.463 ± 0.089	0.093 ± 0.142	-----

III.5.4 Gaussian Width Parameter

The Gaussian width parameter σ was parameterized by fitting all the calibration data peaks with all of the non-Gaussian parameters (λ, η, q, ξ) fixed at their parameterized values. The resulting values of σ were fitted to Legendre polynomials of up to second order in N_0 . The results of these fits are shown in Table XVI.

TABLE XVI

Gaussian Width Parameterization

where

$$\sigma = a_0 P_0(X) + a_1 P_1(X) + a_2 P_2(X)$$

$$X = \frac{2\{N_c - 3500\}}{[6600 - 400]} \quad \text{and} \quad N_c = \text{Channel number}$$

Data set	Norm χ^2	a_0	a_1	a_2
<u>RFB2A0.SUM</u>				
Detector A	2.0984	4.709 ± 0.004	1.234 ± 0.005	-0.097 ± 0.004
Detector B	2.1885	4.501 ± 0.004	1.152 ± 0.005	-0.053 ± 0.005
Detector C	10.6142	4.932 ± 0.003	1.361 ± 0.004	-0.111 ± 0.004
<u>RFB2B0.SUM</u>				
Detector A	8.1556	4.719 ± 0.006	1.148 ± 0.008	-0.124 ± 0.008
Detector B	6.1187	4.551 ± 0.007	1.190 ± 0.009	-0.072 ± 0.009
Detector C	2.5424	5.011 ± 0.006	1.371 ± 0.007	-0.162 ± 0.007
<u>RW0.SUM</u>				
Detector A	0.2872	4.779 ± 0.017	1.286 ± 0.005	-0.129 ± 0.019
Detector B	1.0990	4.650 ± 0.020	1.253 ± 0.005	-0.102 ± 0.022
Detector C	3.4599	5.031 ± 0.012	1.412 ± 0.003	-0.108 ± 0.013
<u>RAWW0.SUM</u>				
Detector A	1.5681	4.737 ± 0.010	1.485 ± 0.014	-0.067 ± 0.016
Detector B	8.3343	4.778 ± 0.010	1.335 ± 0.012	-0.059 ± 0.014
Detector C	1.1210	4.779 ± 0.008	1.449 ± 0.011	-0.069 ± 0.012

III.5.5 Energy Calibration

Finally, all the calibration data peaks were fitted with the Gaussian width σ and all non-Gaussian parameters (λ, η, q, γ) fixed at their parameterized values. The resulting values of the centroid parameter N_c were fitted to Legendre polynomials of up to fourth order in energy, providing an energy calibration for each of the CALON histograms. The results of these fits are shown in Table XVII.

TABLE XVII
Energy Parameterization

$$N_c = a_0 P_c(X) + a_1 P_1(X) + a_2 P_2(X) + a_3 P_3(X) + a_4 P_4(X)$$

$$\text{where } X = \frac{2[\text{Energy} - 400 \text{ keV}]}{[700 \text{ keV} - 100 \text{ keV}]}$$

<u>RFB2A0.SUM</u>	<u>Detector A</u>	<u>Detector B</u>	<u>Detector C</u>
Norm χ^2	1.0212	0.6363	1.8724
a0	3594.610 ± 0.011	3595.415 ± 0.013	3594.129 ± 0.012
a1	3336.347 ± 0.019	3337.442 ± 0.021	3337.012 ± 0.020
a2	-0.657 ± 0.023	-0.844 ± 0.025	0.033 ± 0.024
a3	-0.314 ± 0.029	-0.225 ± 0.031	-0.492 ± 0.030
a4	-----	0.900 ± 0.058	0.311 ± 0.052
<u>RFB2B0.SUM</u>	<u>Detector A</u>	<u>Detector B</u>	<u>Detector C</u>
Norm χ^2	0.6330	0.5339	0.0436
a0	3594.709 ± 0.014	3595.277 ± 0.018	3594.195 ± 0.016
a1	3336.843 ± 0.025	3337.385 ± 0.027	3337.132 ± 0.025
a2	-0.753 ± 0.028	-0.683 ± 0.032	0.207 ± 0.029
a3	-0.521 ± 0.041	-0.321 ± 0.045	-0.406 ± 0.041
a4	-----	0.673 ± 0.088	0.627 ± 0.075
<u>RW0.SUM</u>	<u>Detector A</u>	<u>Detector B</u>	<u>Detector C</u>
Norm χ^2	4.3394	0.7723	11.0663
a0	3594.982 ± 0.013	3595.157 ± 0.016	3594.818 ± 0.013
a1	3336.816 ± 0.021	3337.307 ± 0.023	3337.761 ± 0.021
a2	-0.520 ± 0.026	-0.604 ± 0.029	-0.205 ± 0.024
a3	-0.416 ± 0.034	-0.216 ± 0.040	-0.704 ± 0.032
a4	0.099 ± 0.053	0.909 ± 0.061	0.396 ± 0.052
<u>RAWW0.SUM</u>	<u>Detector A</u>	<u>Detector B</u>	<u>Detector C</u>
Norm χ^2	4.8690	1.8924	3.2959
a0	3592.046 ± 0.019	3593.533 ± 0.017	3591.813 ± 0.016
a1	3336.464 ± 0.028	3337.003 ± 0.026	3335.863 ± 0.025
a2	0.247 ± 0.029	-0.806 ± 0.027	-0.302 ± 0.026
a3	-0.437 ± 0.032	-0.076 ± 0.029	-0.519 ± 0.028
a4	1.936 ± 0.130	1.017 ± 0.115	0.456 ± 0.112

III.6 Determination of Detector Relative Efficiency

During the summer following the 1982 running period, calibration datasets were collected in an attempt to measure the relative detection efficiency as a function of photon energy of each of the three X-ray spectroscopy systems. Spectra were collected from a number of γ -ray sources (^{75}Se , ^{133}Ba , ^{154}Eu , ^{112}In) centered 12 cm above the upper face of the vacuum jacket surrounding the detector array. Each source emitted several γ -ray lines covering a range of energies. The intensity of each line from a given source relative to the other lines from the same source was available from the literature [86]. The relative detector efficiencies at the energies of the source lines could thus be determined for each source, with one free normalization parameter for the efficiency set of each source.

The normalization of the ^{133}Ba efficiency set was arbitrarily chosen so that the efficiency at the 356 keV line was unity. The normalizations of the other efficiency sets were allowed to vary as free parameters in a fit of the combined efficiency sets to the form $\ln(\epsilon)$ -polynomial in channel number. The results of these fits are shown in Table XVIII. Figure 24 shows a plot of a representative efficiency curve (that of detector B) and the data points from which it is derived.

TABLE XVIII

Detector Relative Efficiency Parameterization

$$\ln(\epsilon) = a_0 P_0(X) + a_1 P_1(X) + a_2 P_2(X)$$

$$\text{where } X = \frac{2[\text{Energy} - 400 \text{ keV}]}{[600 \text{ keV} - 400 \text{ keV}]}$$

<u>Data set</u>	<u>Norm χ^2</u>	<u>a_0</u>	<u>a_1</u>	<u>a_2</u>
Detector A	1.3958	-0.183 ± 0.014	-1.171 ± 0.028	0.336 ± 0.017
Detector B	1.2584	-0.147 ± 0.013	-1.092 ± 0.026	0.373 ± 0.017
Detector C	2.0171	-0.170 ± 0.013	-1.124 ± 0.025	0.337 ± 0.016

III.7 Determination of Target Transmission

III.7.1 Measurement of Target Transmission

Although several attempts were made over the summer of 1982, no good general method could be found to measure experimentally the average attenuation of X-ray intensities due to photon absorption within the target assembly. The most convincing attempt resulted when a replica of the lead target was positioned above the detector in a re-creation of the experimental geometry. The sources used for the measurement of the detector relative efficiency (see Section III.6) were sandwiched one at a time between two small pieces of lead foil having thicknesses each one-half that of the target sheets. The edges of this source sandwich were crimped closed to simulate a source of X rays originating from within a target sheet.

An energy spectrum was collected for each efficiency-calibration source with the source-foil sandwich positioned at a number of points scattered throughout the interfoil spaces of the replica target. The collection time at each source location was chosen to simulate the distribution of K^- stopping within the target, as determined by a Monte-Carlo calculation. With the proper choice of normalization, the ratio of the relative efficiency measured with the mock target in position to that measured with no intervening material (as in Section III.6) agreed within the errors of the measurement with the transmission curve calculated by a Monte-Carlo computer simulation of the X-ray production and detection process.

Since tungsten is too brittle to be formed into a sandwich source, the analysis of the tungsten data relied on the Monte-Carlo calculation of target transmission. For consistency in the analysis, the experimental measurement of the lead transmission curves described above were regarded as a check on the Monte-Carlo calculation. Only the transmission curves determined by the Monte-Carlo calculation were actually used in the analysis.

III.7.2 Calculation of Target Transmission

The calculation of the target transmission was broken into three separate steps, each of which was carried out by a Monte-Carlo method. Firstly, the distribution of K^- stopping in the target was calculated for incident K^- characteristic of the beam delivered to the C4 experimental station. Secondly, the distribution was calculated of those Σ^- which were produced by the stopping kaons and which subsequently came to rest in one of the target foils. Finally, the distributions of those K^- and Σ^- which stopped in target foils were taken as source distributions for isotropic X-ray emission, and the probability that a given photon would arrive unabsorbed at one of the three X-ray detectors was calculated as a function of energy and then averaged over the source distribution.

The Monte-Carlo method of calculation relies heavily on the generation of a pseudo-random sequence of numbers. An algorithm for a 32-bit congruence generator [95] was tested and found to have no significant non-random behavior over a wide range of initial seed values. This single algorithm was used for all pseudo-randomization procedures carried out within the various Monte-Carlo calculations. In the discussion that follows, the generation by this algorithm of a pseudo-random perturbation to one of the state constants is referred to as a randomization, with the prefix 'pseudo-' implied.

All three steps of the calculation used the same representation of the experimental arrangement wherein the volume of the experimental area was divided into a number of homogeneous rectilinear volume

elements corresponding to the various experimental components. The stopping distributions were calculated with the help of a computer subroutine called GEOM which simulated the passage of energetic charged particles through a homogeneous material medium, and which included randomized treatments of lateral drift, transverse scattering, energy loss and straggling, particle decay, and inelastic nuclear reactions between the particle and the nuclei of the material medium.

A general method of simulating the absorption or decay of a particle was devised which was then customized for those particles recognized by the Monte-Carlo software package which undergo such reactions (π^\pm , μ^\pm , K^\pm , Σ^\pm). This resulted in a set of subroutines, one for each type of particle, which selected at random an outcome from the possible reaction products. The statistical weight of each outcome was determined by the branching ratio of the process involved [77].

All of the processes pertinent to these Monte-Carlo calculations had two-body final states except for the three-body decay of muons. In the case of a two-body final state, the total center-of-mass energy available to the reaction was divided between the reaction products according to the kinematical relationships [77]:

$$\text{III.7-1) } \begin{aligned} E_1 &= (E^2 + m_1^2 - m_2^2) / 2E \\ E_2 &= (E^2 + m_2^2 - m_1^2) / 2E \end{aligned} \quad \text{where } E = E_1 + E_2$$

The momenta thus determined for the reaction products were assigned

opposite directions in a random orientation within the CM frame.

The three-body case of muon decay was treated somewhat differently. In the CM frame, the energy of the decay e^+ or e^- was selected randomly from a distribution representative of the Michel spectrum [96]. The resulting momentum of the e^+ or e^- was assigned a random direction. The remaining two particles, being neutrinos, were undetected in the experiment and so were ignored by the Monte-Carlo software. In both the two-body and the three-body cases, the energy-momentum four-vectors of all pertinent reaction products were transformed back to the laboratory frame and then were used to initialize the appropriate four-momentum variables in the Monte-Carlo software package.

In order to calculate the distributions of K^- and Ξ^- which stopped in the target foils, subroutine GEOM was used to project the path through the experimental arrangement of a randomized distribution of incident K^- representative of the beam delivered by the AGS facility. The locations of those K^- which stopped in a foil of the high-Z target material were tabulated. In addition, the reaction-simulating algorithm was applied ten times at the location of each K^- which stopped within the target volume. For each application which resulted in the simulated production of a Ξ^- , subroutine GEOM was used to project the path of the Ξ^- through the target assembly. The locations of those Ξ^- which stopped in a foil of the high-Z target material were tabulated.

The transmission probability curve for a given stopping distribution was calculated by choosing 40 random directions, distributed isotropically, for each of the locations recorded as part of the distribution. Projections were made along the rays so defined to determine whether or not they would intersect the active volume of one of the three X-ray detector crystals. The types and thicknesses of all material traversed were tabulated for those rays which did intersect a detector crystal.

For each detector, a histogram was defined which had two real-valued bins, one for values and one for the squares of the values. Each bin pair was assigned an energy range determined by the bin index and by the binwidth and offset stored in the histogram header. The transmission probability for each photon path which intersected a detector crystal was calculated at each energy of the grid defined by the histogram for that particular detector. The photon mass-attenuation constants used for this calculation were interpolated from values tabulated at key energies for each material [97]. The resulting transmission probabilities and their squares were summed to the value and squared-value bins of the histogram for the appropriate detector.

This procedure was repeated for all locations recorded in the stopping distribution, and the resulting summed value and squared-value bins were used to calculate the mean and variance of the transmission histograms at each point of their respective energy grids. Representatives of the resulting curves of relative

transmission- y_2 -energy are shown in Figure 25.

During the development and initial testing of the transmission-calculation Monte-Carlo software, it was found that the shapes of the transmission curves (but not their overall normalizations) were very insensitive to small (one or two cm) changes in the locations of the detector crystals relative to the target assembly. Other variables which were found to have little or no effect on the shapes were the assumed spot size, divergence, horizontal steering, and central momentum of the kaon beam. Only the vertical beam steering showed a significant effect on the shapes of the transmission curves.

III.8 Energy Calculations

The initial values assumed in this analysis for the masses of the K^- and Σ^- were [77]

$$m_{K^-} = 493.667 \pm 0.015 \text{ MeV}$$

$$m_{\Sigma^-} = 1197.34 \pm 0.05 \text{ MeV}$$

A detailed analysis for the purpose of extracting the masses [12] has shown that the data of Experiment 723 are consistent with these values.

III.8.1 Calculation of Potentials

Calculations of the energy eigenvalues were made via numerical integration of either the Dirac or the Klein-Gordon equation (see Section I.1). This required the calculation of a number of hadron-nucleus potential functions on a grid (i.e., at each of a series of equally spaced radii) about the nucleus. The grid for each hadron-nucleus system was chosen with a sufficiently small grid step size and a sufficiently large maximum radius to accommodate all of the states of that particular hadron-nucleus system for which energy eigenvalues were to be calculated. The potentials thus needed to be calculated only once, and were then stored in disk files for later use. The potential functions calculated in this manner for each of the systems K^- -Pb, Σ^- -Pb, K^- -W, and Σ^- -W are listed in Table XIX.

 TABLE XIX
 Potentials Calculated for Each Hadron-Nucleus System

<u>Entry</u>	<u>Potential</u>
1)	Point-nucleus electrostatic (Coulomb) potential
2)	Finite-nucleus electrostatic potential
3)	Finite-nucleus $\alpha(Z\alpha)$ vacuum polarization potential
4)	Finite-nucleus $\alpha^2(Z\alpha)$ vacuum polarization potential
5)	Finite-nucleus $\alpha(Z\alpha)^{3,5,7}$ vacuum polarization potential
6)	Electron screening potential
7)	Finite-nucleus total electrodynamic potential (Sum of entries 2 \rightarrow 7)
8)	Perturbation potential (Entry 1 minus Entry 7)

The (time-averaged) nuclear charge distribution was assumed to follow the Fermi distribution, with radius and skin thickness parameter values for each isotope taken from Reference [2]. The values of the isotopic masses were taken from Reference [98]. Weighted means of these masses and charge distribution parameters were calculated for each hadron-nucleus system, in which the natural abundance [98] of each isotope was taken as the weighting factor. It was these weighted mean values, listed in Table XX, which were used in the eigenvalue calculations.

TABLE XI
Weighted Means of Nuclear Parameters

	<u>Tungsten</u>	<u>Lead</u>
Mass Number (A)	183.8904	207.2426
Atomic Mass	183.8415	207.2185
Fermi Radius (c)	6.501 fm	6.6194 fm
Skin Thickness (x)	0.543 fm	0.5473 fm

The algorithm for the finite-nucleus Coulomb potential first calculated the nuclear distribution, numerically evaluated its volume integral, and re-normalized the distribution to insure a total nuclear charge equal to Z_0 . Next, the integrated charge within a sphere of radius r centered at the origin (center of the nucleus) was evaluated for each value of r on the grid which fell within the nuclear charge distribution. Gauss' law was applied at these interior grid points to derive at each one the radial derivative of the electrostatic potential. The potential itself was evaluated at each of the interior grid points by a numerical integration of this radial derivative from a point outside of the nucleus. Coulomb's law was used to evaluate the potential and its radial derivative at all grid points exterior to the nuclear charge distribution.

Values for the electron screening potential were interpolated from the tabulated values of Vogel [1]. The constant part of this potential was chosen so that the potential vanished at the origin (See Section I.2.1).

Two different methods were used to calculate the vacuum polarization potentials, depending on the radius at which they were to be evaluated. At radii less than four times the Fermi (half-maximum) radius of the nuclear charge distribution, the $\alpha(Z\alpha)$ and $\alpha^2(Z\alpha)$ vacuum polarization potentials of a finite nucleus were calculated by convoluting numerically those due to a point source over the nuclear charge distribution. This was accomplished with the aid of the parameterizations of the indefinite integrals of the point-source potentials due to Fullerton and Rinker [33] (see Section I.2.2). At radii greater than four times the Fermi radius, this convolution was approximated by an expansion in terms of the first few radial moments of the charge distribution. The values of the point-source potential and its radial derivatives required for this expansion were also calculated by parameterizations due to Fullerton and Rinker [33]. The zeroth, second and fourth radial moments were retained in the expansion of the $\alpha(Z\alpha)$ potential. Because of the spherical symmetry of the nucleus, odd moments vanish. Only the zeroth (normalization) moment was retained for the higher-order potentials.

As discussed in section I.2.2, the finite-nucleus $\alpha(Z\alpha)^{3,5,7}$ potentials at moderate radii can differ significantly from the convolution of the point-source potentials over the nuclear charge

distribution [34]. Appendix A describes in some detail a parameterization derived in the course of this analysis which, when convoluted over the nuclear charge distribution, gives an approximation to the finite-nucleus $\propto(Z\alpha)^{3,5,7}$ potentials which is good for most of the radii accessible to hadrons orbiting nuclei with $Z < 90$. All calculations in this analysis which required the finite-nucleus $\propto(Z\alpha)^{3,5,7}$ vacuum polarization potentials as inputs were carried out with the aid of this parameterization.

III.8.2 Integration of the Wave Equation

For a given set of quantum numbers and a given assumed state energy, the wave functions were obtained by numerical integration using a fourth-order Runge-Kutta algorithm [24] which was customized for a system of two simultaneous first-order partial differential equations. The second-order Klein-Gordon equation was converted to a system of two first-order equations so that the same integration algorithm could be used for either equation. The algorithm was initialized as discussed in section 1.1 at the grid point nearest to, but not coincident with, the origin and at the largest radius which occurred in the particular subset of the grid chosen for the eigenstate under consideration. The values of the spherical Bessel functions needed for this initialization were calculated by a combination of power series expansions, continued fraction expansions, and recursion relations [24]. The integration of the wave function was performed outwards from the origin and inwards from the periphery to some mid-point radius, where the two solution halves were matched.

As discussed in sections I.1.2 and I.1.3, the solution pairs of the Dirac and Klein-Gordon equations for a spherically symmetrical system may be expressed at very large and at very small radii in such a way that one solution of each solution pair is excluded by the bound-state requirement of a localized, finitely normalized wave function. The excluded solutions are a rapidly decreasing function of radius near the origin and a rapidly increasing function of radius at very large radii. The desired solutions show a rapid increase with increasing radius near the origin and a rapid decrease with increasing radius at very large radii. The technique of integrating from the extremities of radius to some mid-point thus aids in reducing the effects of truncation and discretization errors on the numerical integration algorithm [20]. Any errors introduced near the extremities (where the radial behavior of the wave function is the most radical) are of necessity of the form of a slight admixture of the excluded solution. The relative amount of this admixture which is propagated away from the extremities towards the matching point is very small, since in both cases the desired component increases rapidly with further integration while the unwanted admixture simultaneously decreases rapidly.

III.8.3 Determination of Eigenvalues

Determination of a particular energy eigenvalue started with the integration of the governing equation as described in section III.8.2 for some assumed initial energy and again for another energy which differed by only approximately 100 eV. In the case of a complex

potential, the second energy was chosen so that both its real and imaginary components differed from those of the initial energy. A matching parameter

$$y = \frac{G_{OUT}}{F_{OUT}} - \frac{G_{IN}}{F_{IN}} \quad \text{for the Dirac equation or}$$

$$y = \frac{(rR_{OUT})}{(rR_{OUT})'} - \frac{(rR_{IN})}{(rR_{IN})'} \quad \text{for the Klein-Gordon equation}$$

was defined at the mid-point where the inner and outer solution halves were joined. The (possibly complex) values of this parameter as evaluated for the two energies were used to establish an assumed linear relationship between the values of the matching parameter and those of the state energy. The value of the state energy for which this linear parameterization of the matching parameter vanished was taken as the next trial energy, replacing the one of the original two trial energies which differed the most from the new trial energy. This procedure was repeated until a convergence criterion of two successive iterations where neither component of the trial energy changed by more than one eV was met.

III.8.4 Grid Selection

The point most commonly chosen for matching the inner and outer wave functions in this analysis was the most centrally located antinode in either $G(r)$ (Dirac equation) or in the derivative $d(rR(r))/dr$ (Klein-Gordon equation). For some of the calculations involving the strong-interaction potential, the innermost antinode was

chosen so that the small step sizes needed for the inner portion of the wave function calculation would not increase the calculation time any more than was necessary.

During the development of the eigenvalue search software, a parameterization was derived empirically for the minimum integration stepsize needed to achieve a given precision in the eigenvalue solution. For this analysis, the stepsize was chosen via this parameterization so that the expected precision of the eigenvalue solutions was one eV or less. For each of the two regions (inner and outer) of integration, this stepsize was calculated and rounded down to an integral multiple of the spacing of the potential grid. The exact radius of the matching point was then adjusted to fall an exact multiple of the inner stepsize away from the inner initialization radius.

The minimum radius at which the outer portion of the wave function could be reliably initialized was also parameterized. This exact value of the outer initialization radius was found by adjusting the values from this parameterization upwards so that the radius fell an exact multiple of the outer stepsize beyond the matching point. This tailoring of the pre-defined potential grid to a given state insured the most efficient possible calculation of the eigenvalues.

III.8.5 Corrections

The effects of electron screening and vacuum polarization on the energy of a particular eigenstate were calculated by including the

relevant potentials in the numerical eigenvalue solution. The effects of nuclear recoil, static polarizability, and intrinsic nuclear multipole moments were evaluated by first-order perturbation theory once the energy and the wave function of the state had been calculated. Nuclear recoil effects were calculated via equation I.3-2. Effects of static polarizability of the nucleus and hadron were calculated via equation I.3-8 and I.3-10, with an assumed hadron polarizability of $9 \times 10^{-4} \text{ fm}^3$. The combined effects of nuclear recoil and static polarizability are less than $30 \pm 7 \text{ eV}$ for all transitions in Σ^- -Pb and Σ^- -W exotic atoms except for the final (10 \rightarrow 9) transition in Σ^- -Pb, where the combined effect of $80 \pm 20 \text{ eV}$ is the largest source of uncertainty in the calculation of the transition energy.

Hyperfine splitting due to intrinsic nuclear multipole moments was calculated via equation I.3-12 for Σ^- and I.3-16 for K^- . The only isotope of Pb which has a non-zero intrinsic M1 moment is ^{207}Pb , which has a natural abundance of 22.6%. The (9,8) level of Σ^- - ^{207}Pb has a hyperfine splitting of only $\pm 7 \text{ eV}$. Similarly, the only isotope of W which has a non-zero intrinsic M1 moment is ^{183}W , which has a natural abundance of 14.4%. The (9,8) level of Σ^- - ^{183}W is split by only $\pm 1 \text{ eV}$. Higher-lying states show even less of an effect. The hyperfine structure of the spectra of sigma-hyperonic atoms was thus ignored in this analysis.

By contrast, the (8,7) level of $K^-^{207}\text{Pb}$ is split by approximately ± 105 eV, indicating that hyperfine effects would need to be included in any critical analysis of the spectra of kaonic Pb atoms for strong-interaction widths. The same (8,7) level in $K^-^{183}\text{W}$ is split by only ± 14 eV. This effect can be ignored in all but the most critical lineshape analysis of kaonic atoms formed in natural tungsten because of the low natural abundance (14.4%) of the isotope ^{183}W . No K^- -W transitions below the (10 \rightarrow 9) were included in this analysis. Hyperfine splitting of kaonic atom energy levels was thus ignored.

III.8.6 Sequence of Calculations

Eigenvalues for most states were calculated for a number of special cases. The sequence of eigenvalue calculations for a particular state was chosen for the greatest possible calculational efficiency. The Dirac or Klein-Gordon energy for a point nucleus with no electrodynamic corrections was usually taken as the starting point. The point-nucleus Coulomb potential was inserted into the wave equation, which was then integrated at this energy. The resulting point-nucleus wave function was used to estimate the vacuum polarization, electron screening, and finite-nucleus corrections to the Dirac or Klein-Gordon energy via a first-order perturbation calculation. This estimate was added to the Dirac or Klein-Gordon energy, which was then taken as the initial energy of a numerical eigenvalue search as described in section III.8.3.

The potentials included in this first eigenvalue search were those due to the finite-nucleus Coulomb interaction, electron screening, and vacuum polarization. The resulting eigenvalue was corrected for nuclear recoil and static polarizability effects to give the state energy for the assumption of no strong interactions.

The uncorrected finite-nucleus eigenvalue and its corresponding wave function were used to estimate the effects of a complex strong-interaction optical potential via a first-order perturbation calculation. The resulting estimate of the energy of a state subject to strong-interaction effects was used to initialize another numerical eigenvalue search. The potentials included in this search were the same as in the first, with the addition of a complex strong-interaction optical potential. The resulting complex eigenvalue was corrected for nuclear recoil and static polarizability effects to give the fully corrected state energy in the presence of strong interactions.

III.9 Cascade Simulations

III.9.1 Initial Approximations

Several simplifying assumptions were made in the initial simulations of the hadronic-atomic cascade. Electric quadrupole (E2) and magnetic dipole (M1) transition rates from a given state were found to be four to ten orders of magnitude smaller than the electric dipole (E1) transition rates from the same state, and so were ignored. The E1 rates were calculated by inserting equation I.3-6 into equations I.3-9 and I.3-10 for Σ^- or into equation I.3-8) for K^- . These equations were then evaluated with the help of equation I.3-15. The resulting matrix element was inserted into equation I.3-2, summed as indicated by equations I.3-5 and I.3-16, and multiplied by E^2 (see equation I.3-4) to give a value for the observable transition rate.

Initially, the point-nucleus Dirac (or Klein-Gordon) value from equation I.1-19 (or equation I.1-7) was used for the energy in equation I.3-2. The radial matrix elements of equation I.3-9 (or equation I.3-8) were initially evaluated via the Gordon approximation (equation I.3-17). Absorption due to the strong interaction was initially approximated by first-order perturbation, taking as the set of basis states the finite-nucleus wave functions with no strong interaction.

The sensitivity of the entire set of calculated yields to the imaginary component (width) of the energy eigenvalue of a state (n, ℓ) decreases very rapidly with decreasing ℓ for a given value of n .

This is a result of the concentration of the hadron population towards states having larger values of l (see Section I.4). At the same time, the width of a state (n, l) (largely a function of the hadron-nucleus overlap) decreases rapidly with increasing l . There thus exists an n_{max} above which there are no observable strong interaction effects on the calculated yields. Studies of the functional dependence of the width on n and on l indicated a very gradual dependence on n for a given value of l . It was determined empirically that no significant changes occurred in the calculated yields when the widths of all states $(n > n_{max}, l)$ were replaced by that of the state (n_{max}, l) . Since the calculation of the exact width rapidly becomes more difficult as n increases, this resulted in a significant savings of computation time.

For values of n where the cascade is significantly affected by the strong interaction, there is an abrupt decrease in the hadron population density as l decreases to some characteristic value l_{min} . This is caused both by the strength of the strong-interaction absorption and by its rapid increase with decreasing l . As a result, the widths of states having values of l less than l_{min} , although quite large, have no observable effect on the calculated yields. Due to the gradual dependence of the width on n , l_{min} was found to be independent of n . Similarly, the rapid decrease of the width with increasing l insures that there exists some l_{max} beyond which the widths are effectively zero. l_{max} , like l_{min} , was found to be independent of n . The values of n_{max} , l_{max} , and l_{min} determined empirically for each hadron-nucleus system considered in this analysis

are listed in Table XXI.

III.9.2 Optimization of Computational Technique

For each of the hadron-nucleus systems considered in this analysis, the final few transitions of the cascade were so severely affected by finite-nuclear and strong-interaction effects that the Gordon approximation (equation I.3-17) failed adequately to represent the radial matrix elements of equations I.3-8 and I.3-9. The wave functions associated with the finite-nucleus complex energy eigenvalues were integrated numerically to calculate the radial matrix elements for these final few transitions. The energies used in equation I.3-2 for these transitions were derived from the real component of the finite-nucleus complex eigenvalues.

Similarly, first-order perturbation calculations failed to give adequate precision when used to evaluate the strong-interaction widths of the last few states involved in the cascade. The imaginary component of the finite-nucleus complex eigenvalue was used to calculate the strong-interaction absorption out of these last few states.

The ranges of validity of the Gordon approximation and of the first-order perturbation calculation were determined empirically for each hadron-nucleus system considered in this analysis. For each of the last few transitions, the approximated values of the rates and widths were replaced by the exact values and the cascade was recalculated. Any such substitutions which resulted in a change of 1%

or more in the calculated yields were retained in all further calculations. The states and transitions for which exact width and rate calculations were necessary are listed in Table XXI.

TABLE XXI

Optimization Parameters for the Cascade Simulation

	$K^- - W$	$K^- - Pb$	$\Xi^- - W$	$\Xi^- - Pb$
n_{max}	15	15	16	16
l_{max}	9	9	12	12
l_{min}	6	6	8	8
Transitions requiring exact rate calculation	(7 \rightarrow 6)	(7 \rightarrow 6)	(11 \rightarrow 10) (10 \rightarrow 9)	(11 \rightarrow 10) (10 \rightarrow 9)
States requiring exact width calculation	$n \leq 12$	$n \leq 12$	$n \leq 12$	$n \leq 12$

III.9.3 Determination of Initiation Parameters

The values of the initial distribution parameters for each hadron-nucleus system were determined from those transitions which were relatively unaffected by the strong interaction. These transitions were determined by running the simulation of each cascade

with an assumed value for the strong-interaction effective scattering length \bar{a} taken from Reference [25] and again with \bar{a} set equal to zero. Any transitions for which the total calculated yield changed by more than 2% were excluded from the analysis of the initial distribution parameters.

The remaining transitions were fitted to a functional form which included all components of the X-ray multiplet having expected yields greater than 0.1% of the yield of the strongest component. The separations of the various components were fixed to values derived from the energy eigenvalue calculations of Section III.8 as interpreted by the energy calibration of Section III.5. The lineshape parameters σ , λ , q , and χ (see Section III.4) were fixed to values taken from the parameterizations of Section III.5. The Compton-shelf parameter τ was significant only for high-statistics datasets having a good signal-to-noise ratio, and so was omitted from these fits. The amplitude ratios of the various components were fixed at values determined by folding the effects of detector efficiency (Section III.6) and target transmission (Section III.7.2) into the yields calculated by the cascade simulation with the currently assumed value of \bar{a} . The only free parameters in these fits were the centroid of the circular component

$$(n, l=(n-1)) \longrightarrow ((n-1), l=(n-2))$$

and its area, plus any background parameters.

In the case of Σ^- transitions where there are two circular components (one spin-up and one spin-down), the spin-down (i.e., $j = \ell - 1/2$) component was chosen for reasons of software convenience as the primary component of the fit. The area and centroid of the spin-up (i.e., $j = \ell + 1/2$) circular component was fixed relative to that of the spin-down circular component in a manner exactly analogous to the non-circular components. In the discussion that follows, the term 'circular component' as applied to Σ^- atom transitions generally refers to the spin-down component of the circular doublet.

The fitted area of the circular component of each data peak and the statistical error on this area were scaled by $(1+q)/\epsilon T$, where q is the pileup amplitude, ϵ is the detector relative efficiency, and T is the relative target transmission. The uncertainties in ϵ and T were added in quadrature with that of the area. This resulted in a measured relative yield, with error bars, for the circular component of each multiplet.

These measured yields (grouped by run number and by detector) were divided by the yields calculated by the cascade simulation. The resulting sets of ratios were fitted to constants to determine the overall normalizations of the measured yield sets relative to the calculated yields. The χ^2 of these normalization fits were taken as the optimization parameters for the cascade simulations. The input parameters of the cascade were adjusted for each hadron-nucleus system so as to minimize the χ^2 (summed over runs and detectors) of the normalization fits for that particular system.

Initial applications of this analysis method to the K^- -Pb system exhibited unreasonably large values of χ^2 which could not be significantly improved by adjusting the initial distribution parameters a and b of the cascade simulation. It was observed that the yield factor

$$(\text{measured yield})/(\text{calculated yield})$$

had a strong energy dependence of a general form which was very similar to the effects of vertical beam steering on the target transmission curves (see Section III.7.2). The vertical beam steering parameter x_5 was thus included as an adjustable input parameter to the analysis. Figure 26 shows a representative plot of the yield factors of the K^- -Pb system with $x_5=0$ (beam centered on target) and $x_5=-2$ (beam passes 2 cm below center of target).

It is felt that these variations in the parameter x_5 do not represent the actual physical geometry of the beam steering. Rather, it appears that this is a convenient way to accommodate the many small differences between the idealized target geometry represented in the Monte-Carlo software and the physically-realized target, with its minor misalignments and (in the case of Pb) wrinkles of the target foils. Such slight imperfections in the target construction, detected by X-ray photographs taken of the target assembly during setup, were unavoidable. It was not considered practical to include these effects explicitly in the Monte-Carlo calculations.

More transitions, covering a wider energy region, were observable for the kaonic than for the Σ^- atoms. The kaonic atom data peaks also contained considerably more statistics than did the Σ^- atom data peaks. As a result, the kaonic atom yield fits were much more sensitive to x_S than were the Σ^- atom yield fits. The Σ^- yield fits therefore used target transmission curves calculated for the value of x_S determined from the kaonic atom analysis.

The tungsten data required values of x_S different for detector C from those for detectors A and B. This is not surprising, since the slight differences in the detection geometries among the three detectors are of a symmetrical nature between detectors A and B, but not between detectors A and C or detectors B and C. Perhaps more surprising is the lack of any such observable difference in the lead data.

The tungsten data also required two different sets of beam steering parameters, $[(x_S^{82})_{A,B}, (x_S^{82})_C]$ and $[(x_S^{84})_{A,B}, (x_S^{84})_C]$, for the two different tungsten runs (1982 and 1984). This, also, is not surprising, as the tungsten target was dismantled and re-mounted in the interim between the 1982 and 1984 runs, allowing the positions of the tungsten foils to shift about somewhat. The lead target remained in position throughout the 1982 lead run.

For each hadron-nucleon system, the values of x_S , Q and b which resulted in the minimum value of the total normalization χ^2 were determined first for x_S , which had the strongest effect. The transmission curves were calculated for a range of values of x_S , and

the yield fits were repeated for each set of curves. The normalization χ^2 was plotted as a function of z_5 and fitted to a polynomial. This polynomial was evaluated for a range of values to determine an estimate of the value of z_5 which would minimize the χ^2 and the values of z_5 which resulted in a χ^2 greater by one than this minimum value. This range determined the error assigned to the estimate of z_5 . The transmission curves were re-calculated for the value of z_5 so determined. The resulting transmission curves were used in all subsequent yield fits.

Next, the χ^2 was minimized on Q , which had the median effect of the three input parameters. The cascade simulation was run for a range of values of Q , and the yield fits were re-computed for each set of calculated yields. The normalization χ^2 was plotted as a function of Q and fitted to a polynomial. The estimate of Q and its associated errors were determined in a manner similar to that used for z_5 .

Finally, the χ^2 was minimized on b , which had the least effect. The cascade simulation was run for a range of values of b , with z_5 and Q fixed at the values determined above. A χ^2 -vs- b plot was used as before to find the best estimate of b and the expected error on this estimate.

If necessary, this series of three χ^2 minimizations was repeated until no parameter values changed by more than 0.1σ . The resulting values of the beam steering parameter z_5 and the hadronic initial distribution parameters Q and b are listed in Table XIII. The

measured and calculated relative yields of the circular components of the most important hadronic transitions are listed in Tables XXIII and XXIV. The calculated yields of the individual components of those Σ^- transitions in W and Pb which were included in this analysis are listed, respectively, in Tables XXV and XXVI. The yields of those Σ^- transitions which were affected significantly by the strong interaction are discussed in more detail in the next chapter.

TABLE XXII

Beam Steering and Hadron Initial Distribution Parameters

Dataset	z_5	a	b
K^- -Pb	-1.86 ± 0.18	0.118 ± 0.009	0.93 ± 0.30
Σ^- -Pb	Same as K^- -Pb	0.090 ± 0.010	1.00 (no effect)
1982 K^- -W (Det A+B)	-2.03 ± 0.14	0.020 ± 0.006	1.02 ± 0.14
1982 K^- -W (Det C)	-1.00 ± 0.29		
1984 K^- -W (Det A+B)	-1.95 ± 0.15		
1984 K^- -W (Det C)	-3.65 ± 0.52		
1982 and 1984 Σ^- -W	Same as K^- -W	0.060 ± 0.017	1.00 (no effect)

TABLE XIII

Measured and Calculated Kaonic Atom X-ray Relative Yields
(Circular components only)

Strong Interaction effects calculated with $\bar{a}=(0.44+i0.83)$ fm

$K^- - W$ Transition	Y(measured)	Y(calculated)	
		No S.I.	S.I. Included
11 \rightarrow 10	0.422 ± 0.132	0.641	0.641
10 \rightarrow 9	0.698 ± 0.077	0.816	0.816
+13 \rightarrow 11			
9 \rightarrow 8	1.00	1.000	1.000
8 \rightarrow 7 *	1.294 ± 0.087	1.188	1.142
14 \rightarrow 12 ++	0.161 ± 0.025	0.063	0.063
12 \rightarrow 10	0.074 ± 0.012	0.083	0.083
11 \rightarrow 9	0.116 ± 0.012	0.103	0.103
10 \rightarrow 8	0.118 ± 0.014	0.118	0.118
9 \rightarrow 7 *	0.180 ± 0.026	0.125	0.113

$K^- - Pb$ Transition	Y(measured)	Y(calculated)	
		No S.I.	S.I. Included
12 \rightarrow 11	0.598 ± 0.086	0.593	0.595
11 \rightarrow 10	0.652 ± 0.065	0.737	0.739
10 \rightarrow 9	0.847 ± 0.055	0.874	0.877
+13 \rightarrow 10			
9 \rightarrow 8	1.00	1.000	1.000
8 \rightarrow 7 *	1.093 ± 0.042	1.112	0.940
7 \rightarrow 6 *	0.111 ± 0.017	1.209	0.102
15 \rightarrow 13	0.037 ± 0.008	0.051	0.051
14 \rightarrow 12	0.062 ± 0.008	0.061	0.061
12 \rightarrow 10	0.066 ± 0.004	0.069	0.069
11 \rightarrow 9	0.097 ± 0.003	0.076	0.076
10 \rightarrow 8	0.103 ± 0.006	0.077	0.077

* ==> Affected by Strong Interaction

++ ==> Contaminated - excluded from the analysis

TABLE XXIV

Measured and Calculated Σ^- Atom X-ray Relative Yields
(Circular $j = \ell - 1/2$ components only)

Strong Interaction effects calculated with
 $\bar{r} = (0.928 \pm 0.022)$ fm for W
 $\bar{r} = (0.350 \pm 0.135)$ fm for Pb

Σ^- -W Transition	Y(measured)	Y(calculated)	
		No S.I.	S.I. Included
14 \rightarrow 13	0.615 \pm 0.080	0.747	0.747
13 \rightarrow 12	0.806 \pm 0.075	0.875	0.875
12 \rightarrow 11	1.00	1.000	1.000
11 \rightarrow 10	1.137 \pm 0.076	1.120	1.111
10 \rightarrow 9	1.201 \pm 0.072	1.231	1.127
+13 \rightarrow 11	*		
15 \rightarrow 13	0.053 \pm 0.016	0.072	0.072
14 \rightarrow 12	0.093 \pm 0.016	0.080	0.080
12 \rightarrow 10	0.118 \pm 0.580	0.087	0.085

Σ^- -Pb Transition	Y(measured)	Y(calculated)	
		No S.I.	S.I. Included
15 \rightarrow 14	0.576 \pm 0.044	0.686	0.687
14 \rightarrow 13	0.791 \pm 0.042	0.796	0.797
13 \rightarrow 12	0.874 \pm 0.036	0.902	0.903
12 \rightarrow 11	1.00	1.000	1.000
11 \rightarrow 10	1.083 \pm 0.035	1.089	1.070
10 \rightarrow 9	0.623 \pm 0.047	1.166	0.596
+13 \rightarrow 11	*		
16 \rightarrow 14	0.068 \pm 0.008	0.058	0.058
15 \rightarrow 13	0.054 \pm 0.008	0.064	0.064
14 \rightarrow 12	0.063 \pm 0.008	0.067	0.067

* \Rightarrow Affected by Strong Interaction

TABLE XV

Calculated Yields of Σ^- -W X-ray Components (X rays/Atom)Strong Interaction effects calculated with $\bar{a}=(0.928+10.022) \text{ fm}$

	Circular	1'st nc	2'nd nc	3'rd nc	4'th nc
<u>(14→13)</u>					
Spin-up	0.2242	0.0672	0.0197	0.0054	0.0011
Spin-down	0.2076	0.0618	0.0180	0.0049	0.0010
<u>(13→12)</u>					
Spin-up	0.2643	0.0658	0.0159	0.0030	0.0001
Spin-down	0.2431	0.0601	0.0144	0.0027	0.0001
<u>(12→11)</u>					
Spin-up	0.3045	0.0589	0.0081	----	----
Spin-down	0.2780	0.0537	0.0071	----	----
<u>(11→10)</u>					
Spin-up	0.3405	0.0418	----	----	----
Spin-down	0.3087	0.0371	----	----	----
<u>(10→9)</u>					
Spin-up	0.3510	0.0005	----	----	----
Spin-down	0.3134	0.0003	----	----	----
<u>(16→14)</u>					
Spin-up	0.0215	0.0133	0.0058	0.0021	0.0005
Spin-down	0.0199	0.0122	0.0053	0.0019	0.0004
<u>(15→13)</u>					
Spin-up	0.0242	0.0126	0.0046	0.0011	----
Spin-down	0.0223	0.0115	0.0041	0.0010	----
<u>(14→12)</u>					
Spin-up	0.0260	0.0110	0.0028	0.0001	----
Spin-down	0.0237	0.0100	0.0025	0.0001	----
<u>(13→11)</u>					
Spin-up	0.0258	0.0061	----	----	----
Spin-down	0.0235	0.0054	----	----	----

TABLE XXVI

Calculated Yields of Σ^- -Pb X-ray Components (X rays/Atom)Strong Interaction effects calculated with $\bar{a}=(0.350+i0.135)$ fm

	<u>Circular</u>	<u>1'st nc</u>	<u>2'nd nc</u>	<u>3'rd nc</u>	<u>4'th nc</u>
<u>(15→14)</u>					
Spin-up	0.2396	0.0678	0.0188	0.0049	0.0009
Spin-down	0.2230	0.0628	0.0173	0.0045	0.0008
<u>(14→13)</u>					
Spin-up	0.2795	0.0661	0.0152	0.0027	---
Spin-down	0.2588	0.0608	0.0139	0.0024	---
<u>(13→12)</u>					
Spin-up	0.3186	0.0610	0.0098	0.0002	---
Spin-down	0.2931	0.0556	0.0088	0.0002	---
<u>(12→11)</u>					
Spin-up	0.3559	0.0501	0.0009	---	---
Spin-down	0.3248	0.0456	0.0008	---	---
<u>(11→10)</u>					
Spin-up	0.3847	0.0114	---	---	---
Spin-down	0.3476	0.0096	---	---	---
<u>(10→9)</u>					
Spin-up	0.2245	0.0001	---	---	---
Spin-down	0.1936	0.0001	---	---	---
<u>(16→14)</u>					
Spin-up	0.0201	0.0118	0.0049	0.0017	0.0004
Spin-down	0.0187	0.0109	0.0045	0.0016	0.0003
<u>(15→13)</u>					
Spin-up	0.0224	0.0111	0.0039	0.0009	---
Spin-down	0.0207	0.0102	0.0036	0.0008	---
<u>(14→12)</u>					
Spin-up	0.0238	0.0097	0.0023	---	---
Spin-down	0.0219	0.0089	0.0020	---	---
<u>(13→11)</u>					
Spin-up	0.0241	0.0073	0.0002	---	---
Spin-down	0.0220	0.0066	0.0002	---	---

Chapter IV
RESULTS AND CONCLUSIONS

IV.1 Widths and Shifts

The functional form $R_3(A; E_\gamma, \sigma, \lambda, q, \delta)$ derived in Section III.4 has no provisions for transition energies which have been broadened by the strong interaction. The intensity of emitted radiation for such transitions is generally assumed to follow a Lorentzian distribution [99]:

$$IV.1-1) \quad L(E_\gamma; E_0, \Gamma) = \frac{\Gamma/2\pi}{(E_\gamma - E_0)^2 + \Gamma^2/4}$$

Strictly speaking, the initial as well as the final state of the transition has a characteristic Lorentzian width; respectively, Γ_i and Γ_f . In practice, Γ_i is so much smaller than Γ_f that it may be either included as a slight final correction to the width value or else ignored. The complete detector response function which should be fitted to these transitions is thus a convolution of a Lorentzian by the detector response function R_3 :

$$IV.1-2) \quad R_4(A; E_\gamma, \sigma, \lambda, q, \delta, \Gamma) = R_3(A; E_\gamma, \sigma, \lambda, q, \delta) * L(E_\gamma; E_0, \Gamma)$$

Unfortunately, it was not possible to find an effective algorithm to calculate the $[\exp(z)\operatorname{erfc}(z)] * L(y)$ terms involved in this response function short of a direct numerical evaluation of the convolution integral. This method provided adequate values for the response function R_4 , but required large amounts of computation time and did not provide the derivatives needed for the application of a least-squares fitting algorithm (see Section III.3).

In the limit $\lambda \rightarrow 0$, the function $R_3(A; E_0, \sigma, \lambda, q, \gamma)$ contains only Gaussian and $[\exp(z)\operatorname{erfc}(z)]$ terms. A convenient algorithm based on the method of continued fractions exists for the evaluation of the Voigt (1,2, Gaussian*Lorentzian) integral [100]. This algorithm was incorporated into the least-squares fitting software as a useful, although clearly incomplete, approximation of the detector response function R_4 . The lack of the charge trapping parameter λ in this approximate function $\tilde{R}_4(A; E_0, \sigma, q, \gamma, \Gamma)$ can be largely accommodated by shifting the centroid parameter E_0 by an amount $-\lambda$ and by replacing σ with $\sigma_{\text{eff}} \approx \sqrt{\sigma^2 + \lambda^2}$. More appropriate values of σ_{eff} may be found by using functions based on the $\lambda \rightarrow 0$ limit of R_3 to fit simulated datasets based on the proper form of R_3 .

The fits to the Σ^- data peaks which were affected by the strong interaction ($10 \rightarrow 9$) transition in $\Sigma^- - \text{W}$ and $\Sigma^- - \text{Pb}$) followed closely the yield fits of section III.9.3, but used the functional form $A_0 \tilde{R}_4(A; (E_0 - \lambda), \sigma_{\text{eff}}, q, \gamma, \Gamma)$ for those components which had an expected strong interaction width Γ greater than 1 eV. The remaining components were assumed to have the functional form

$A_3 R_3(A; E_0, \sigma, \lambda, q, \gamma)$ as parameterized in section III.5. Only the circular components (both spin-up and spin-down) of the (10 \rightarrow 9) transition in Σ^- -W and Σ^- -Pb required the form \widetilde{R}_4 . The non-circular components of the (10 \rightarrow 9) transition were so sharply attenuated by strong interaction absorption that they could be excluded from these fits, and all significant components of the underlying (13 \rightarrow 11) transition were described adequately by the form R_3 .

The width of the spin-up circular component is not necessarily equal to that of the spin-down. The width of the spin-up component was thus fixed relative to that of the spin-down, with a relative offset determined from the energy calculations of Section III.8. The width of the spin-down circular component was the only free strong-interaction width parameter in these fits.

An iterative method was devised to correct for the residual inadequacies of the function \widetilde{R}_4 . Simulated datasets were generated based on the function $A_0 R_4(A; E_0, \sigma, \lambda, q, \gamma, \Gamma)$ as evaluated via numerical integration. These datasets were then fitted to forms based on $A_0 \widetilde{R}_4$. The values of A_0 , E_0 and Γ were adjusted to improve the agreement between the parameter values from these fits and the values resulting from fits to the data peaks, where the same functional form was used for both sets of fits. This procedure was repeated until the values of A_0 , E_0 and Γ stabilized. The values of Γ and E_0 determined from the data by this iterative method were converted from the ADC-channel scale to the energy scale via the parameterizations of Table XVII. The strong-interaction shift $\epsilon = E_{\text{meas}} - E_{\text{calc}}$ of the

transition was determined from this converted value of E_0 and from the energy calculated for the transition in Section III.8.

IV.2 Yield Reductions

The circular component areas determined from the strong interaction fits were, as were the yield fits in Section III.9.3, multiplied by $(1+q)/\epsilon T$ to give estimates and probable errors for the relative yields of the circular components. These measured yields were divided by the normalization constants of their respective datasets relative to the cascade simulation (as determined in Section III.9.3) so that they could be compared directly with the yield values calculated by the cascade simulation. The ratio of measured to calculated yield of the $\Sigma^- (10 \rightarrow 9)$ transition, averaged over all datasets analyzed for a particular hadron-nucleus system, was used to determine the strong-interaction absorption out of the (10,9) state of that system.

The yield y_j of a particular transition may be expressed in terms of the fraction of the initial state population which exits the state by way of the desired radiative process, rather than by any of the competing processes:

$$\text{IV.2-1) } y_j = d \frac{R_j}{S + \sum_i (R_i + A_i)}$$

where d is the initial state population, R_j is the rate of the desired radiative process, $\sum_i (R_i + A_i)$ is the sum of all possible radiative and Auger processes (including the desired radiative process), and S is

the rate of strong-interaction absorption. The value of S which results in a desired value y for y_j may be determined from equation IV.2-1, and may be expressed in terms of some initially assumed value S_0 and its resulting calculated yield y_0 :

$$\text{IV.2-2)} \quad (S-S_0) = \left[\frac{y_0}{y} - 1 \right] [S_0 + \sum (R_i + A_i)]$$

Here, the ratio (y_0/y) corresponds to the inverse of the ratio of measured to calculated yields determined from the strong interaction fits. For each hadron-nucleus system, the value of S was calculated via equation IV.2-2 over a range of values of (y_0/y) which was determined by the mean ratio of measured to calculated yields for that system and by the expected error of this mean ratio. The resulting values and errors for S were related to the imaginary component of the initial-state energy eigenvalue by the relationship

$$\text{IV.2-3)} \quad S = \Gamma/\hbar = -2 \text{Im}(E)/\hbar$$

IV.3 Scattering Lengths

From the assumption that the strong interaction effects on the energy of the $(10,9)$ state are observable only through the yield reductions of the $(10 \rightarrow 9)$ transition (expected effects are less than 25 eV), the complex energy eigenvalue of the $(9,8)$ state may be deduced from the observed shift and broadening of the $(10 \rightarrow 9)$ transition. An iterative method was used to find the value of the effective strong interaction scattering length \bar{a} which reproduced this

eigenvalue.

It was found that the value of \bar{a} ((0.928+10.022) fm) which reproduced the shift (650 eV) and width (380 eV) of the (10→9) transition in Σ^-W also reproduced to within 1.5 σ the width of the (10,9) state (0.3 eV) as deduced from the reduction in yield of the (10→9) transition.

The situation was not so simple for the Σ^-Pb system, since there was a lesser amount (≈ 290 eV) of broadening in the (10→9) transition of this system. A value of \bar{a} could be found which reproduced simultaneously the observed shift (510 eV) of the (10→9) transition and the deduced width (17 eV) of the (10,9) state, but the width of the (9,8) state which was calculated with this value ((0.350+10.135) fm) of \bar{a} was in excess of one keV, in clear disagreement with the data. Similarly, the value of \bar{a} ((0.247+10.039) fm) which reproduced the observed shift and broadening in the (10→9) transition predicted only a 17% reduction in the yield of this transition. This is clearly at odds with the data, as the yield of the (10→9) transition in Σ^-Pb is only $53 \pm 4\%$ of what one would expect in the absence of the strong interaction (see Table XXIV).

The cascade simulation for the Σ^-Pb system was found to be much more sensitive to the widths of states having $l=9$ than to those of states having $l=8$. Values of \bar{a} determined from the Σ^-Pb data and intended for further use in the analysis (i.e., fine-tuning of the cascade simulation) were thus determined from the shift and yield

reduction of the (10→9) transition, rather than from the shift and width of the (9,8) state.

Once the value of \bar{a} had been determined for the Σ^- -W and Σ^- -Pb systems, the energy eigenvalues and transition rates which had significant strong-interaction effects on the cascade simulation (see Sections III.9.1 and III.9.2) were re-calculated and the cascade simulation was updated accordingly. The entire procedure was then repeated until the values of \bar{a} stabilized. The values of the shift, width, yield reduction, and deduced initial-state width which resulted from this iterative process are listed for the spin-down circular components of the Σ^- -W and Σ^- -Pb systems in Table XIVII. The values of the effective scattering length \bar{a} which reproduced these effects in optical-model calculations are listed in Table XXVIII.

TABLE XIVII

Strong-Interaction Effects Measured in Σ^- -W and Σ^- -Pb
(Quoted for spin-down circular components only)

	Σ^- -W	Σ^- -Pb
Shift ($E_{\text{meas}} - E_{\text{calc}}$) of (10→9) Transition (eV)	650 +/- 30	510 +/- 50
Width (eV) of (10→9) Transition	380 +/- 70	290 +/- 140
(10→9) Effective Yield (Measured/Calculated-No SI)	.98 +/- .04	0.53 +/- 0.05
Deduced Width (eV) of (10,9) State	0.3 +/- 0.5	17 +/- 3

TABLE XXVIII

Strong-Interaction Effects Calculated for $\Sigma^- - N$ and $\Sigma^- - Pb$

$\Sigma^- - N$		$\bar{a} = (0.928+10.022) \text{ fm}$		$\bar{a} = (0.928+10.022) \text{ fm}$	
		Shift (eV)	Width (eV)	Shift (eV)	Width (eV)
<u>States:</u>	(10,9,↑)	-4.5	0.88		
	(10,9,↓)	-5.5	0.94		
	(9,8,↑)	-577.	303.		
	(9,8,↓)	-649.	382.		
<u>Transitions:</u>	(10→9,↑)	572.	304.		
	(10→9,↓)	644.	383.		
Spin-averaged	(10→9)	606.	341.		

$\Sigma^- - Pb$	$\bar{a} = (0.247+10.039) \text{ fm}$		$\bar{a} = (0.350+10.135) \text{ fm}$	
	Shift (eV)	Width (eV)	Shift (eV)	Width (eV)
<u>States:</u>				
(10,9,↑)	-8.2	3.8	-12.3	15.8
(10,9,↓)	-10.8	4.0	-15.1	17.0
(9,8,↑)	-481.	252.	-499.	1180.
(9,8,↓)	-515.	270.	-519.	1270.
<u>Transitions:</u>				
(10→9,↑)	473.	255.	487.	1200.
(10→9,↓)	504.	275.	504.	1290.
(10→9,avg)	487.	264.	495.	1242.

IV.4 Discussion and Theoretical Implications

Several attempts were made to find modifications of the strong interaction optical potential which would reproduce the unexpected behavior of the Σ^- -Pb system. Most notable among them was the introduction of a parameterization of the potential of Brockmann and Oset [74], which exhibits a saturation of the imaginary component at nuclear densities greater than about 0.7 that of the normal nuclear medium. Surprisingly, calculations based on this potential were no more able to account for the discrepancy between the widths of the Σ^- -Pb (10,9) and (9,8) states than were calculations based on the usual optical model.

Studies of the radial dependence of the hadron-nucleus overlap function for the states (10,9) and (9,8), as calculated with the usual optical-model potential for the Σ^- -Pb system, showed almost no difference in the shape of the overlap; i.e., the (9,8) state does not penetrate significantly farther into the nuclear medium than does the (10,9) state. Rather, the increased effect of the optical-model potential on the (9,8) state relative to that on the (10,9) state is due more to the greater fraction of the (9,8) state particle density which lies within the nuclear medium. Such studies seem to indicate that the state-dependence of the effective scattering length \bar{a} which was observed in the Σ^- -Pb system must be due to effects other than the spatial or nuclear-density dependence of the Σ^- -Pb potential.

It is interesting to note that the principal isotope of Pb, ^{208}Pb , has a 'magic' number of both protons and neutrons (Shell model [96]), while the principal isotope of W, ^{184}W , has a non-'magic' number of both protons and neutrons. Slight differences from isotope to isotope between the proton and neutron distributions of the nucleus (arising possibly from Shell-model effects) could perhaps explain the different behavior of the Σ^- -W and Σ^- -Pb systems if there were a significant difference in the Σ^- -p and Σ^- -n effective scattering lengths. A comparison of strong interaction effects in Σ^- atoms formed with nuclei having a 'magic' number either of protons or of neutrons to those in Σ^- atoms formed with non-'magic' nuclei could result in more information.

APPENDIX A

Calculation of Higher-Order Vacuum Polarization Potentials

An accurate numerical method for the evaluation of the $\propto (Z\alpha)^{3,5,7}$ vacuum polarization potential about a finite nucleus has been demonstrated by Rinker, Willets and Steffen [9,29,34]. Based on Schwinger's [101] expression for the vacuum polarization charge density (see equation I.2-1), it requires the summation of the state densities of all possible solutions (bound or unbound, electron or positron) for the Dirac equation in the presence of the finite nucleus. In practice, the continuum of unbound states implicit in this sum is approximated by a discrete set of states, the momenta of which form an equally spaced grid. States having either large momenta or large angular momenta are found to contribute little to the vacuum polarization charge density, so that the summation over all possible states may be truncated for momenta greater than some P_{max} and for angular momenta greater than some l_{max} . This discretization and truncation of the continuum reduces the summation of equation I.2-1 to a finite, if large, number of terms.

Each term in equation I.2-1 must be calculated as many as four different ways in order to remove the divergences linear in $(Z\alpha)$ and to insure gauge invariance and charge conservation. There are many terms in the summation that nearly cancel each other, so that a high

degree of numerical precision must be maintained throughout the calculation if the final result is to have a useful degree of accuracy. Due to the complexity of the calculations involved, such a direct numerical approach was deemed impractical for this analysis.

The results of Rinker, Wilets and Steffen [9,29,34] are presented in the form of several plots depicting calculated potentials and several tables containing the calculated effects of these potentials on the energy eigenvalues of selected lower-lying states of muonic atoms. A visual parameterization was made of the potential about $^{208}_{82}\text{Pb}$ (see Figure 1) which, when incorporated into the energy calculation algorithm of this analysis, reproduced the effects tabulated by Rinker and Wilets [34] for muonic $^{208}_{82}\text{Pb}$. It was unclear how to modify this visual parameterization to include nuclei other than $^{208}_{82}\text{Pb}$.

For radii outside of the nuclear charge distribution, it was observed that the visual parameterization of the $\propto (Z\alpha)^{3,5,7}$ potential for $^{208}_{82}\text{Pb}$ taken from Rinker and Wilets [34] differed from the point-nucleus potential calculated by Blomqvist [8] by a factor which behaved roughly as $\exp(-1/r)$. A numerical parameterization was devised, based on this observation, which consisted of multiplying the point-nucleus of Blomqvist [8] by a factor $\exp[-b/(c+r)]$, where b and c are adjustable parameters. For radii larger than 10 fm and with the proper choice of b and c , this parameterization agreed to within about 10 eV with the visual parameterization. For radii less than 10 fm, this numerical parameterization gave values for the potential which

were as much as 300 eV larger than those of Rinker and Wilets [34]. This discrepancy could be greatly reduced by performing a linear convolution of the parameterization over the nuclear charge distribution, a process which had almost no effect on the potential for radii larger than 10 fm. The effects on the energy eigenvalues of muonic ${}_{82}^{208}\text{Pb}$ due to the $\propto(Z\alpha)^{3,5,7}$ vacuum polarization potential were calculated by inserting this numerical parameterization into the energy calculation algorithm described in Section III.8. The results agreed with the tabulated effects of Rinker and Wilets [34] to within three eV.

In an effort to extend this parameterization to other nuclei, the parameters b and c were expressed in terms of the half-maximum radius of the (assumed Fermi) nuclear charge distribution. The effects of this parameterized $\propto(Z\alpha)^{3,5,7}$ potential on the energy eigenvalues of a number of muonic systems were calculated as before and compared with the tabulated results of Rinker, Wilets and Steffen [29,34]. The values $b=3R_N/4$ and $c=R_N/4$ were found to give the best results for ${}_{82}^{208}\text{Pb}$, and gave good agreement for all nuclei lighter than ${}_{82}^{208}\text{Pb}$, as shown in Table A. Although not as accurate for nuclei heavier than ${}_{82}^{208}\text{Pb}$, this parameterization remains a useful approximation for nuclei as heavy as ${}_{98}^{251}\text{Cf}$.

TABLE A

Comparison of Parameterized to Exact Vacuum Polarization Effects
on Energy Eigenvalues of Muonic Atoms

Z	A	Max Error	Other Errors
26	56	2 eV (1s)	< 1 eV
56	138	4 eV (1s)	< 3 eV
74	182	3 eV (1s)	< 2 eV
74	186	2 eV (3d)	< 1 eV
78	195	7 eV (1s)	< 3 eV
82	208	3 eV (1s)	< 2 eV
92	238	29eV (1s)	< 14eV (R _N =6.9fm)
92	238	13eV (1s)	< 4 eV (R _N =7.55fm)
98	251	43eV (1s)	23eV (2p), also < 11eV (R _N =7.1fm)
98	251	29eV (1s)	16eV (2p), also < 7 eV (R _N =7.7fm)

In summary, the $\propto (Z\alpha)^{3,5,7}$ vacuum polarization potential generated by a finite nucleus may be approximated by:

- 1) calculating the point-nucleus potentials via Reference [8],
 - 2) multiplying by $\exp[-b/(c+r)]$, where $b=3R_N/4$ and $c=R_N/4$,
- and
- 3) convoluting linearly over the nuclear charge distribution.

For exotic-atom energy calculations about nuclei having $Z \leq 82$, this parameterization is expected to be good to within about five eV.

BIBLIOGRAPHY

- 1) P.Vogel, Phys.Rev. A7, 63 (1973).
- 2) C.W.DeJaeger, H.DeVries and C.DeVries, At.Data Nucl.Data Tables 14, 479 (1974).
- 3) E.H.Wichmann and N.W.Kroll, Phys.Rev. 101, 843 (1956).
- 4) R.C.Barrett, S.J.Brodsky, G.W.Erickson and M.H.Goldhaber, Phys.Rev. 166, 1589 (1968).
- 5) T.Dubler, K.Kaesor, B.Robert-Tissot, L.A.Schaller, L.Schellenberg and H.Schneuwly, Nucl.Phys. A294, 397 (1978).
- 6) Carboni et. al., Nuovo Cim. A34, 493 (1976).
- 7) G.Carboni, G.Gorini, G.Torelli, L.Palffy, F.Palmonari and E.Zavattini, Nucl.Phys. A278, 381 (1977).
- 8) J.Blomqvist, Nucl.Phys. B48, 95 (1972).
- 9) G.A.Rinker Jr. and L.Wilets, Phys.Rev. A12, 748 (1975).
- 10) J.Calmet and D.A.Owen, J.Phys. B12, 169 (1979).
- 11) E.Boric and G.A.Rinker, Phys.Rev. A18, 324 (1978).
- 12) K.Gell et. al., Phys.Rev.Lett. 51, 1131 (1983).
- 13) S.C.Cheng et.al., Nucl.Phys. A254, 381 (1975).
- 14) G.Dugan et.al., Nucl.Phys. A254, 396 (1975).
- 15) B.L.Roberts et.al., Phys.Rev. D12, 1232 (1975).
- 16) D.W.Hertzog et.al., Phys.Rev.Lett. 51, 1131 (1983).
- 17) P.D.Barnea et.al., Nucl.Phys. A231, 477 (1974).
- 18) C.J.Batty et.al., Nucl.Phys. A329, 407 (1979).
- 19) M. Leon, Nucl.Phys. A260, 461 (1976).
- 20) E.Boric and G.A.Rinker, Rev.Mod.Phys. 54 67, (1982).
- 21) J.D.Bjorken and S.D.Drell, Relativistic Quantum Mechanics, (McGraw-Hill, New York N.Y., 1964)

- 22) H.A.Bethe and E.E.Salpeter, Quantum Mechanics of One- and Two-Electron Atoms, (Springer-Verlag, Berlin, 1957)
- 23) L.I.Schiff, Quantum Mechanics, (McGraw-Hill, New York N.Y., 1949)
- 24) M.Abramowitz and I.A.Stegun, Handbook of Mathematical Functions, (Dover, New York N.Y., 1965)
- 25) F.O'Brien, PhD Thesis, Boston University
- 26) P.Vogel, At.Data Nucl.Data Tables 14, 599 (1974).
- 27) H.A.Bethe, Phys.Rev. 72, 339 (1947).
- 28) K.T.Cheng, W.-D.Sepp, W.R.Johnson and E.Fricke, Phys.Rev. A17, 489 (1978).
- 29) G.A.Rinker and R.M.Steffen, At.Data Nucl.Data Tables 20, 143 (1977).
- 30) R.Serber, Phys.Rev. 48, 49 (1935).
- 31) E.A.Uehling, Phys.Rev. 48, 55 (1935).
- 32) G.Kallen and A.Sabrey, K. Dan. Vidensk. Selsk. Mat.-Fys. Medd. 29 No 17 (1955)
- 33) L.W.Fullerton and G.A.Rinker Jr., Phys.Rev. A13, 1283 (1976).
- 34) G.A.Rinker Jr. and L.Wilets, Phys.Rev.Lett. 31, 1559 (1973).
- 35) H.Pilkuhn, Relativistic Particle Physics, (Springer, New York N.Y., 1979)
- 36) I.T.Todorov, Properties of Fundamental Interactions, Part C, Vol 2 pg 953., Ed. A.Zichichi, (Editrice Compositori, Bologna, 1973)
- 37) G.Breit, Phys.Rev. 51, 248 (1937).
- 38) H.Grotch and D.R.Yennie, Rev.Mod.Phys. 41, 350 (1969).
- 39) J.L.Friar and J.W.Negele, Phys.Lett. B46, 5 (1973).
- 40) R.C.Barrett, D.A.Owen, J.Calmot and H.Grotch, Phys.Lett. B47, 297 (1973).
- 41) F.Gross, Phys.Rev. 186, 1448 (1969).
- 42) E.E.Salpeter, Phys.Rev. 87, 328 (1952).

- 43) T.Fulton and P.C.Martin, Phys.Rev. 25, 811 (1954).
- 44) T.E.O.Ericson and J.Hufner, Nucl.Phys. B47 205 (1972).
- 45) G.A.Rinker, Phys.Rev. A14, 18 (1976).
- 46) G.A.Rinker and J.Spath, Nucl.Phys. A306, 360 (1978).
- 47) P.Vogel and V.R.Akylas, Nucl.Phys. A276, 466 (1977).
- 48) G.A.Rinker and J.Spath, Nucl.Phys. A306, 397 (1978).
- 49) M.Chen, Phys.Rev. C1, 1167 (1970).
- 50) M.Chen, Phys.Rev. C1, 1176 (1970).
- 51) J.D.Jackson, Classical Electrodynamics, (Wiley, New York N.Y., 1975)
- 52) E.U.Condon and G.H.Shortly, The Theory of Atomic Spectra, (Cambridge, London, 1951)
- 53) Z.Fried and A.D.Martin, Nuovo Cim. 29, 574 (1963).
- 54) Gordon, Ann. der Phys. 2, 927 (1926).
- 55) R.A.Ferrell, Phys.Rev.Lett. 4, 425 (1960).
- 56) M.Leon and R.Seki, Nucl.Phys. A282, 445 (1977).
- 57) E.Storm and H.I.Israel, At.Data Nucl.Data Tables A7, 565 (1970).
- 58) E.Fermi and E.Teller, Phys.Rev. 72, 399 (1947).
- 59) C.E.Wiegand and G.L.Godfrey, Phys.Rev. A9, 2282 (1974).
- 60) M.Leon and J.B.Miller, Nucl.Phys. A282, 461 (1977).
- 61) C.J.Batty, Nucl.Phys. A372, 418 (1981).
- 62) C.J.Batty, Nucl.Phys. A372, 433 (1981).
- 63) T.E.O.Ericson and F.Scheck, Nucl.Phys. B19, 450 (1970).
- 64) A.Doloff and J.Law, Phys.Rev. C10, 1688 (1974).
- 65) M.Krell, Phys.Rev.Lett. 26, 584 (1971).
- 66) R.Seki, Phys.Rev. C5, 1196 (1972).
- 67) G.Backenstoss et. al., Phys.Lett. 38B, 181 (1972).

- 68) B.R.Martin and M.Sakitt, *Phys.Rev.* 183, 1345 (1969).
- 69) B.R.Martin and M.Sakitt, *Phys.Rev.* 183, 1352 (1969).
- 70) W.A.Bardeen and E.W.Torigoe, *Phys.Rev.* C3, 1785 (1971).
- 71) W.A.Bardeen and E.W.Torigoe, *Phys.Lett.* 38B, 135 (1972).
- 72) A.Daloff, *Phys.Rev.* C21, 1516 (1980).
- 73) K.M.Watson, *Phys.Rev.* 89, 575 (1953).
- 74) R.Brockmann and E.Oset, *Phys.Lett.* 118B, 33 (1982).
- 75) D.Zieminska, *Phys.Lett.* 37B, 403 (1971).
- 76) V.Fitch and R.Motley, *Phys.Rev.* 101, 496 (1956).
- 77) Particle Data Group, *Phys.Lett.* 111B (1982).
- 78) Giovannotti *et. al.*, *Phys.Rev.* D29, 343 (1984).
- 79) L.Michel, *Rev.Mod.Phys.* 29, 227 (1957)
- 80) Adrian C. Melissinos, Experiments in Modern Physics, (Academic Press, New York N.Y., 1966)
- 81) F.S.Goulding and D.A.Landis, Lawrence Berkeley Laboratory Report 13862, IEEE Nucl. Sci. Symp., San Francisco (1981).
- 82) R.H.Pehl, N.W.Madden, J.H.Elliott, T.W.Randorf, R.C.Trammel and L.S.Darken Jr., IEEE Nucl. Sci. Symp., Washington D.C. (1978).
- 83) D.A.Landis, C.P.Cork, N.W.Madden and F.S.Goulding, Lawrence Berkeley Laboratory Report 13214 (unpublished).
- 84) IEEE Std. 583
- 85) L.R.Biswell and R.E.Rajala, Los Alamos Report 5144 (1973).
- 86) Table of Isotopes 7'th Ed., C.M.Lederer and V.S.Shirley ed., (John Wiley and Sons, New York, 1978).
- 87) K.Dobertin, PTB Report PTB-Ra-12 (1980).
- 88) J.F.Bartlett, J.R.Biel, D.B.Curtis, R.J.Dosen, T.D.Lagerlund, D.J.Ritchie and L.M.Taff, IEEE Trans. Nucl. Sci. NS-26 (1979).
- 89) Copyright Digital Equipment Corp., RSX-11M V03.1 (1978).

- 90) Philip R. Bevington, Data Reduction and Error Analysis for the Physical Sciences, (McGraw-Hill, New York, 1969).
- 91) T.Aways, Nucl.Instr. and Meth. 174, 237 (1980).
- 92) J.T.Routti and S.G.Pruessin, Nucl.Instr. and Meth. 72, 125 (1969).
- 93) B.L.Roberts, R.A.J.Riddle and G.T.A.Squier, Nucl.Instr. and Meth. 130, 559 (1975).
- 94) J.J.Sakurai, Advanced Quantum Mechanics, (Addison-Wesley, Reading Pa, 1967)
- 95) William J. Hommerie, Statistical Computations on a Digital Computer, (Blaisdell Publishing, Waltham, Massachusetts, 1967)
- 96) S.DeBenedetti, Nuclear Interactions, (Robert E. Krieger Publishing Co., Huntington N.Y., 1974).
- 97) Hubbell, Gimm and Överbó, J.Phys.Chem.Ref.Data 9, 1023 (1980).
- 98) Handbook of Chemistry and Physics 53rd Ed., Robert C. Weast ed., (CRC Press, Clevelandd Ohio, 1972).
- 99) Rolf G. Winter, Quantum Physics, (Faculty Publishing, Davis California, 1986).
- 100) C.J.Datty et.al., Nucl.instr. and Meth. 137, 179 (1976).
- 101) J.Schwinger, Phys.Rev. 74, 1439 (1948), and 75, 651 (1949), and 82, 664 (1951).

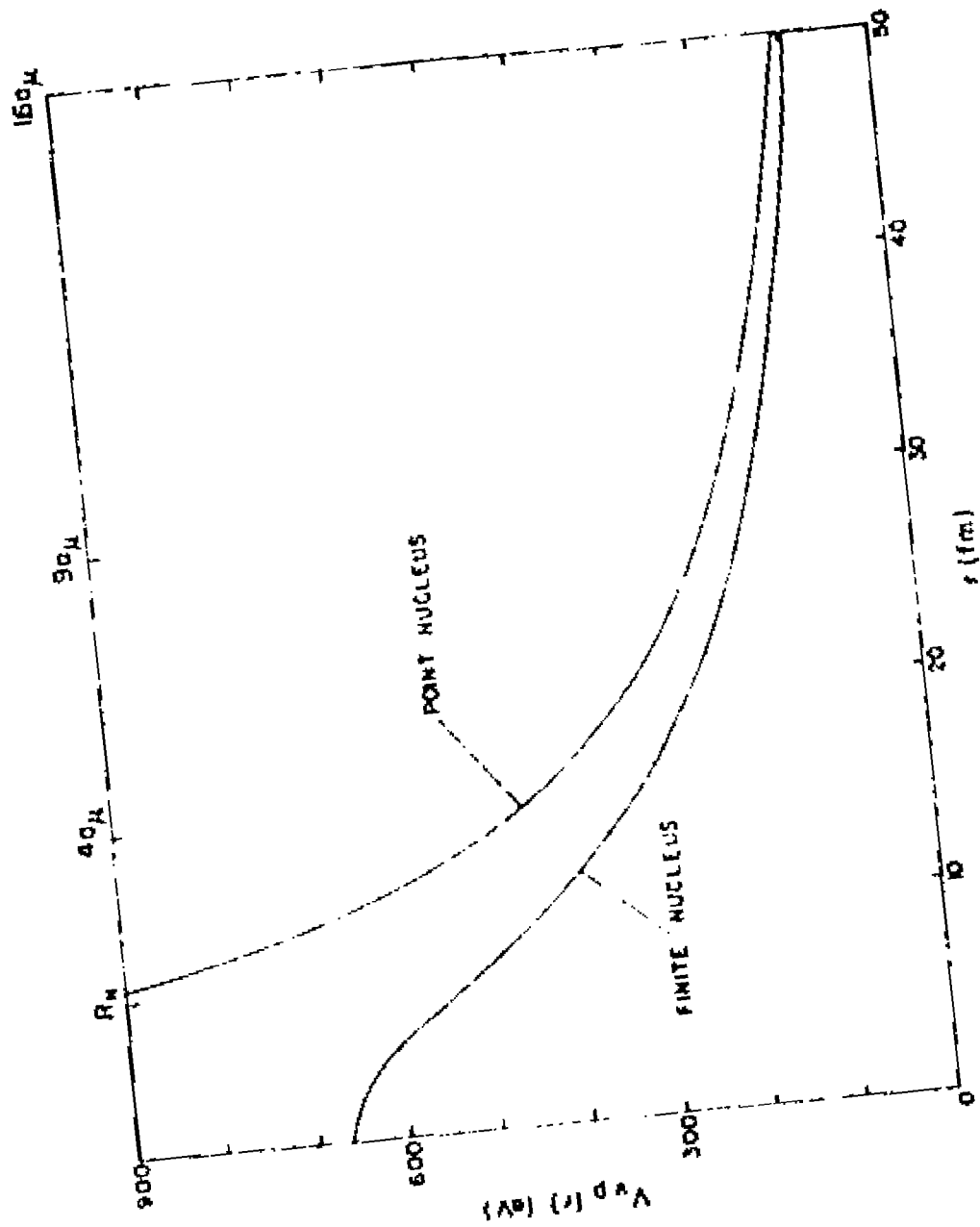


Figure 1

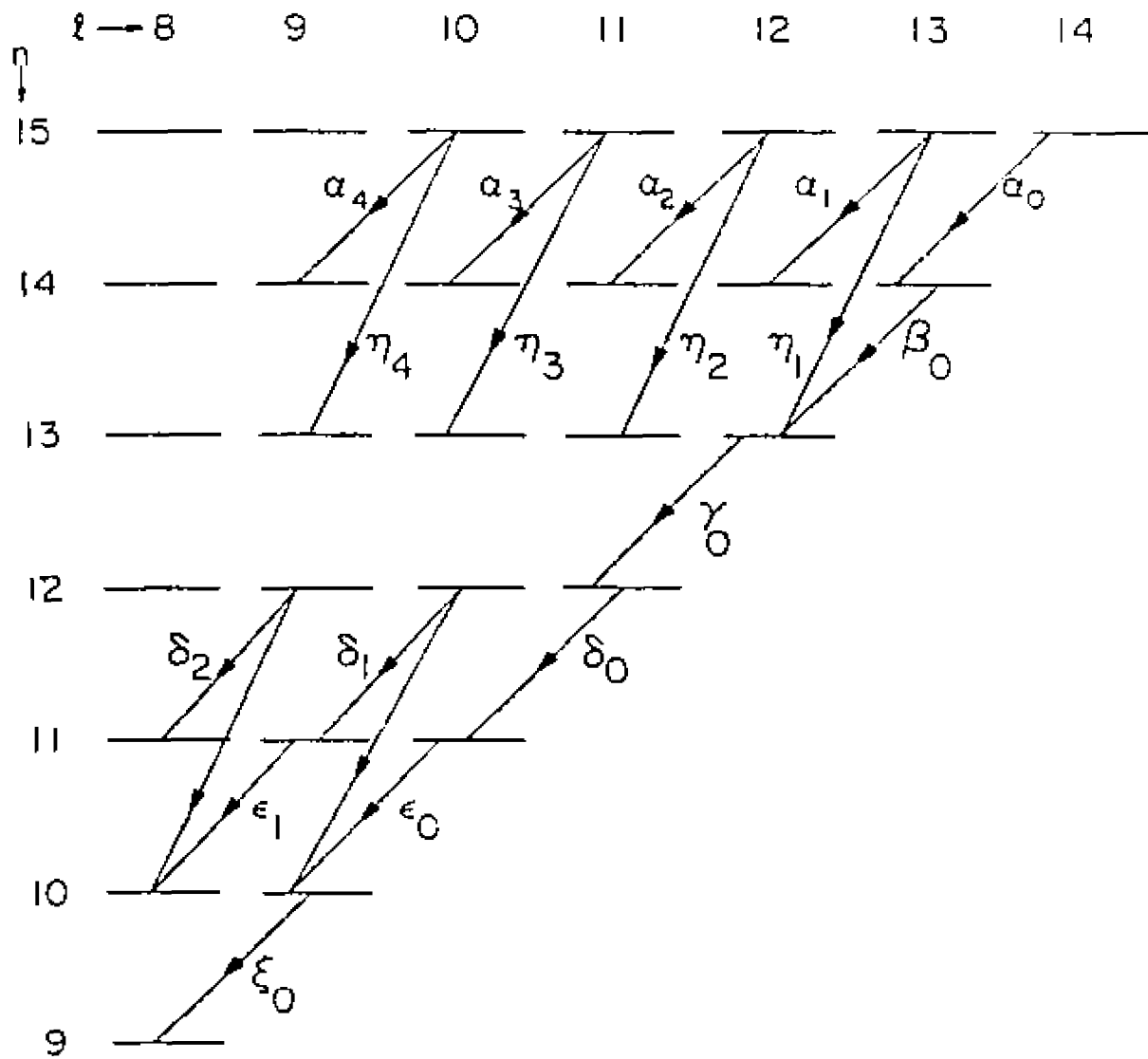


Figure 2

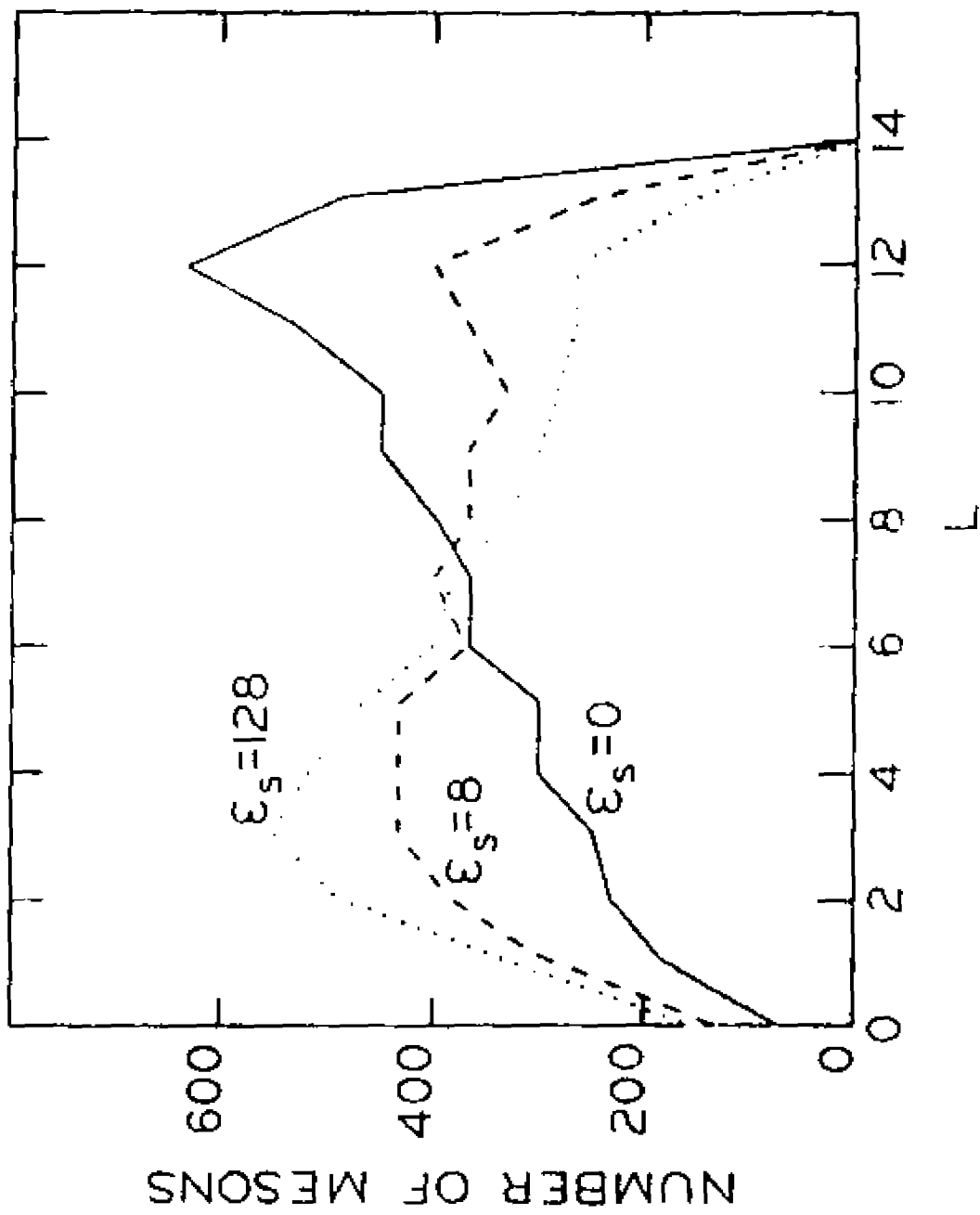


Figure 3

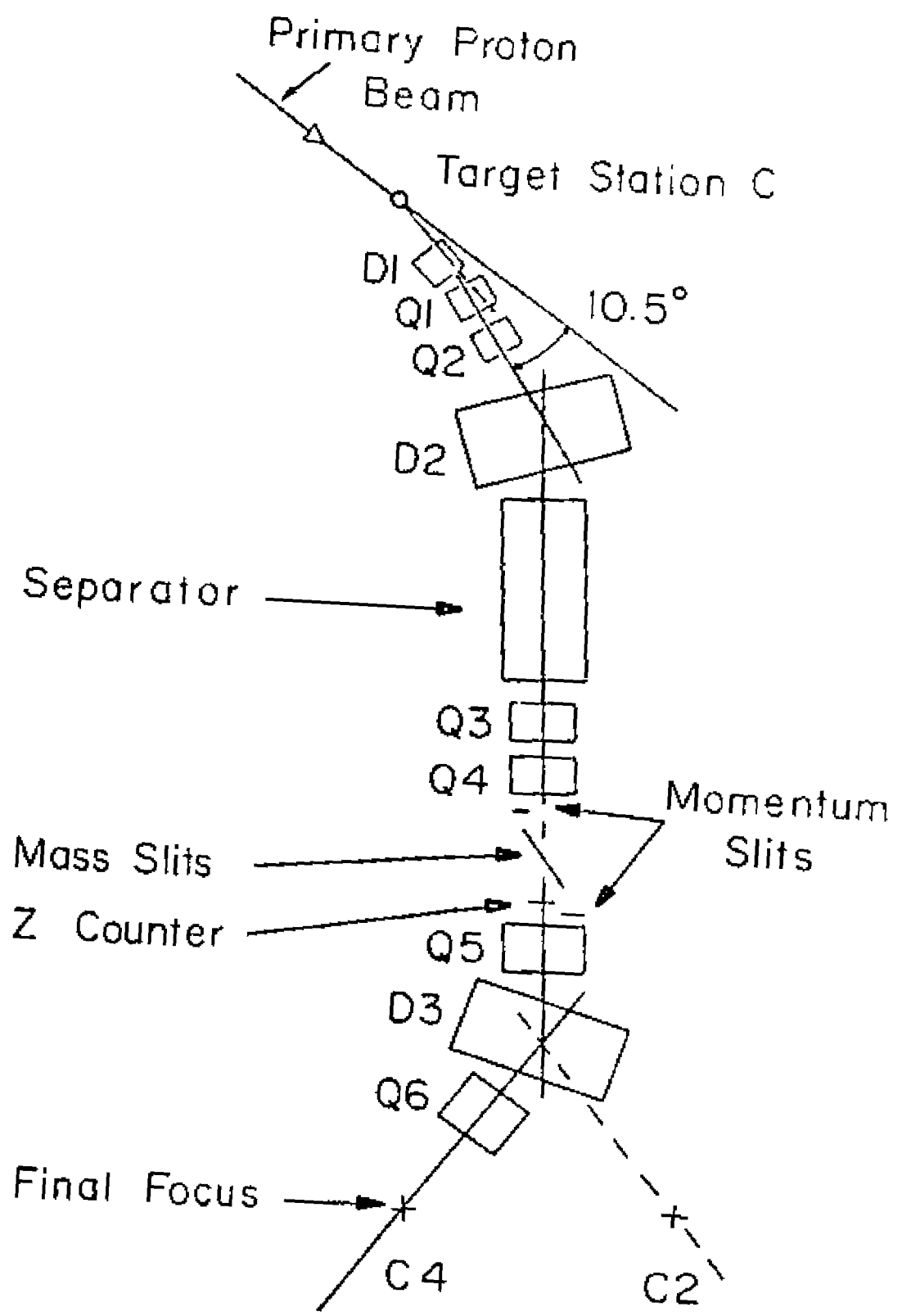


Figure 4

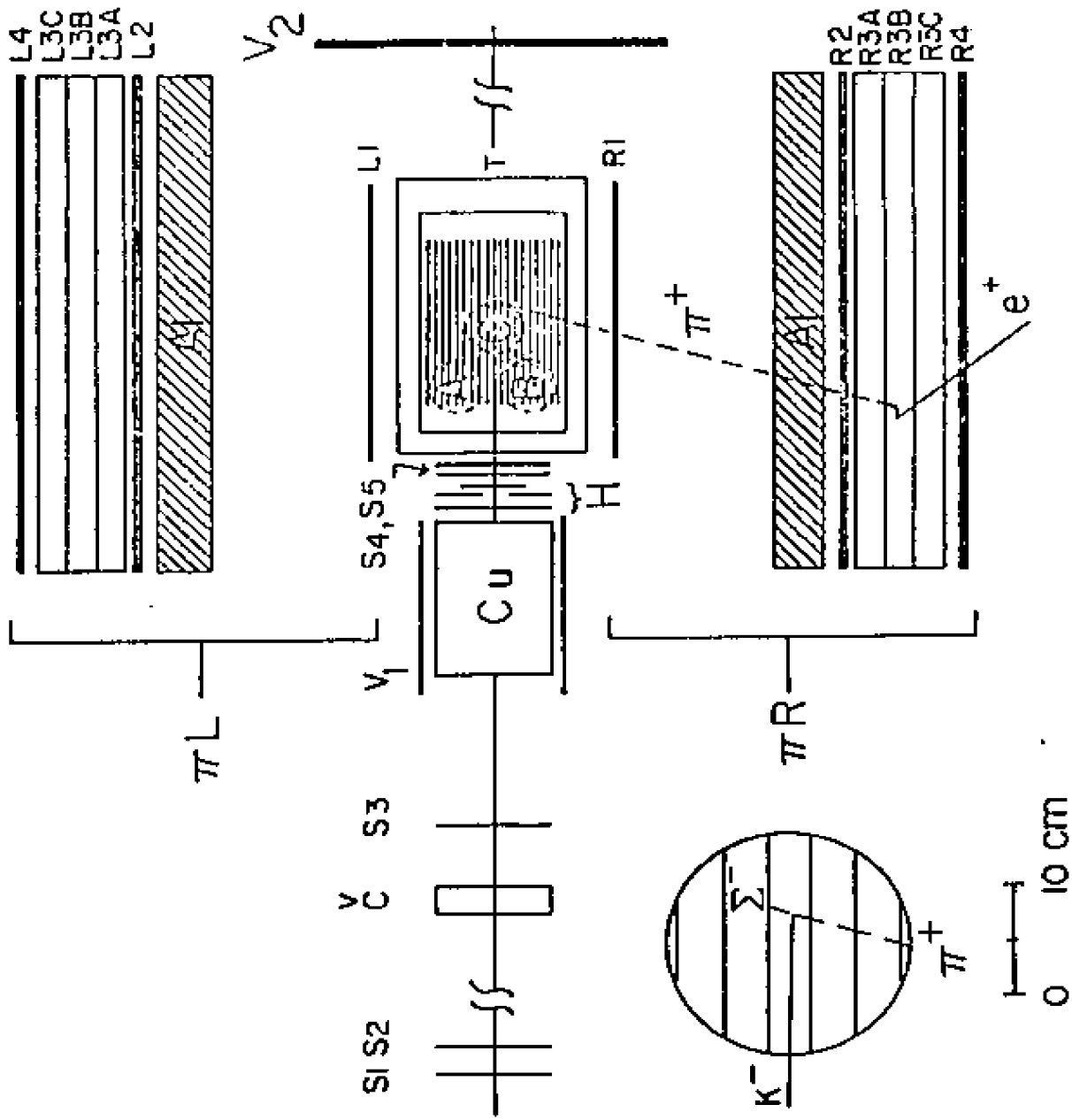


Figure 5

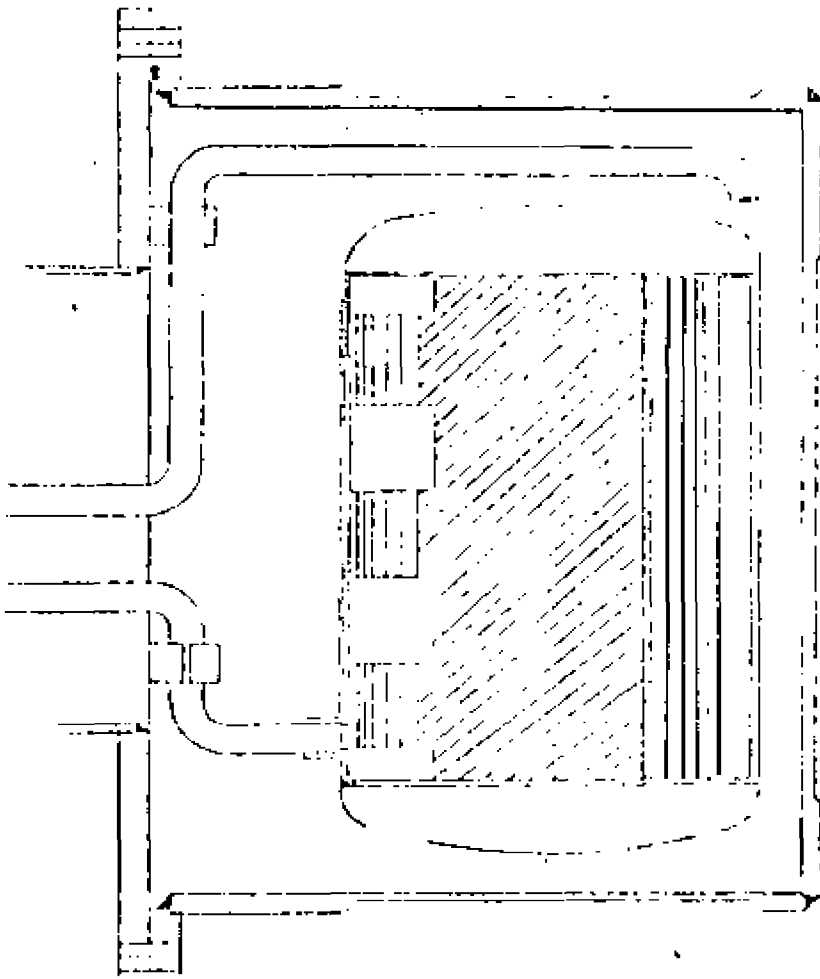
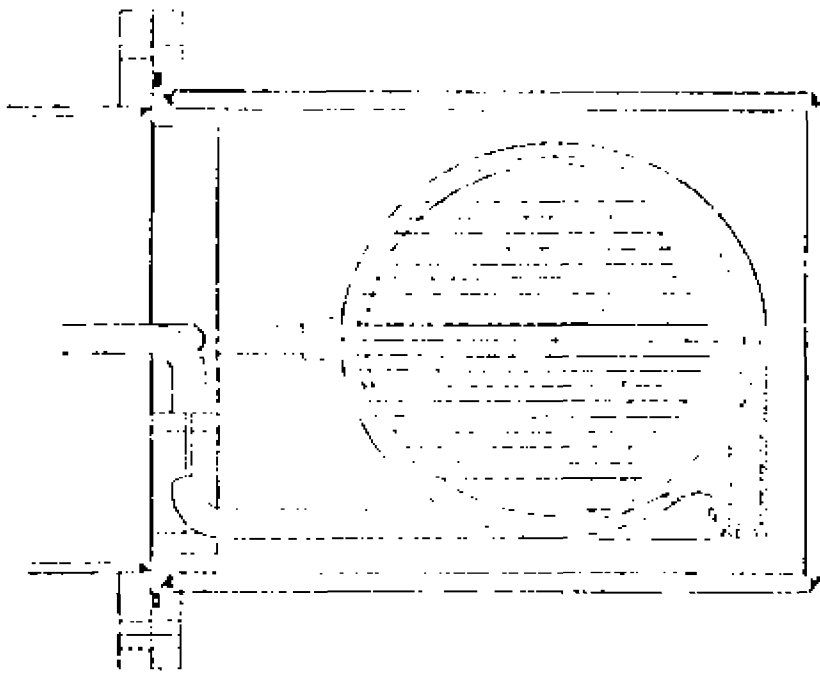


Figure 6

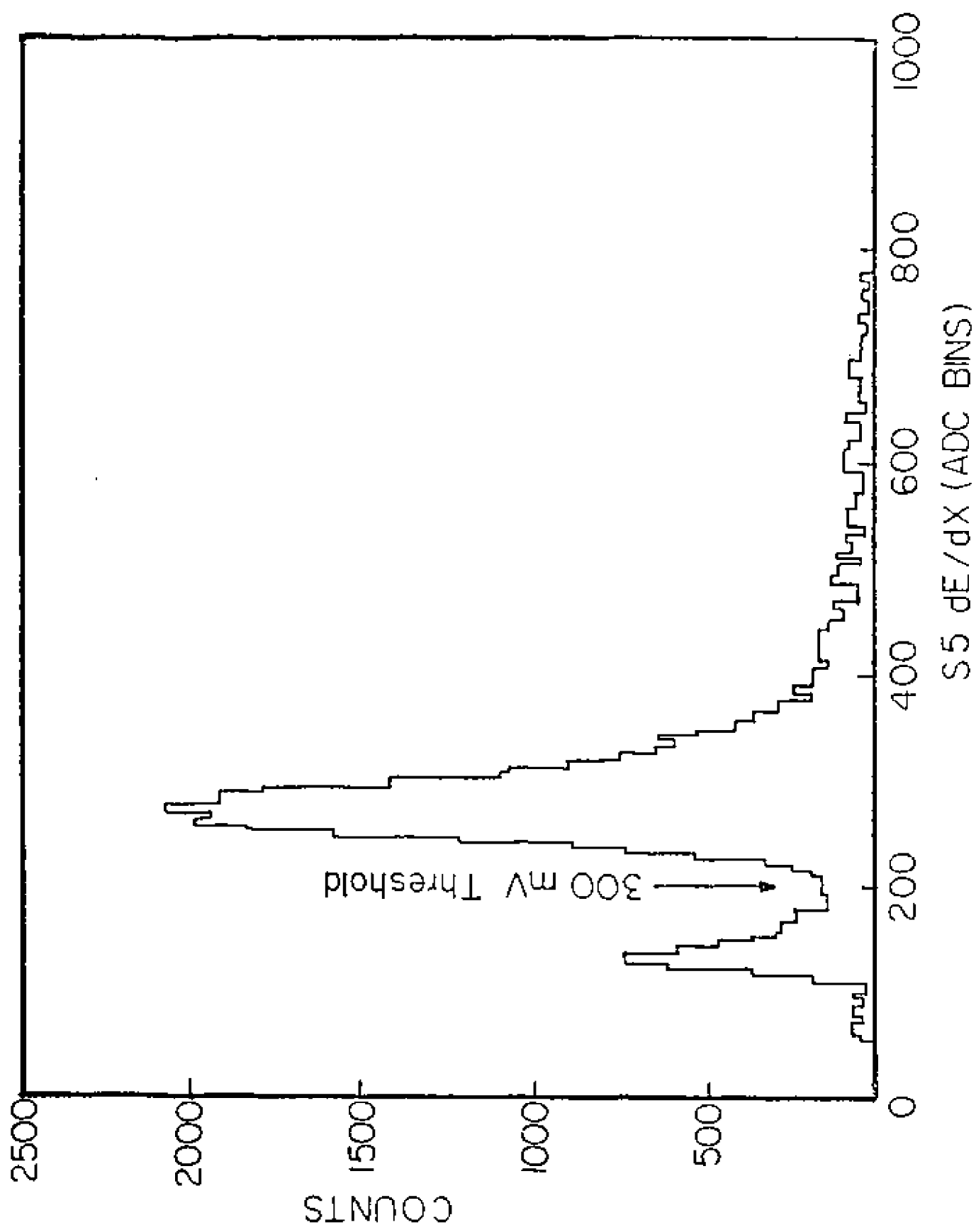


Figure 7

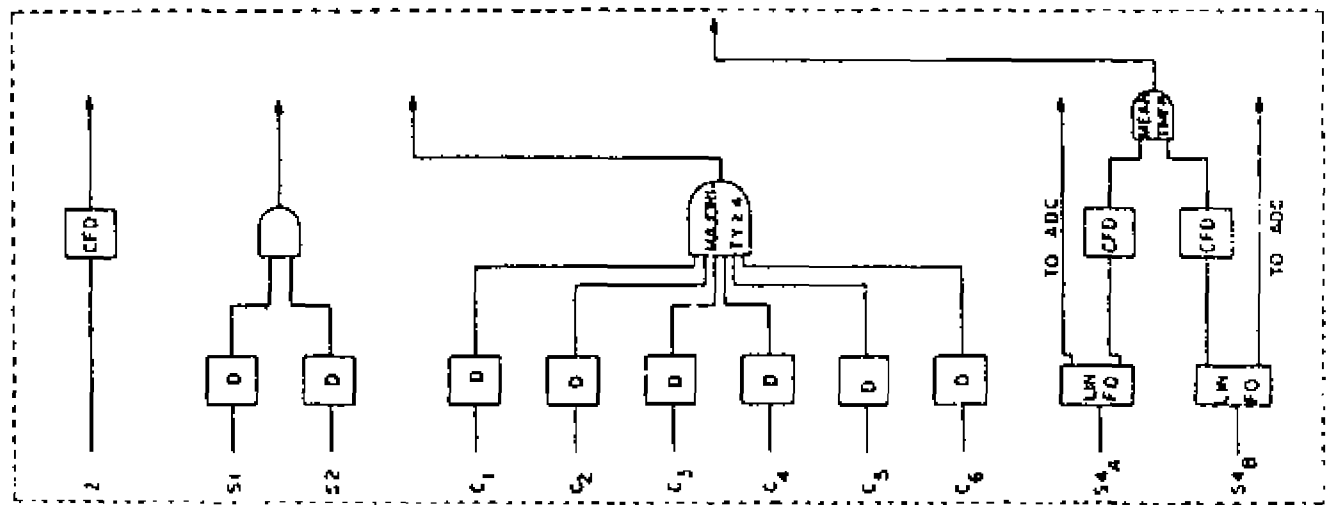
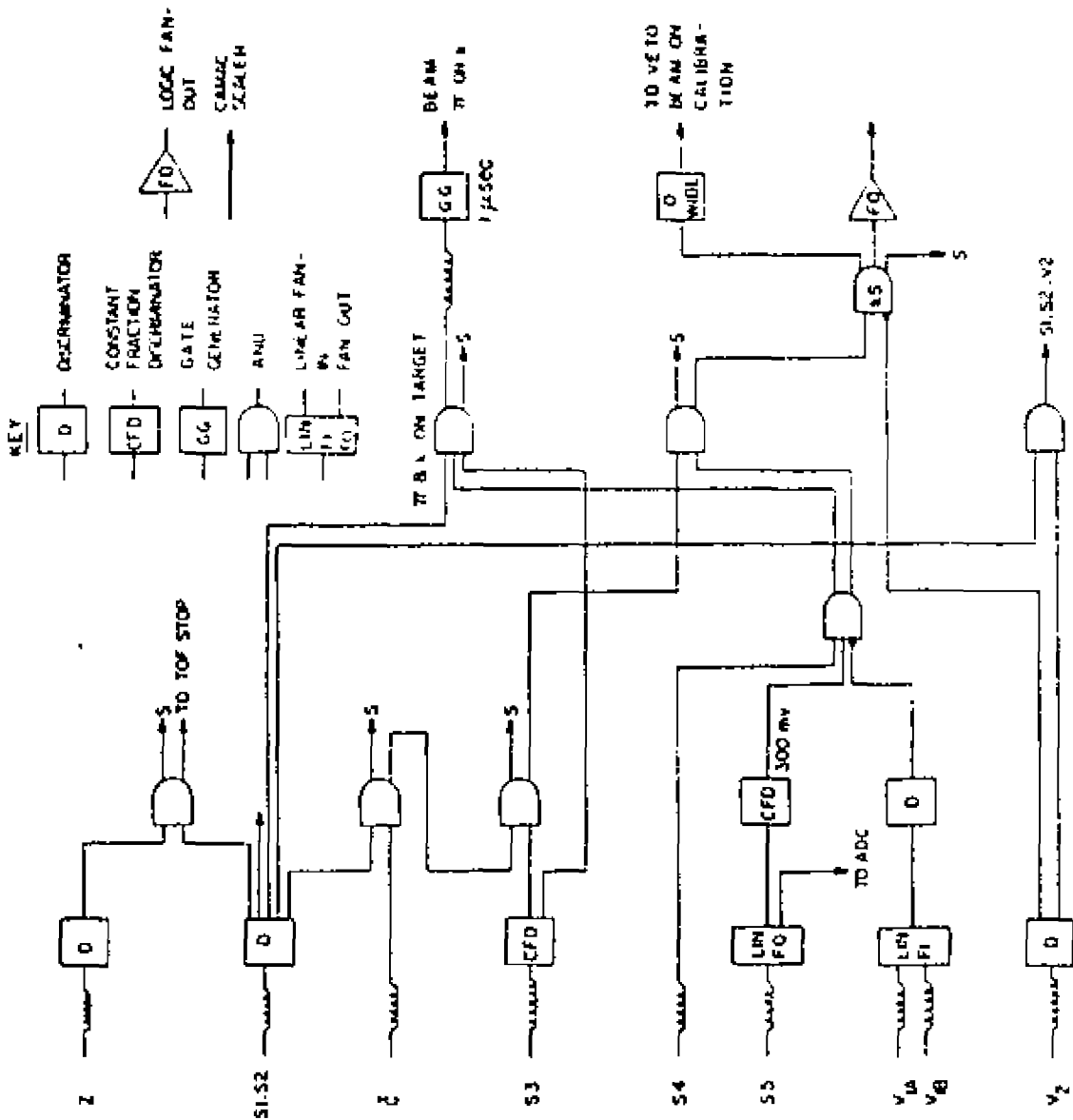


Figure 9

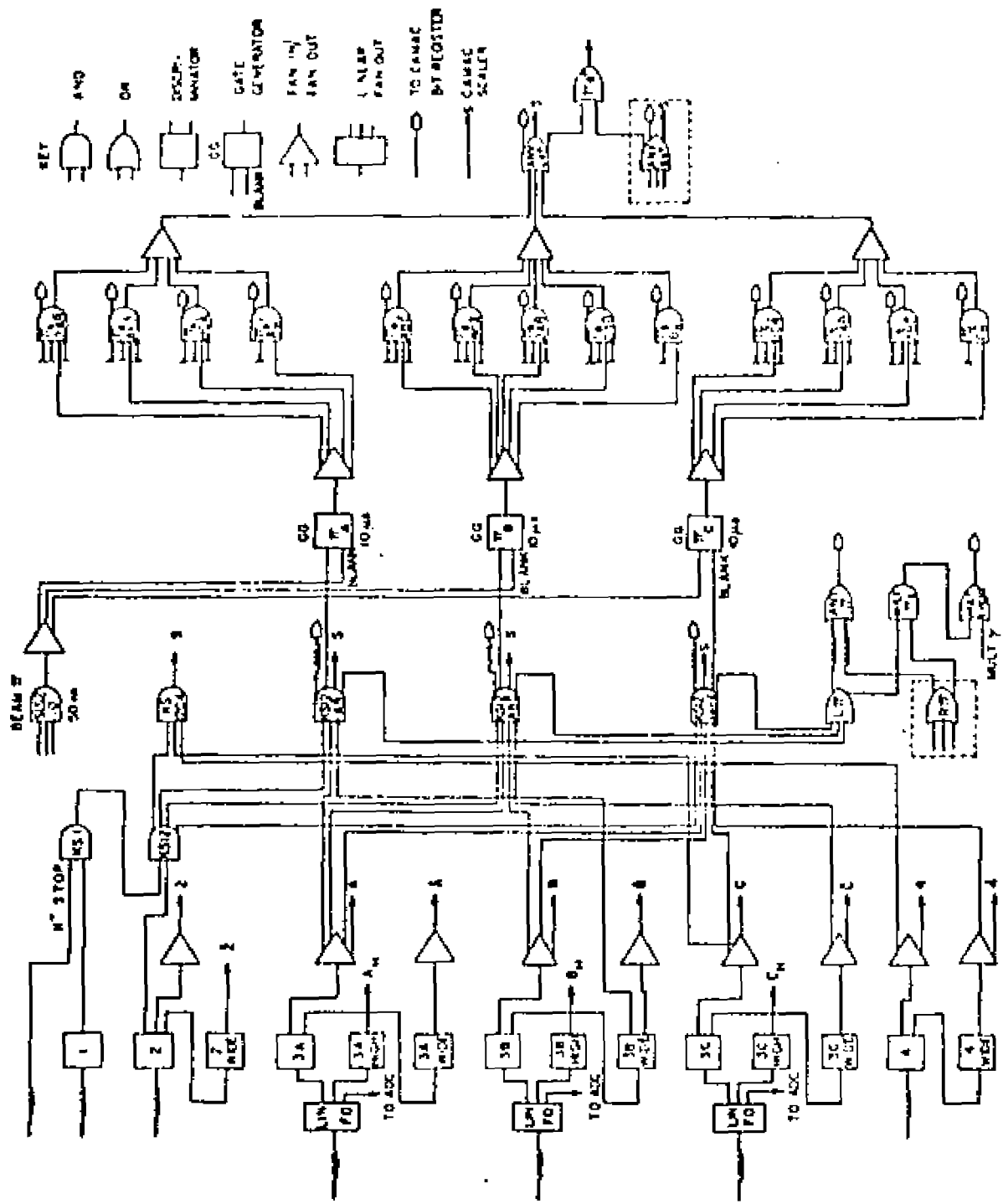


Figure 9

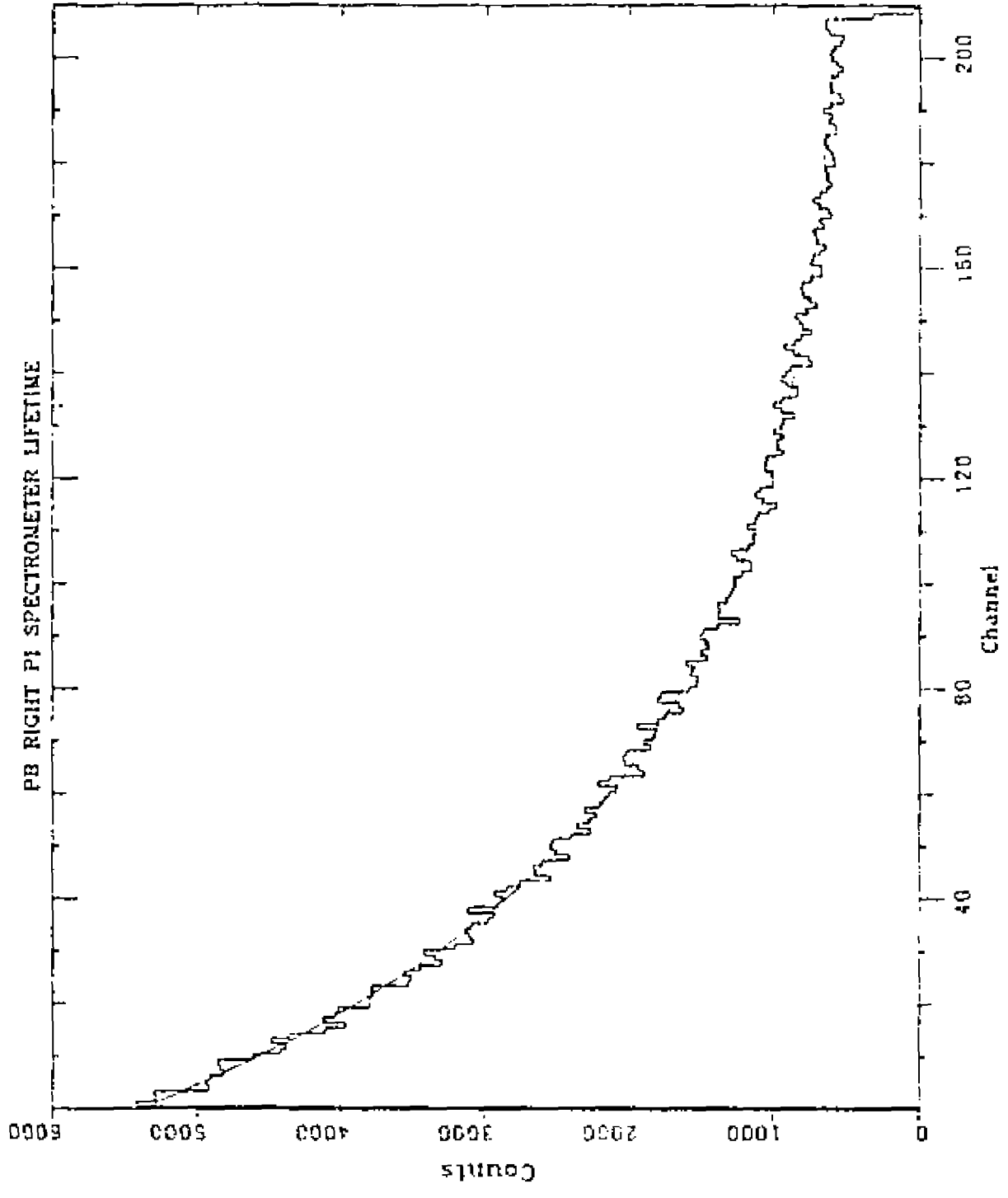


Figure 10

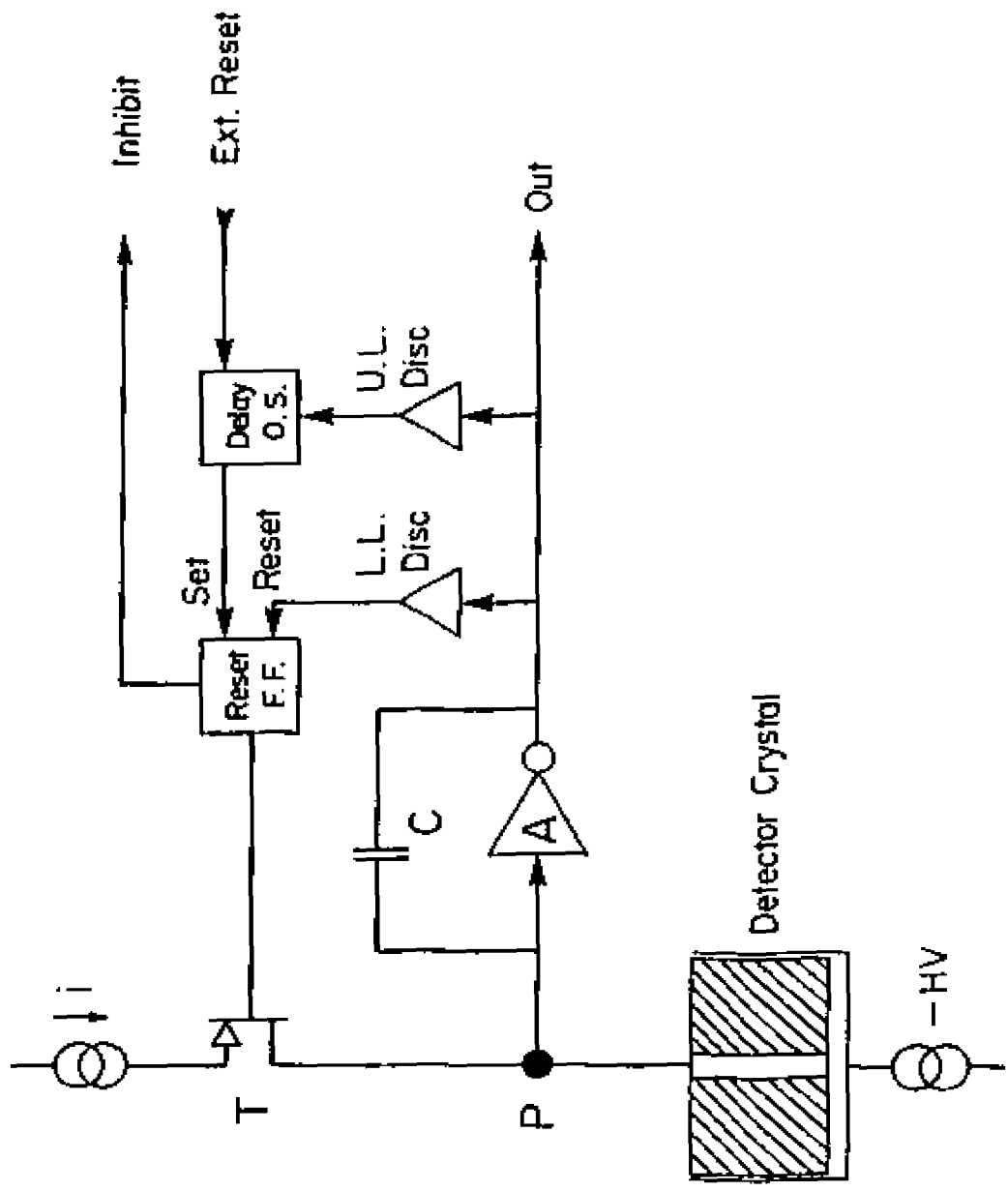


Figure 12

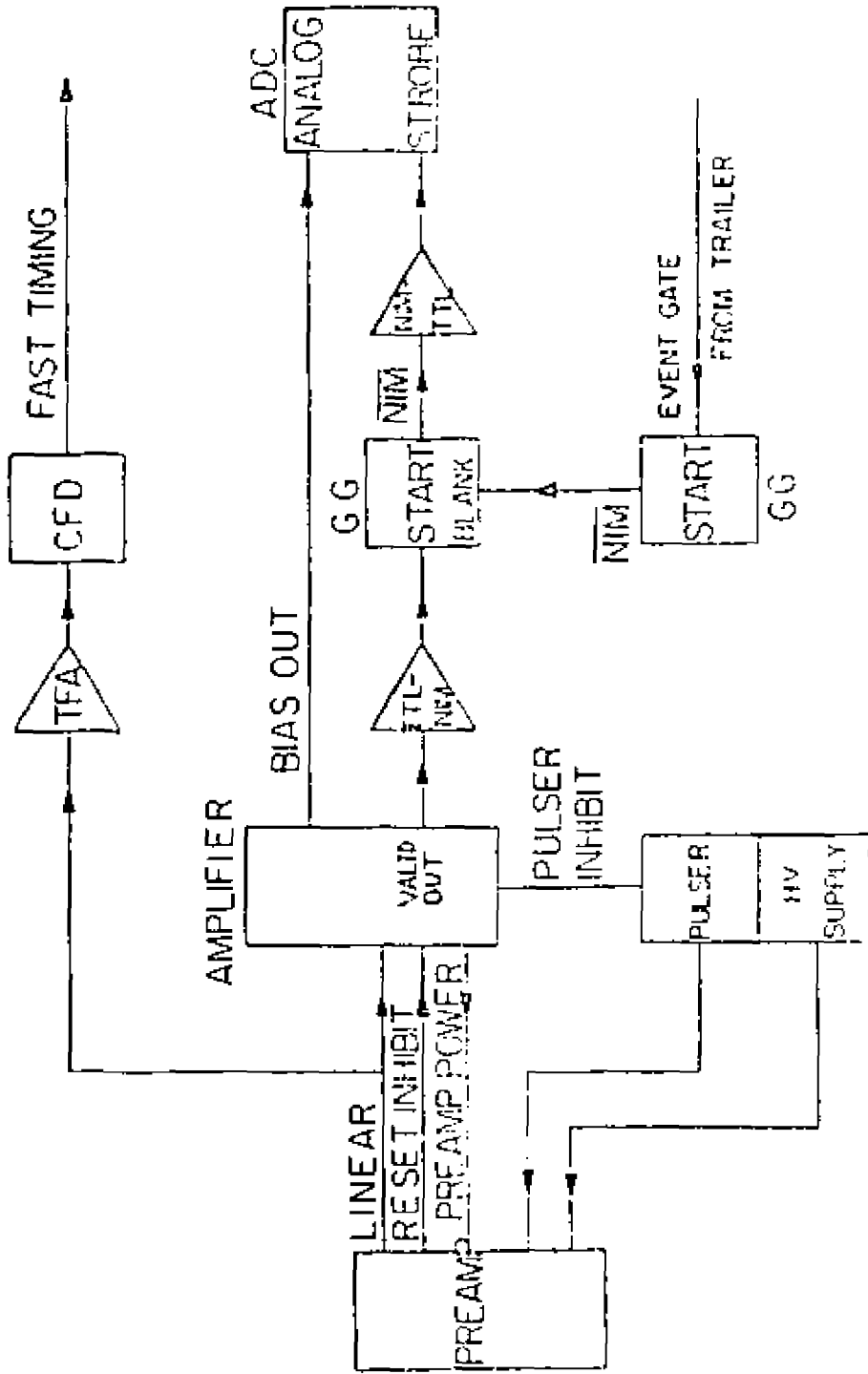


Figure 13

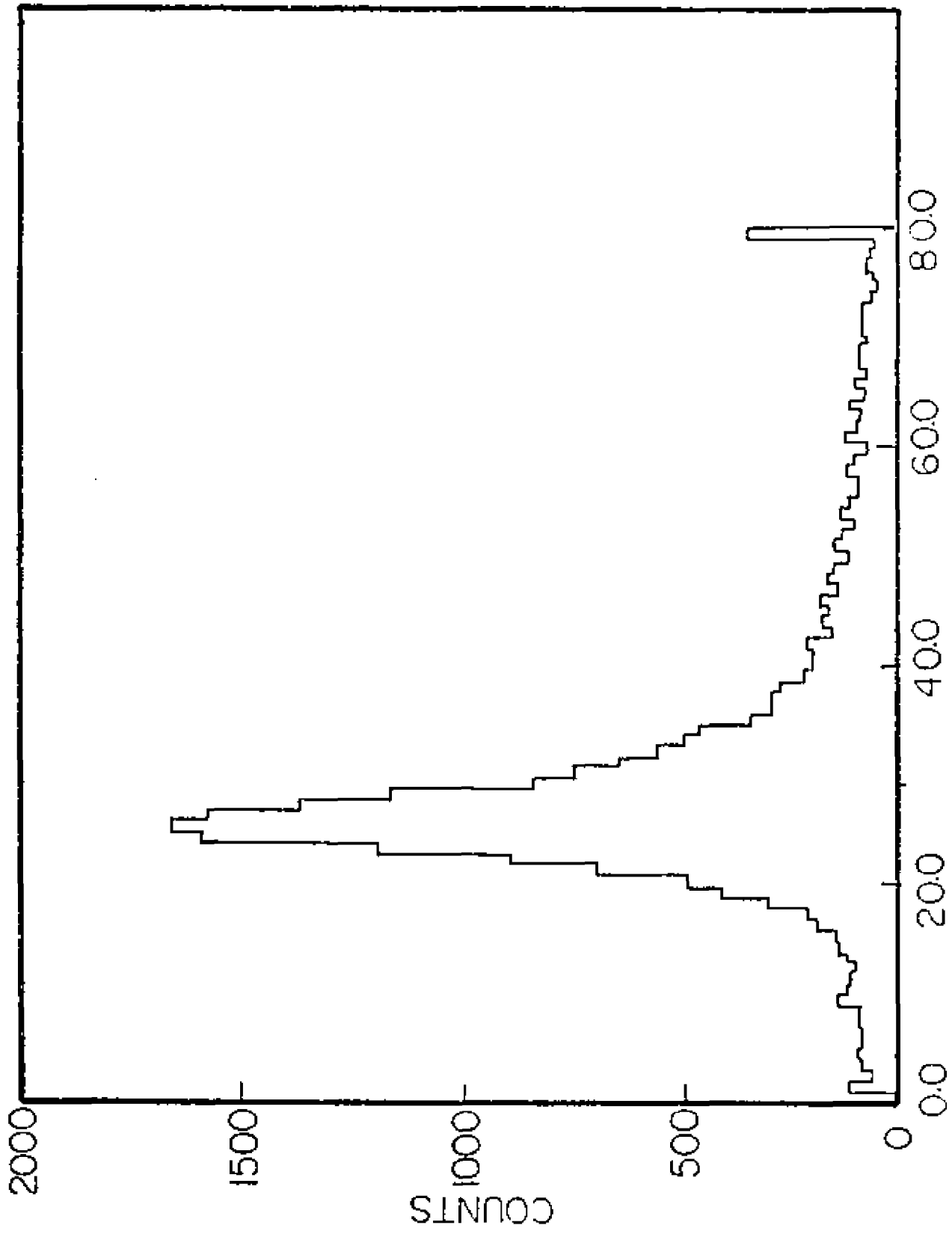


Figure 14

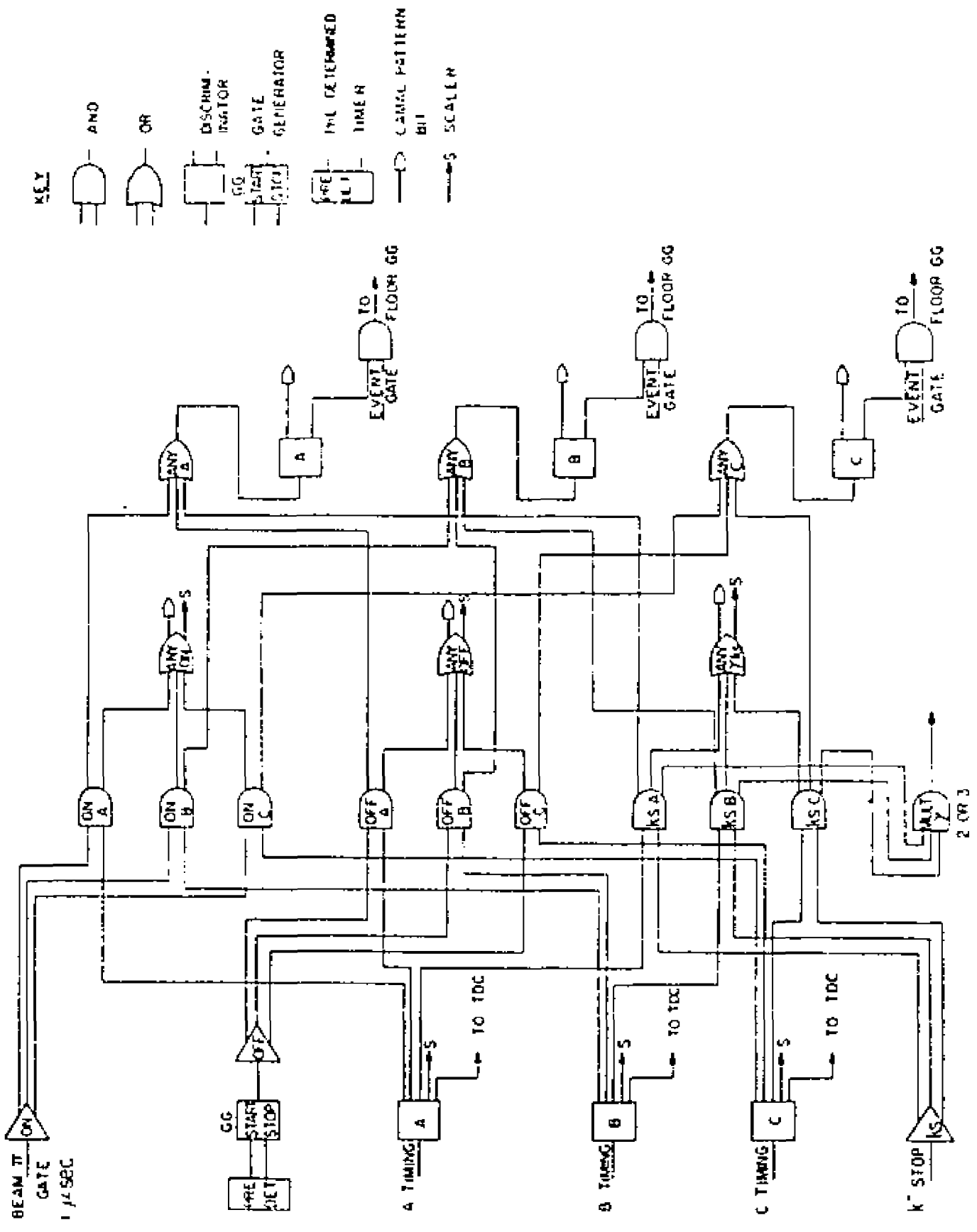


Figure 15

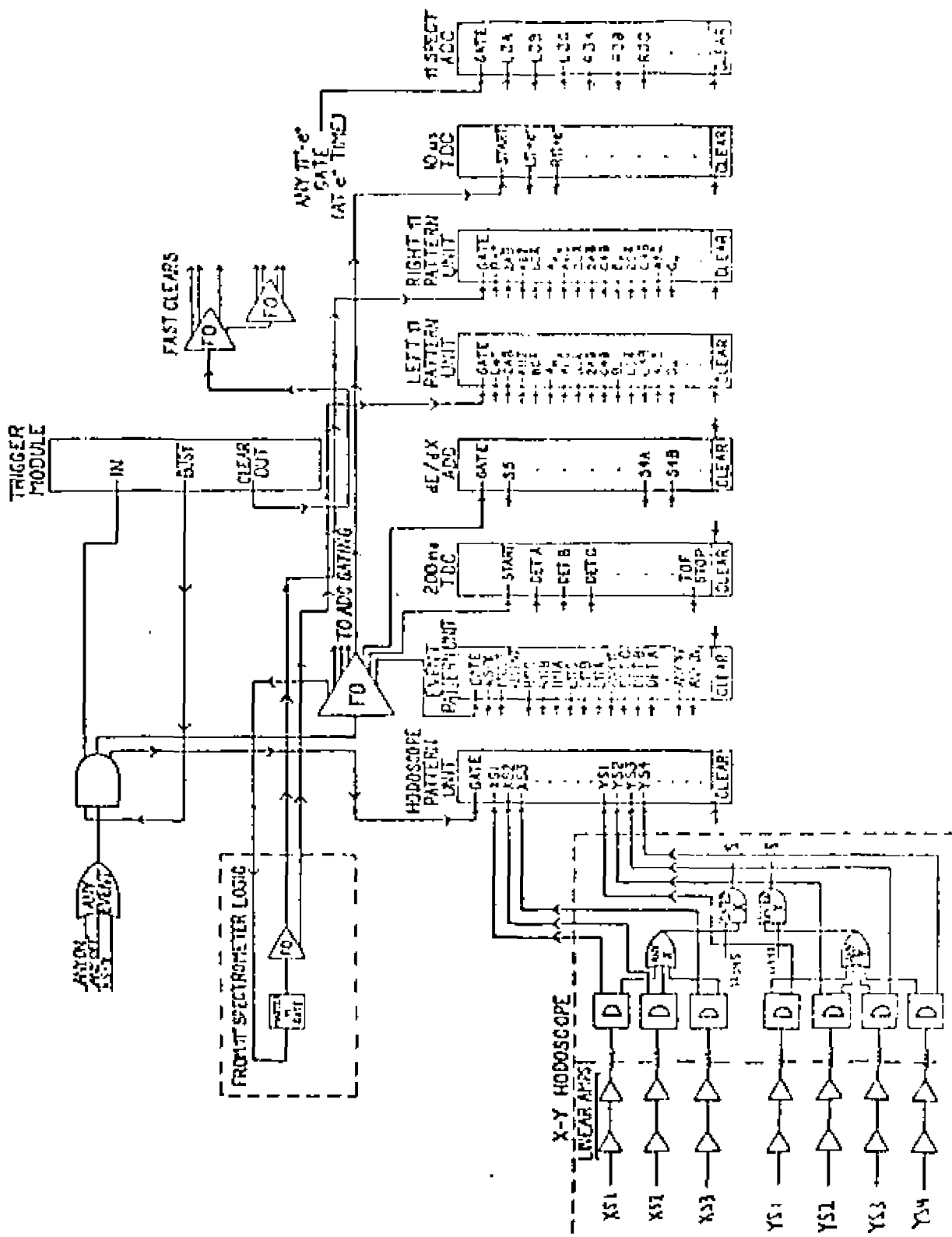


Figure 16

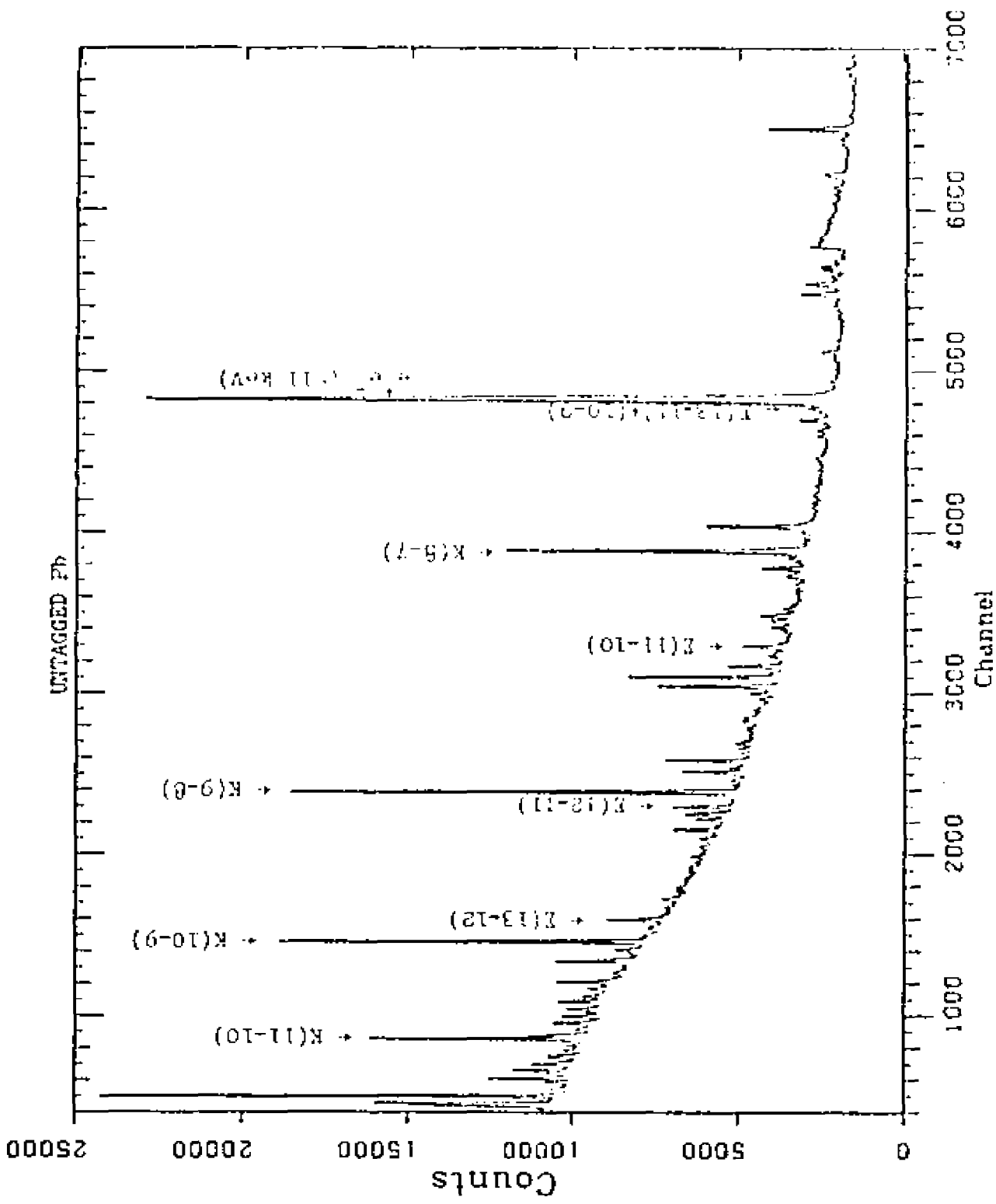


Figure 17

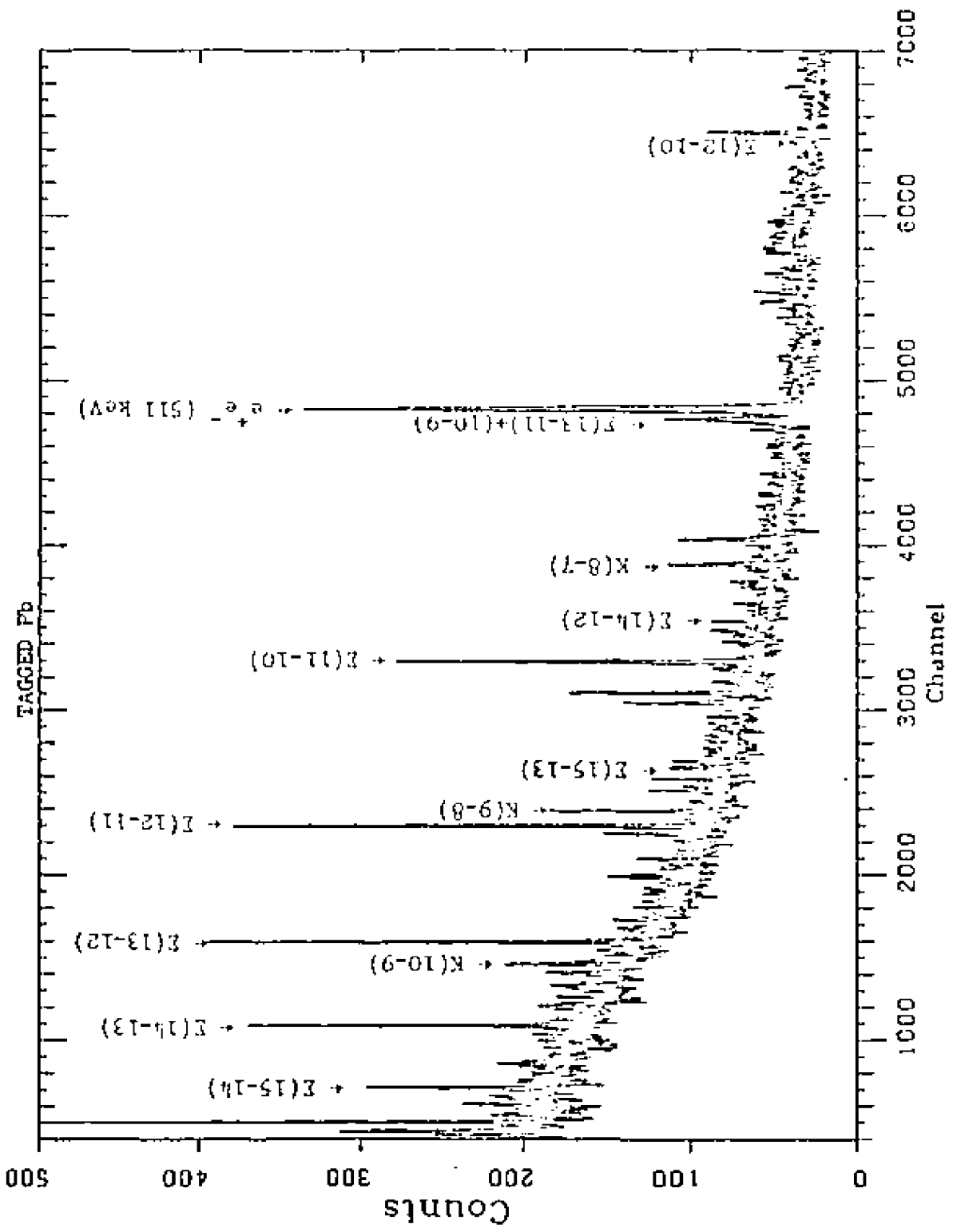


Figure 18

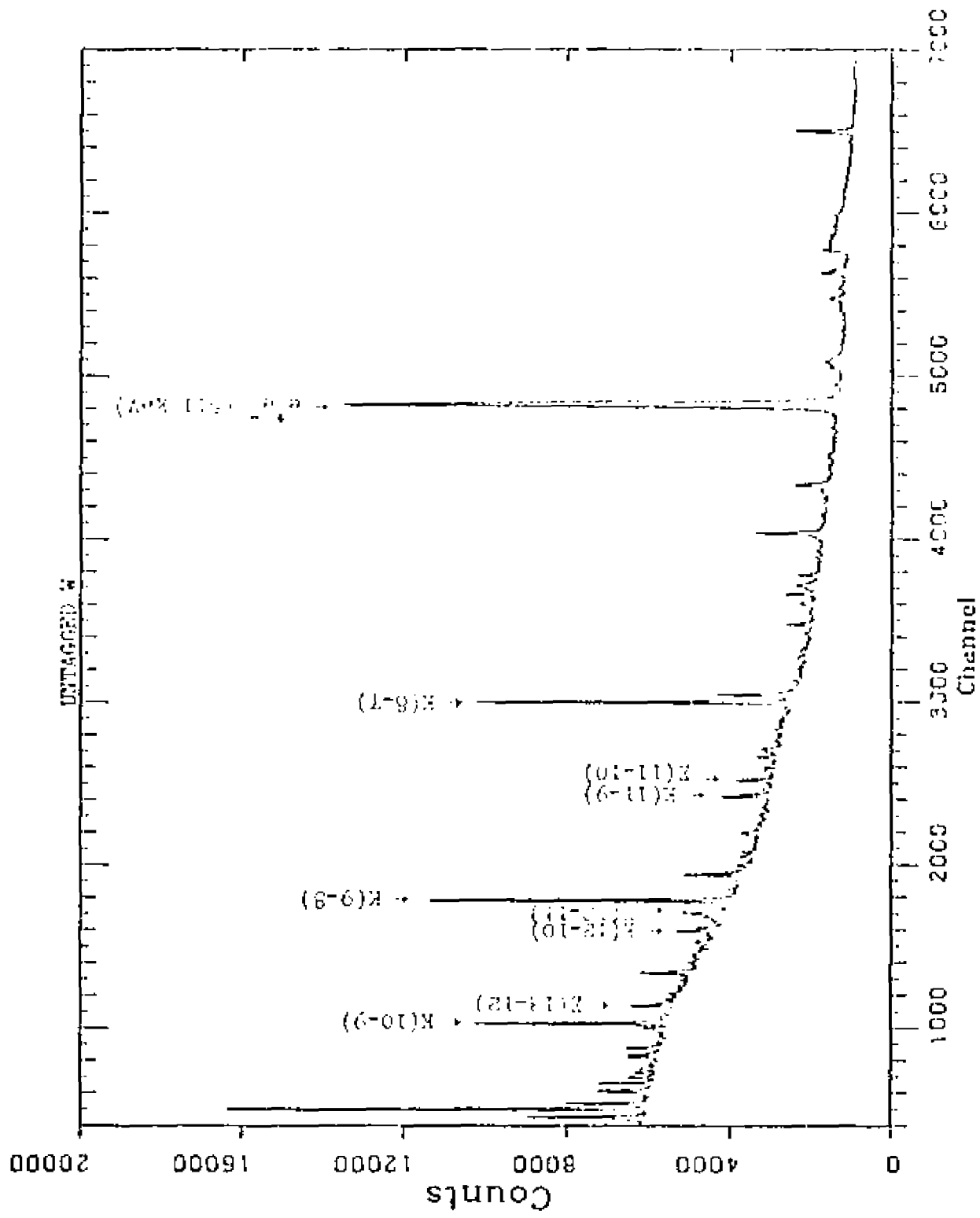


Figure 19

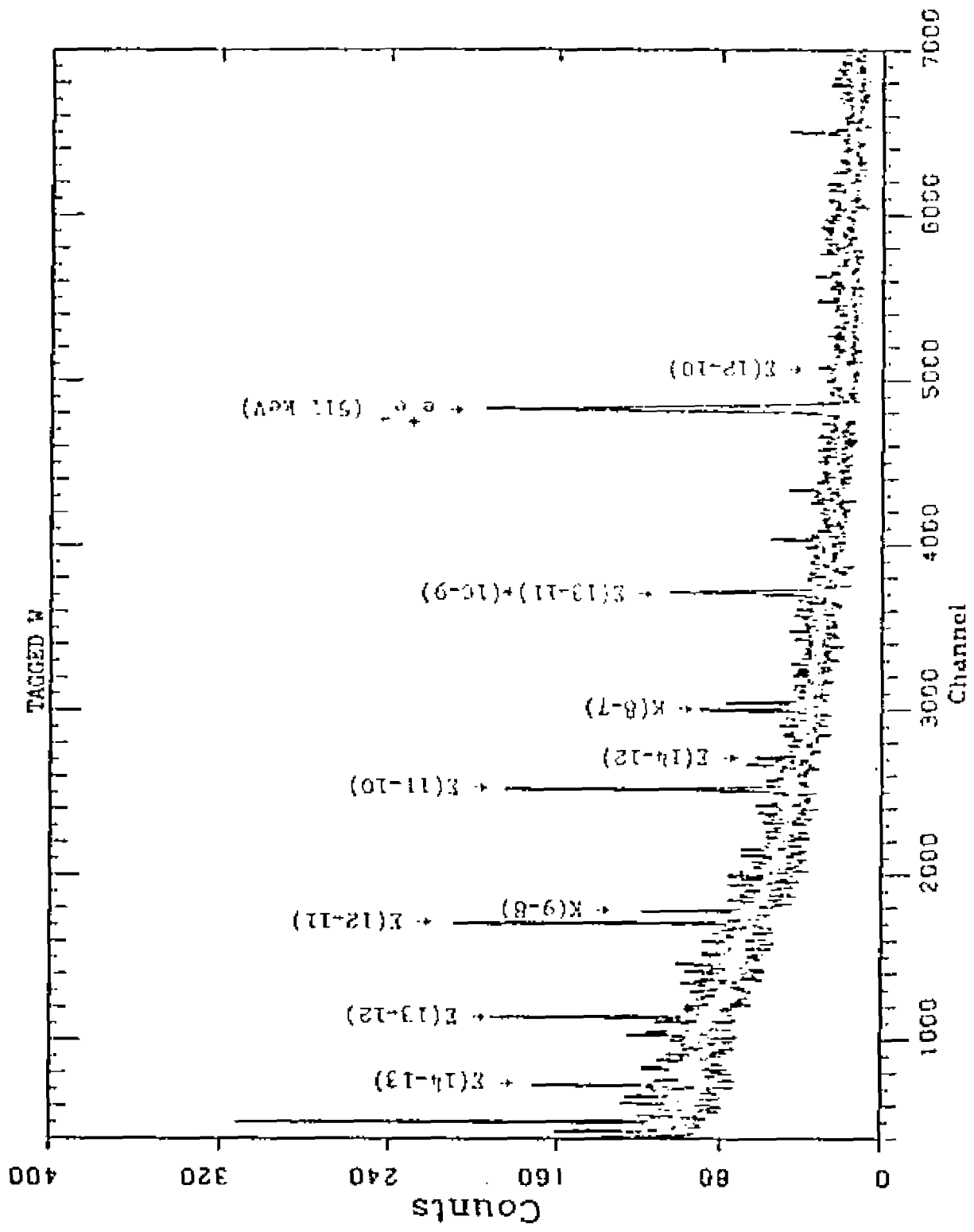


Figure 20

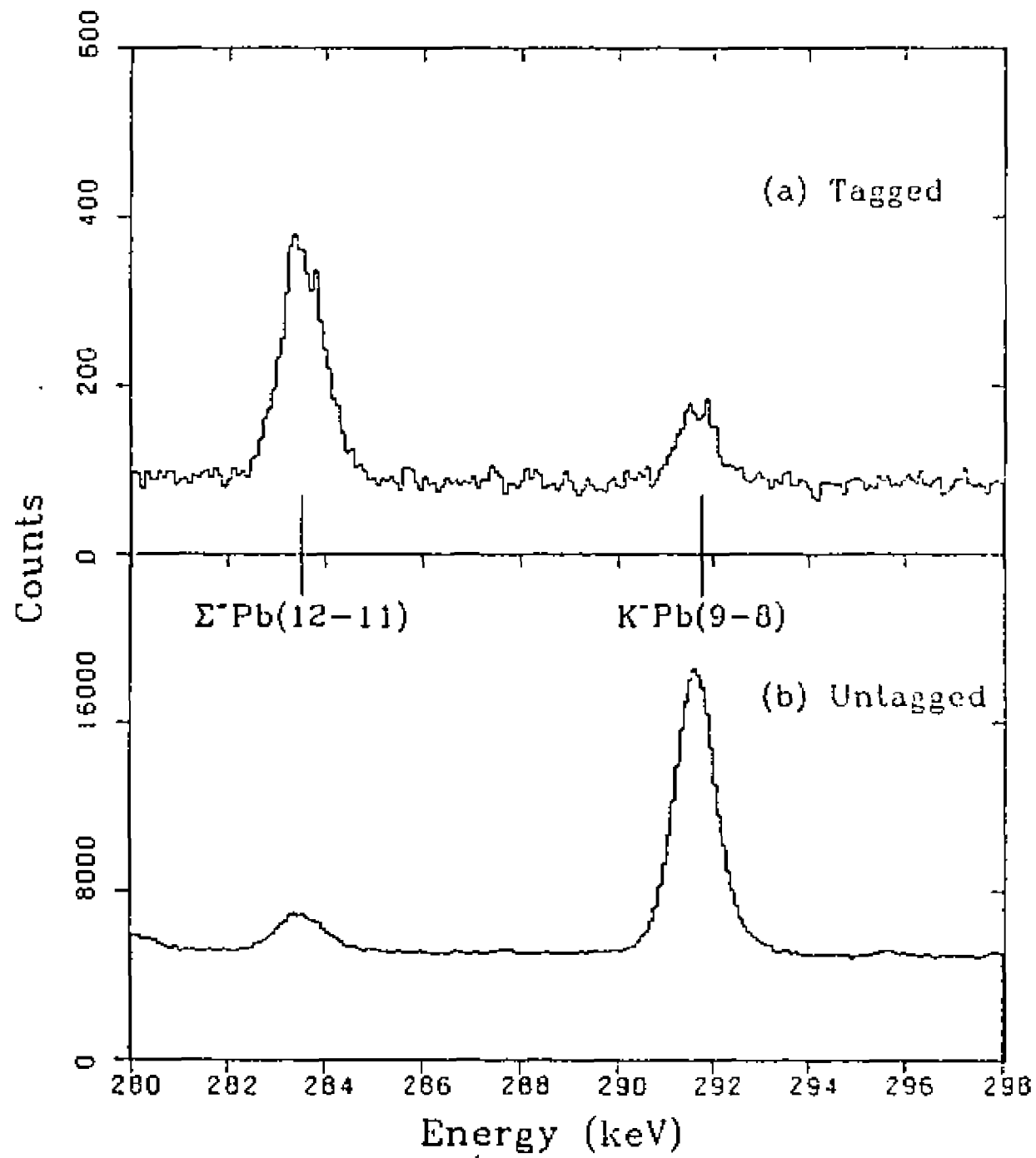


Figure 21

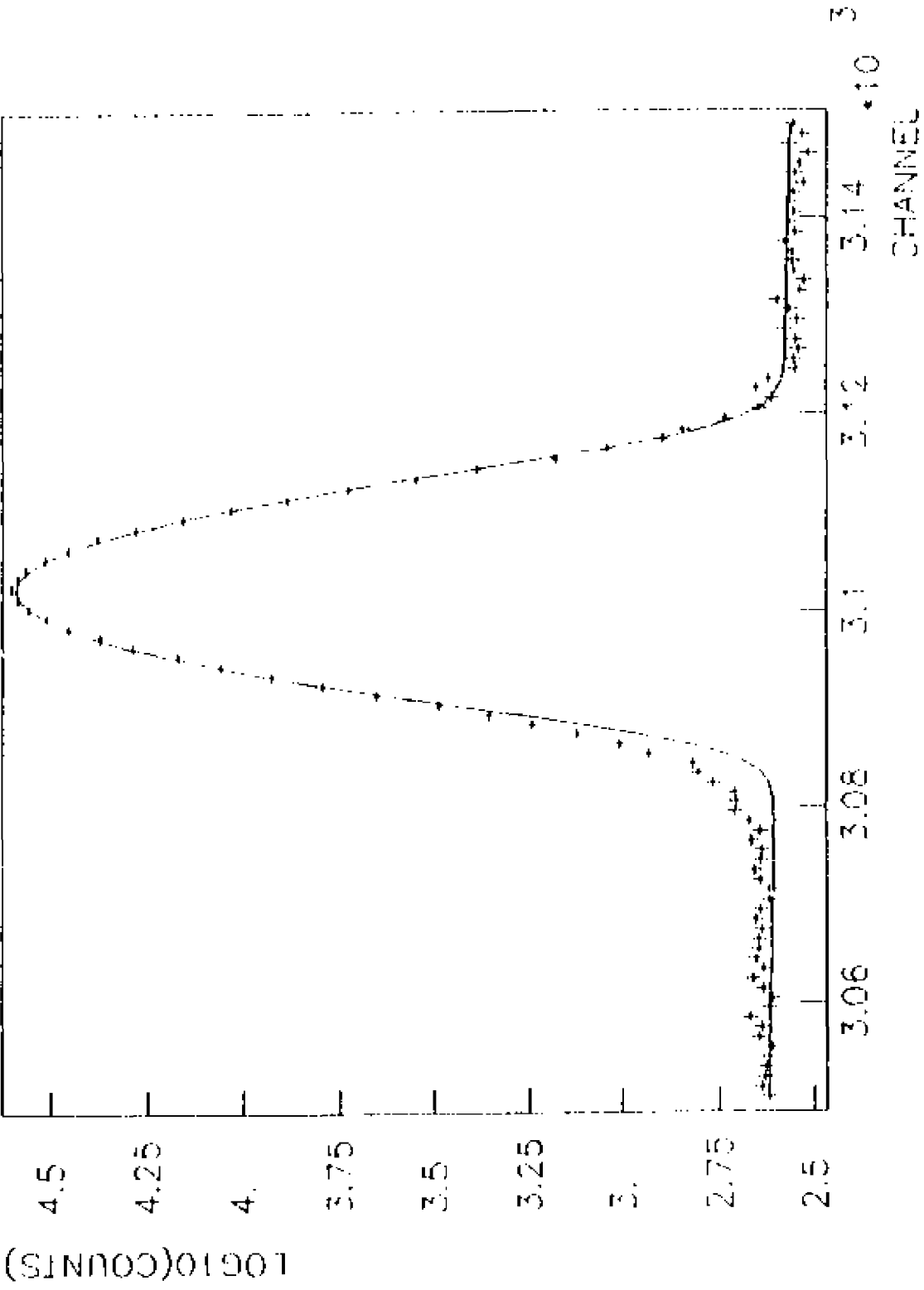


Figure 22

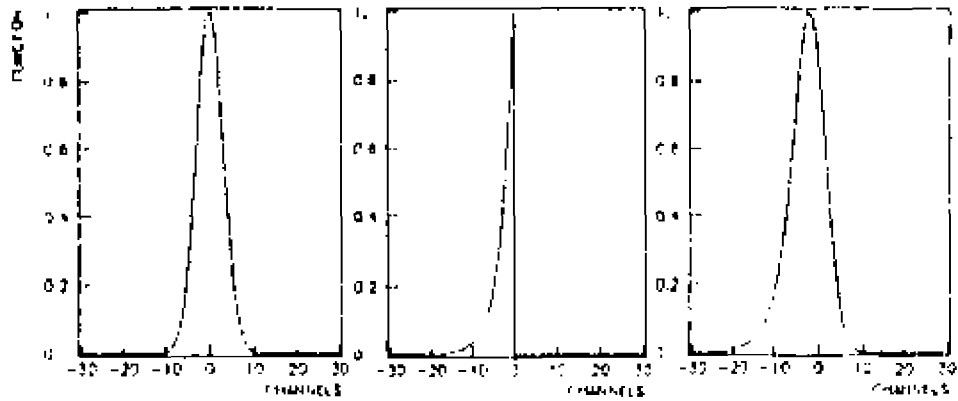


Figure 23-a) $C(O; E_0, \sigma) = V(O; O, \lambda) + R_1(O; E_1, \sigma, \lambda)$

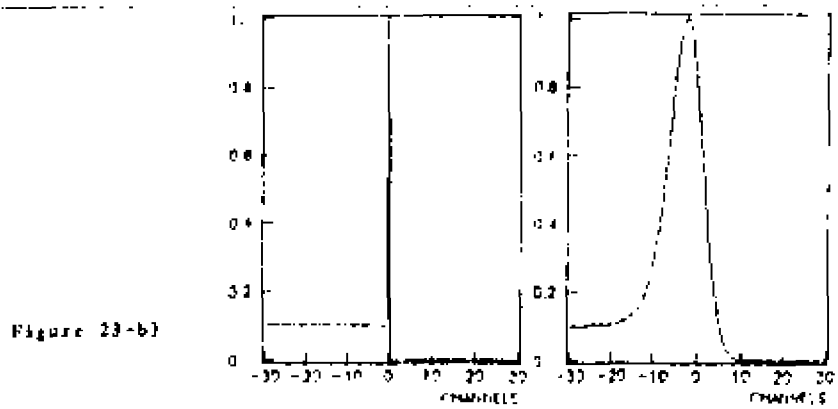


Figure 23-b)

$$R_2(O; E_0, \sigma, \lambda) = I(F_0; E_1, \eta) + R_2(O; E_1, \sigma, \lambda, \eta)$$

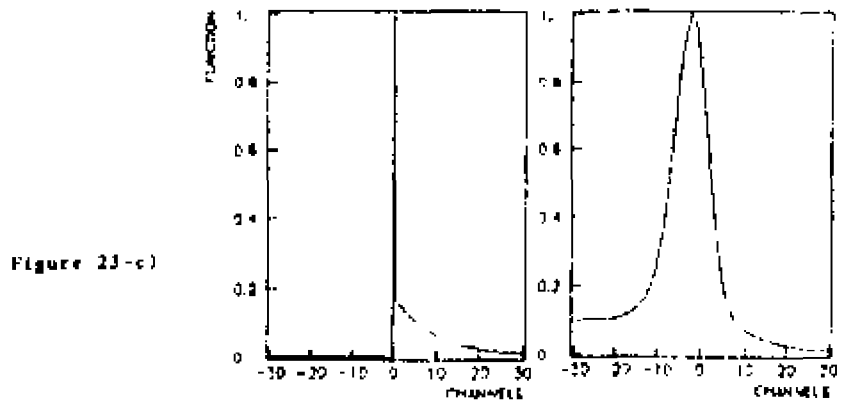


Figure 23-c)

$$P(A; O, q, \gamma) = R_2(O; E_1, \sigma, \lambda, \eta) + R_2(A; E_1, \sigma, \lambda, \eta, q, \gamma)$$

Figure 23

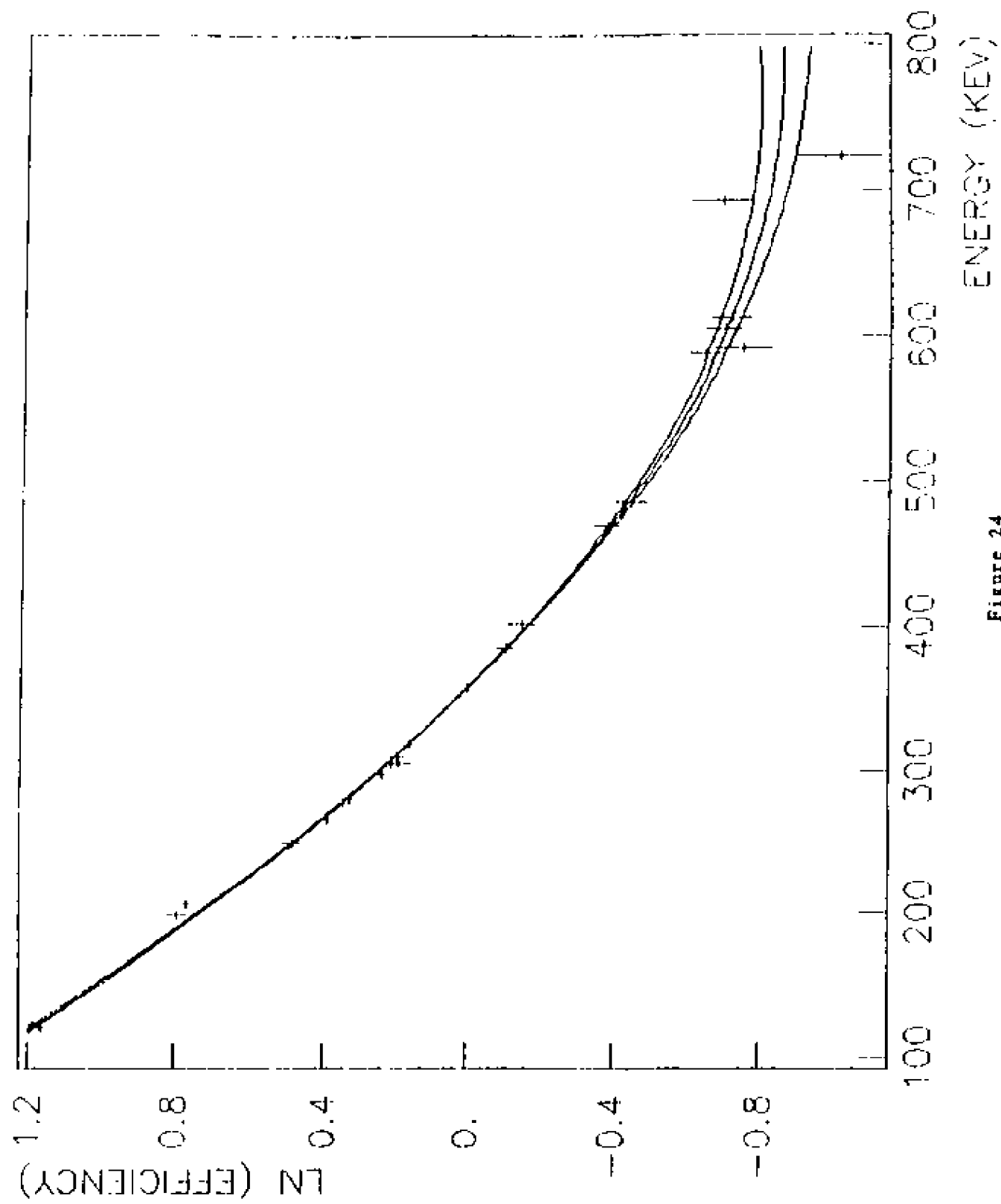


Figure 24

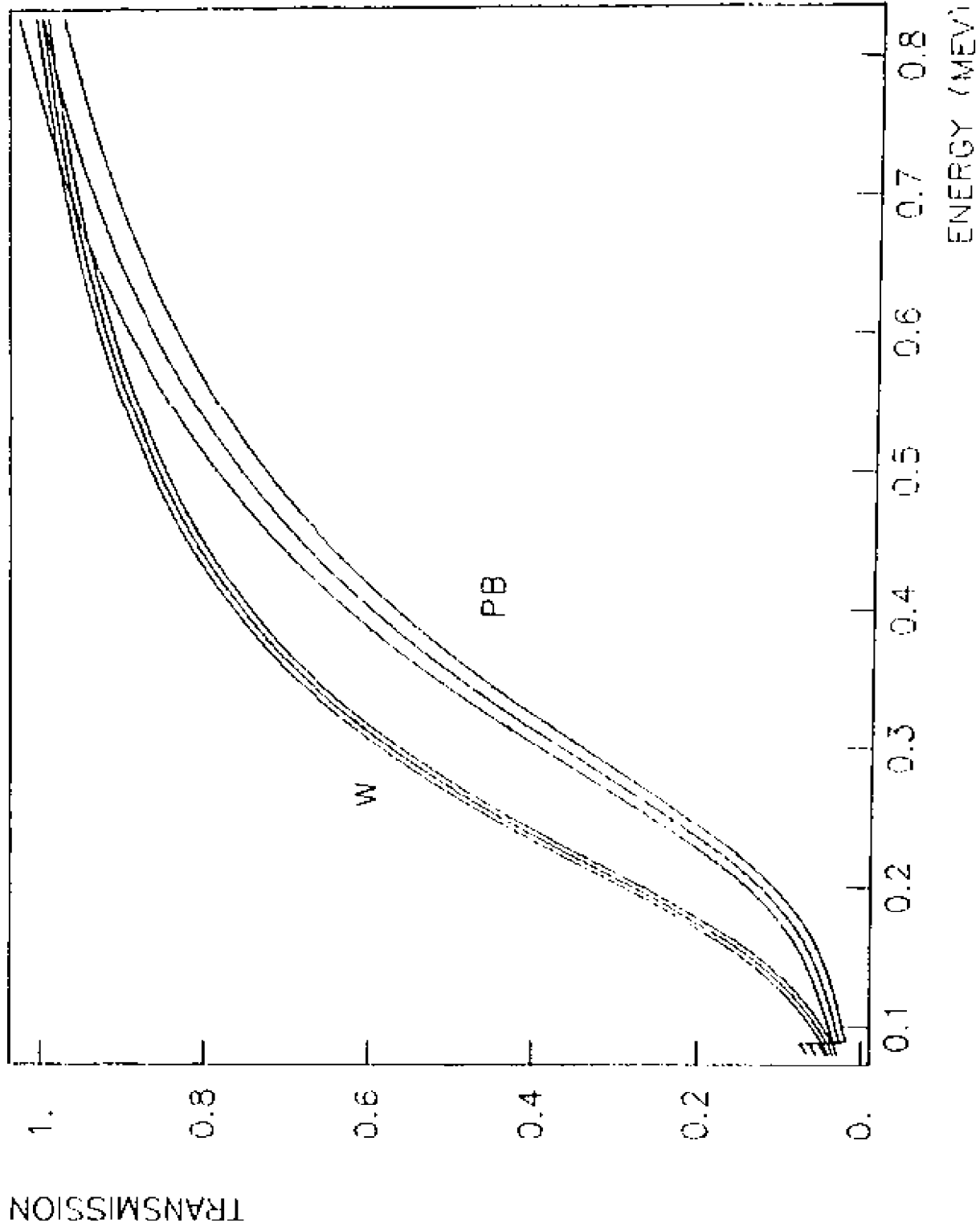


Figure 25

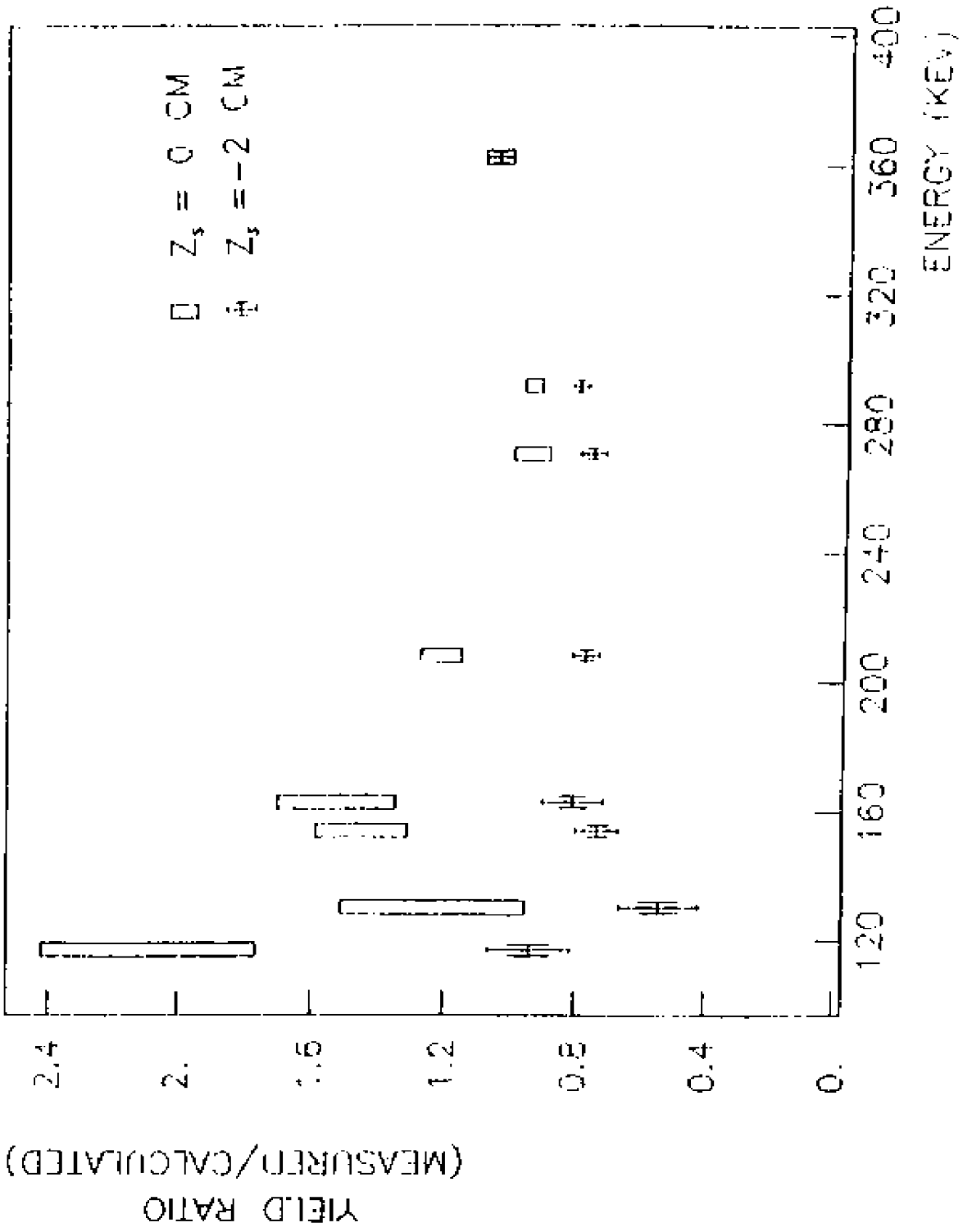


Figure 26

VITA

William Clarke Phillips

Born in Martinsville, Virginia, October 29, 1955. Graduated from Martinsville High School in that city, June 1974, B.S. (Physics, with High Honors) 1978, M.S. (Physics) 1981, Ph.D. (Physics) 1988, all from The College of William and Mary in Virginia.